Cretaceous partial melting, deformation, and exhumation of the Potters Pond migmatite domain, west-central Idaho

Author: William J. Montz

CRETACEOUS PARTIAL MELTING, DEFORMATION, AND EXHUMATION OF THE POTTERS POND MIGMATITE DOMAIN, WEST-CENTRAL IDAHO

William J. Montz

A thesis

submitted to the Faculty of

the department of Earth and Environmental Sciences

in partial fulfillment

of the requirements for the degree of

Master of Science

Boston College
Morrissey College of Arts and Sciences
Graduate School

August 2016

CRETACEOUS PARTIAL MELTING, DEFORMATION, AND EXHUMATION OF THE POTTERS POND MIGMATITE DOMAIN, WEST-CENTRAL IDAHO

William J. Montz
Advisor: Seth C. Kruckenberg, Ph.D.

The Potters Pond migmatite domain (PPMD) is a heterogeneous zone of migmatites located ~10 km southwest of Cascade, Idaho within the western Idaho shear zone (WISZ). The PPMD is the only known exposure of migmatites within the WISZ over its ~300 km length, occurring where the shear zone orientation changes from 020° south to 000° north of the migmatite domain. Structural mapping within the PPMD has identified multiple generations of migmatite with varied structural fabrics. Leucosome layers were sampled from distinct migmatite localities and morphologies (e.g., metatexite, diatexite) to determine the timing and duration of partial melting in the PPMD. U-Pb age determinations of zircon by means of LA-ICP-MS document two periods of protracted migmatite crystallization during the Early and Late Cretaceous. Early Cretaceous (ca. 145 to 128 Ma) migmatite crystallization ages are coeval with the collision and suturing of oceanic terranes of the Blue Mountains province with North America, and the formation of the Salmon River suture zone (SRSZ). Migmatite crystallization ages from ca. 104 to 90 Ma are associated with Late Cretaceous dextral transpression in the WISZ. Field observations and geochronology of cross cutting leucosome relationships are interpreted to record deep crustal deformation and anatexis associated with formation of the SRSZ, subsequently overprinted by solid-state deformation and renewed anatexis during the evolution of the WISZ. These data are the first direct evidence of the synmetamorphic fabric related to the SRSZ east of the initial Sr 0.706 isopleth, and that the WISZ is a temporally distinct overprinting structure.

TABLE OF CONTENTS

LIST OF FIGURES

LIST OF TABLES

ACKNOWLEDGEMENTS

I would like to thank my advisor Dr. Seth Kruckenberg for his guidance and direction throughout the completion of my MS degree. Without your academic and financial support, none of this would have been possible.

Special thanks Basil Tikoff for providing the initial spark that lit my interest in structural geology all those years ago, and for providing the means and motivation to pursue geologic research. Thank you for taking me under your wing and fueling my love of geology.

I would like to express my gratitude to Kate Johnson for keeping me sane during stressful times, and Babs Wortham for looking out for my health and wellbeing when I forgot to do so myself. I may have become a crazy, malnourished geologist without your support.

Thanks also to Shaina Cohen, Martha Parsons, and Jamie Kendall for your willingness to discuss solid earth geoscience. It was comforting to know you were always available to talk about structure, metamorphism, or mineralogy.

I am truly grateful for the support of my family in every aspect of my life. I definitely would not be where I am today without the love and guidance of my parents and unwavering friendship of my brother.

FORWARD

To the reader:

This thesis has been written in manuscript form. As a result, it must be noted that this thesis is a product of scientific collaboration. While the results and interpretations presented herein are a product of my own research and writing, but I must give credit to those with whom I have collaborated. Their respective contributions are acknowledged accompanying the manuscript.

INTRODUCTION

The western margin of Laurentia is marked by the accretion of multiple oceanic terranes. The broad zone of arc-continent collision in western Idaho is known as the Salmon River suture zone (SRSZ), which juxtaposes the island arc terranes of the Blue Mountains on the west with the North American craton to the east (e.g., Hamilton, 1963; Lund and Snee, 1988). Estimates on the timing of this accretion vary from Early Cretaceous (Getty et al., 1993) to Late Jurassic (Lamaskin et al., 2015). Sometime after accretion of the island arc terranes to this margin, the Salmon River suture zone was affected by the western Idaho shear zone (WISZ) (Lund and Snee, 1988; Manduca et al., 1993; McClelland et al., 2000; Giorgis et. al., 2005). The western Idaho shear zone records dextral, transpressional deformation (e.g., Giorgis and Tikoff, 2004; Giorgis et. al., 2008; Giorgis et al., in review). Current estimates for timing indicate that deformation ceased at ~90 Ma (Giorgis et al., 2008).

A major debate has centered on the timing relation between the Salmon River suture zone and the western Idaho shear zone: There are two main interpretations. The first option is that there is temporal continuity between suturing and the transpressional deformation. This interpretation is implicit in the work of Selverstone et al. (1992) and Snee et al. (1995), and is explicit in Gray et al. (2012). The second option is that the western Idaho shear zone is a distinctly younger feature that overprints the Salmon River suture zone. This interpretation of spatially overlapping structures was initially proposed for both the western Idaho shear zone and the Coast shear zone of British Columbia and Alaska by McClelland et al. (2000), and subsequently supported by Tikoff et al. (2001), Giorgis et al. (2008), and Blake et al. (2009).At present, the data supports either option,

depending on the interpretation of fabrics to U-Pb zircon ages in specific plutonic units (e.g., Gray et al., 2012; Braudy et al., in review).

We studied a newly mapped migmatite domain associated with the western Idaho shear zone on West Mountain (Braudy, 2013; Braudy et al., in review). Migmatites, representing former partially molten rocks and magmas (e.g., Sawyer, 2008; Vanderhaeghe, 2009), have been shown by numerous studies to provide critical constraints on tectonic evolution. Partial melt migration is intrinsically linked to deformation (e.g., Brown and Solar, 1998; Weinberg and Mark, 2008), and as such migmatites – particularly in shear zones – inform on the timescales and interaction of crustal melting and deformation processes. Our study leverages combined structural mapping and U-Pb geochronology in this newly recognized migmatite domain - herein referred to as the Potters Pond migmatite domain (PPMD) - to determine the timing and duration of partial melting and the deformation history recorded in the PPMD migmatites. We demonstrate that migmatites comprising the PPMD record two protracted periods of migmatite crystallization in the Early Cretaceous (ca. 145 to 128 Ma) and Late Cretaceous (ca. 104 to 90 Ma). We interpret these ages to record deep crustal deformation and anatexis during formation of the SRSZ and WISZ, respectively. These data show that the SRSZ and WISZ occurred as two distinct events separated by a deformational hiatus, and offer the first direct evidence that Late Cretaceous mylonites of the WISZ have overprinted Early Cretaceous synmetamorphic structures associated with the SRSZ. The U-Pb zircon age distribution also indicates partial melting of both Blue Mountain and North American sources. As such, a sliver of Blue Mountain terrain must exist east of the western Idaho shear zone at this location, consistent with the interpretation of Braudy et

al. (in review). Further, our U-Pb geochronology results are the first clear evidence from south of the Orofino area (e.g., Woodrat Mountain shear zone; Lewis et al., 2007, 2014; Schmidt et al., in review) that deformation associated with suturing affected the North American side of the western Idaho shear zone.

GEOLOGIC BACKGROUND

The western Idaho shear zone is a steeply dipping, roughly north-south striking high strain zone that follows the initial Sr 0.706 isopleth (Armstrong et al., 1977) for over 300 km along the western margin of the Idaho batholith (Manduca et al., 1993; McClelland et al., 2000; Tikoff et al., 2001; Giorgis et al., in review) (Figure 1). The shear zone lies at one of the many sub-vertical plate boundaries within the North American Cordillera. Although this subvertical boundary was originally thought to reflect the accretion of oceanic terranes with continental North America (e.g., Selverstone et al., 1992), it is potentially better considered as a transpressional modification of that accretionary boundary (e.g., McClelland et al., 2000). Giorgis et al. (2008), in an attempt to build consensus about regional nomenclature, separated the accretionary SRSZ from the shearing modification of that boundary by the WISZ.

In western Idaho, the tectonic history begins with the Late Jurassic-Early Cretaceous collision of the oceanic terranes of the Blue Mountains province with the North American craton (Avé Lallemant, 1995; Vallier, 1995; Gray and Oldow, 2005). Initial collision and suturing began ca. 144 Ma and was active through ca. 128 Ma (Selverstone et al., 1992; Getty et al., 1993), forming the SRSZ in west-central Idaho (Lund and Snee, 1988). Following suturing, intrusive suites were intruded in western Idaho, with ages that

generally decrease from west to east. In the McCall region, these are the Hazard Creek complex, Little Goose Creek complex, and Payette River tonalite. Rocks of the westernmost unit, the Hazard Creek complex, have two main compositions: an older generation of tonalitic to quartz dioritic orthogneiss, and a younger generation of less deformed tonalite and trondhjemite (Manduca et al., 1993). U-Pb zircon ages indicate emplacement and deformation of the Hazard Creek complex was ongoing by ca. 118 ± 5 Ma and concluded by ca. 114.4 ± 2.2 Ma (Manduca et al., 1993; Unruh et al., 2008). East of the Hazard Creek complex lies the Little Goose Creek complex, an intrusion composed primarily of porphyritic granodiorite and granite orthogneiss. The Little Goose Creek complex was emplaced between ca. 105 ± 1.5 and 110 ± 5 Ma (Manduca et al. 1993; Giorgis et al, 2008; Unruh et al., 2008). The youngest intrusion is the Payette River tonalite and was emplaced between 91.5 ± 1.1 and 89.7± 1.2 Ma (Giorgis et al., 2008). The Payette River tonalite is characterized by coarse-grained hornblende and the presence of mafic enclaves.

The WISZ is located within the SRSZ, and is the present day boundary between accreted oceanic arc terranes and cratonic North America. Deformation is best characterized in the McCall region, where it affects the easternmost portion of the Hazard Creek unit and all of the Little Goose Creek complex. The Payette River tonalite is interpreted as a syn-tectonic, steeply dipping sill associated with the western Idaho shear zone (e.g., Manduca et al., 1993). The shear zone has been described as far south as the Owyhee Mountains (Bendford et al., 2010) and extends north through McCall and Riggins (Giorgis et al., 2008; Blake et al., 2009; Giorgis et al., in review) before stopping at a younger shear zone near Orofino (McClelland and Oldow, 2007).

Characteristic fabric observed throughout the western Idaho shear zone is a steeply dipping, N- to NNE-trending foliation (e.g., Giorgis et al., 2008, McClelland et al., 2000; Benford et al., 2010). Tikoff et al. (2001) noted that WISZ fabrics restore to a vertical orientation, when Miocene-present faulting is removed. Thus, dextral transpression is thought to be responsible for the deformation associated with the western Idaho shear zone (e.g., McClelland et al., 2000; Giorgis et al., in review). Lund and Snee (1988) interpret regional structures to indicate a component of dextral motion, agreeing with the results of fabric analyses of mylonitic zone within the western Idaho shear zone (e.g., Giorgis and Tikoff, 2004; Giorgis et al., in review). U-Pb zircon ages constrain deformation along the WISZ to have ceased by 90 Ma (e.g., Giorgis et al., 2008).

West Mountain, immediately south of McCall, also contains the WISZ (Bonnichsen, 1987; Giorgis et al., 2008; Braudy, 2013; Braudy et al., in review). West Mountain is more vegetated, lacks pervasive glaciated outcrops, and the bedrock geology is more significantly covered by Columbia River basalt flows. A series of intrusive suites – similar in both age and composition to those in the McCall area – are found on West Mountain, including the syntectonic Payette River tonalite (Braudy et al., in review). Geochemical analyses, however, indicate major differences from intrusions in the McCall area (Braudy et al., in review). First, and most important, geochemistry on zircon centers indicate that a component of Blue Mountain terrane rocks occurs E of the WISZ. Second, unlike the Hazard Creek complex, the westernmost exposed orthogneiss units in West Mountain are dominantly derived from continental material. Braudy (2013) documented a change in foliation orientation in the orthogneisses on West Mountain, from 005° to 024°, and interpreted this pattern to reflect a primary along-strike variation

in the WISZ. Her mapping also recognized the presence of a migmatite complex near Snowbank Mountain, originally noted by reconnaissance geological mapping (1° x 2° of Baker Quadrangle; Mitchell and Bennett, 1979). Two Lu-Hf dates on garnets, 110.0 ± 1.0 Ma and 99.5 ± 1.4 Ma, were analyzed from this migmatite complex and were interpreted to reflect different generations of garnet growth (Wilford, 2012; Braudy et al., in review). A third Lu-Hf date on garnet from within the WISZ indicated a garnet grown during deformation at 97.1 ± 0.8 Ma (Braudy et al., in review).

COMPOSITION AND STRUCTURE OF THE PPMD MIGMATITES

Migmatites are classified based on increasing granitic fraction and continuity of the former solid framework, and are subdivided into metatexites (former partially molten rocks) and diatexites (former magmas) (Mehnert, 1968; Brown, 1973; Wickham, 1987; Sawyer, 1994; Vanderhaeghe, 2001, 2009). Metatexites comprise gneisses and schists with a continuous foliation enclosing leucosome (i.e. segregated melt), whereas diatexites are dominated by granite enclosing enclaves, selvages, and/or crystals in suspension (e.g., Sawyer, 2008; Vanderhaeghe, 2009). Migmatites within the Potters Pond migmatite domain are structurally and compositionally heterogeneous, consisting primarily of stromatic and folded metatexite, interlayered or intruded by heterogeneous diatexite (Figure 2).

Metatexite is volumetrically minor in the PPMD, consisting of planar and folded domains of stromatic metatexite and entrained blocks of transposed amphibolite and foliated granodioritic to tonalitic gneisses. Paleosome layers are locally boudinaged and enveloped by leucosome, which are in turn folded by tight to open folds on the cm- to m-

scale (Figure 3F,G). A solid-state foliation is observed in stromatic metatexites, defined by domains of stretched quartz aligned parallel to a variably developed transposition foliation. Throughout the PPMD, stromatic metatexite forms anastomosing domains and regions that are invariably cut by discordant layers of cm- to m-scale magmatic-textured leucosome, or deformed and intruded by voluminous bodies of heterogeneous diatexite (Figure 2).

Heterogeneous diatexite is the dominant migmatitic variety exposed throughout the Potters Pond migmatite domain (Figure 2). This melt-rich diatexite is characterized by a well-developed synmigmatitic (i.e. magmatic) layering defined by biotite schlieren and/or schollen of amphibolite, tonalite, and, rarely, granulite, enveloped by granitic to granodioritic neosome (Figure 3A,B). Diatexite within the PPMD is further subdivided into schlieren-textured, melanocratic, and nebulitic varieties. Schlieren-texture diatexite is distinguishable by a "wispy" synmigmatitic foliation and abundant layers of segregated leucosome (Figure 3B). This texture contrasts melanocratic varieties, which are characterized by a higher modal abundance of biotite, planar synmigmatitic layering, and locally boudinaged leucosome oriented parallel to a magmatic to subsolidus foliation (Figure 3E). Garnet is abundant in diatexite, though not observed everywhere. In melanocratic diatexite, garnet is typically fine grained and dispersed throughout the neosome. In both schlieren-textured and melanocratic diatexite, course grained garnets are concentrated along leucosome–melanosome margins. Leucocratic nebulite is distinguished by voluminous, granitic to granodioritic neosome with a swirly to cryptic synmigmatitic foliation, and faint leucosomes commonly containing clusters of large garnets up to 2 cm in diameter (Figure 3C). Schlieren-textured and nebulitic diatexite

tend to form large intrusive bodies on the m- to km-scale throughout the PPMD, whereas melanocratic planar diatexite bodies are primarily found in the southwestern portion of the migmatite domain (Figure 2).

We distinguish the previously described migmatite units from agmatic migmatite that occurs within a band along the western edge of the PPMD. This unit is characterized by blocks of fine-grained biotite-rich tonalitic paleosome cut by leucosome containing abundant hornblende and biotite, and lacking garnet (Figure 3D). These layers form discontinuous lenses within schlieren-textured diatexite (Figure 2), which become more elongate in the northern parts of the PPMD.

The dominant orientation of synmigmatitic layering and leucosome orientation within the Potters Pond migmatite domain varies from 000º to 020º (Figure 4). This pattern is the expected fabric orientation within the WISZ based on mapping by Braudy et al. (in review) who documented a solid-state fabric orientation of 005º north of the PPMD and 024º south of the PPMD. A second population of leucosome orientations trends 050º. The relationship between 000º-020º and 050º fabrics varies spatially. In some localities, the 050º fabric is cross cut by the 020º fabric, where elsewhere they merge into each other. Lineations, where present, either pitch down dip or pitch steeply to the north.

Evidence for melt-present deformation is abundant within the Potters Pond migmatite domain; in all migmatite varieties melt accumulation is associated with dilatant structural sites (Figure 5). For example, asymmetric blocks of paleosome within diatexite preserve melt in pressure shadows associated with rotation during dextral shearing (Figure 5A). Similarly, accumulated melt is preserved in boudin necks (Figure 5B,C), flanking structures associated with folded migmatite layers (Figure 5D), and in the hinge zones of

rootless folds in diatexite (Figure 5E). These structural relationships attest to the role of melt-present deformation in the PPMD (e.g., McLellan, 1988; Brown, 1994; Brown and Solar, 1998; Marchildon and Brown, 2002, 2003; Sawyer, 2001; Holness, 2008). We note, however, that the deformation within the migmatite domain was variable through time as evidenced by multiple periods of migmatite formation and changes in deformation conditions (e.g., melt-present versus solid-state). More explicitly, based on structural relationships, the PPMD migmatites record a poly-phase melting history. Migmatization and melt-present deformation recorded in stromatic metatexite and melanocratic diatexite domains show evidence of overprinting subsolidus deformation, as described previously. These early-formed structural features are, in turn, cut and deformed by subsequent partial melts forming the volumetrically distinct regions of magmatically deformed heterogeneous diatexite that characterizes much of the PPMD.

GEOCHRONOLOGY

Lu-Hf ages of ca. 110-99 Ma are interpreted to reflect multiple generations of garnet growth during migmatite formation in the PPMD (Wilford, 2012; Braudy et al., in review). This interpretation is in agreement with the structural record of polyphase partial melting in the PPMD, as described previously. However, the timing and duration of migmatite crystallization remains unknown. We present new U-Pb data from structurally and compositionally distinct migmatites in the PPMD in order to characterize the timing and duration of partial melting and its relationship to different stages of the tectonic evolution of western Idaho.

Analytical methods

Seven samples were selected for U-Pb isotopic analysis from leucosomes within structurally and compositionally distinct migmatite localities, focused on structural settings in which the crystallization ages of leucosome would provided further constraints on the relationships between melt-present and solid-state deformation histories. Zircon and monazite grains were isolated using standard crushing and mineral separation procedures, and were dated by laser ablation-inductively coupled plasma-mass spectrometer (LA-ICP-MS) U-Pb methods. All analyses were conducted at the Arizona LaserChron Center (Tucson, Arizona), where zircon analyses were conducted on a Thermo Element2 single-collector ICP-MS, and monazite analyses were conducted on a Nu Plasma multicollector ICP-MS. Crystallization ages from rim overgrowths and new zircon growth attributed to migmatite crystallization were calculated using the weighted mean $^{206}Pb/^{238}U$ ages of clustered populations of data. Analyses with a large uncertainties (>10%) and excessive discordance (>20%) or reverse discordance (>5%) were discarded. Additional details of the analytical method and data tables containing analytical results are provided in the supplementary material.

Results of U-Pb Zircon Analyses

Boudinaged leucosome within melanocratic diatexite (14WM39a)

Sample 14WM39a is sourced from granodioritic leucosome within a domain of melanocratic diatexite northwest of Blue Lake (Figure 2). At this locality, the host melanocratic diatexite is characterized by planar synmigmatitic layering and a strong mineral lineation. The sampled leucosome is boudinaged forming rough dextral

sigmoidal shapes that pinch and swell parallel to synmigmatitic layering. Garnets are crowded at the contact of the leucosome with the surrounding melanocratic diatexite. A strong solid-state fabric that conforms to the shape of the boudins is observed for a few centimeters in the surrounding rock. Zircon grains in sample 14WM39a are euhedral to subhedral, and range in size from 150 to 300 μm (Figure 6). Oscillatory-zoned cores are commonly resorbed. Five- to 20 μm wide rim overgrowths surround core domains. Fifty locations on 32 zircon grains were analyzed in sample 14WM39a, yielding $^{206}Pb/^{238}U$ ages from ca. 103 to 153 Ma. Thirty-nine of these analyses yield a statistical age of 136.8 ± 0.09 Ma (MSWD = 1.4). Three younger grains have $^{206}Pb/^{238}U$ ages as young as ca. 103.1 Ma.

Schlieren-textured granodiorite diatexite (13WM25)

Sample 13WM25 is from a diatexite pavement north of, and adjacent to, Blue Lake with intermittent zones of metatexite a few meters thick. The sample was taken from a schlieren-textured, biotite granodiorite diatexite with a strong magmatic foliation (243/79°W with a lineation pitching 80° from the N), and well-defined centimeter-scale leucosomes that alternate with thinner melanosome. Garnet is abundant in both leucosome and melanosome. The zircon population in this sample consists of subhedral to anhedral grains that form elongate to equant crystals 100 to 200 μm long (Figure 7). The morphology of core domains exhibits large variability, with anhedral to euhedral cores that are homogeneous or irregularly zoned. Rarely, cores display oscillatory zoning. Rim overgrowths are 10 to 70 μm wide and exhibit convoluted zoning. Fifty spots on 30 zircon grains were analyzed in sample 13WM25. Sixteen analyses yield concordant ages.

Eleven of the core analyses and 3 of the rim analyses yield Precambrian $^{206}Pb/^{238}U$ ages. The remaining 20 rim analyses exhibit extreme variability in $^{206}Pb/^{238}U$ ages, ranging from ca. 96 to 384 Ma. The three youngest analyses yield a mean $^{206}Pb/^{238}U$ age of 96.8 ± 5.5 Ma (MSWD = 2.3). The next youngest group of 3 ages yields a mean age of 109.7 ± 1.9 Ma (MSWD = 0.36).

Schlieren-textured granodiorite diatexite (13WM30)

Sample 13WM30 is from a large body of granodioritic diatexite located near the southern margin of the PPMD west of Blue Lake (Figure 2). Biotite schlieren and tonalitic blocks are scattered throughout the outcrop, which has a pervasive magmatic foliation. The outcrop from which this sample is sourced is >100 m^2, forming a large concordant intrusive body of diatexites surrounded on three sides by stromatic metatexite. The surrounding metatexite is partially deformed in the solid-state as evidenced by stretched quartz and feldspar porphyroclasts, and locally has a near-mylonitic fabric. The solid-state foliation conforms to the boundary of the granodioritic diatexite, striking parallel to the contact. The zircon population consists of euhedral to subhedral grains 200 to 300 μm long. Internal structure is uniform throughout the population, with light cores displaying indistinct oscillatory zoning (Figure 8). Light rim overgrowths are separated from the core domains by dark, oscillatory-zoned mantles of variable thickness. We analyzed both core and rim domains of 30 grains for a total of 50 analyses in sample 13WM30. The majority of analyses (N=47) have Cretaceous $^{206}Pb/^{238}U$ ages ranging from ca. 91 to 142 Ma. While 34 of the analyses yield $^{206}Pb/^{238}U$ ages ranging from ca. 91 to 108 Ma, 23 analyses define a statistical age of 100.3 ± 0.92 Ma (MSWD = 1.8).

Agmatic migmatite (14WM115)

Sample 14WM115 was collected near the northwestern margin of the PPMD from a large lens-shaped outcrop of agmatic migmatite. Zircon crystals from this sample are typically 300 to 400 μm long, and have length to width ratios of <5:1 (Figure 9). Internal structure is variable, with core domains displaying a range of zoning patterns including unzoned, sector-zoned, and oscillatory-zoned cores. Rim overgrowths display wavy subhedral overgrowths and commonly lack distinct zoning. We analyzed 28 zircon grains with 38 individual spot analyses from sample 14WM115. All 38 analyses give Cretaceous $^{206}Pb/^{238}U$ ages ranging from ca. 93 to 109 Ma. Twenty-nine analyses yield a mean $^{206}Pb/^{238}U$ age of 98.6 ± 0.56 Ma (MSWD = 0.87).

Nebulitic diatexite (14WM58)

Sample 14WM58 is from a large, homogeneous body of massive to nebulitic diatexite. This melt-rich outcrop is nearly anatectic granite, containing no remnants of paleosome and only small (2 cm long) pervasive wisps of biotite. Variably sized garnet (2 mm to 2 cm in diameter) is distributed densely throughout the diatexite body. Zircon crystals in this sample are characterized by euhedral to subhedral elongate crystals, ranging from 200 to 500 μm in length (Figure 10). Core domains commonly display oscillatory zoning. Rim overgrowths also exhibit oscillatory zoning, and are separated from the cores by a thin CL dark band. A total of 50 analyses on 30 grains were analyzed in this sample. The zircon population in sample 14WM58 yielded $^{206}Pb/^{238}U$ ages ranging from ca. 93 to 146 Ma, with two prominent age populations. Thirty analyses have Early Cretaceous $^{206}Pb/^{238}U$ ages for both rim and core domains, with 21 of these yielding a

mean $^{206}Pb/^{238}U$ age of 132.3 ± 0.89 Ma (MSWD = 1.3). A younger population consisting of 9 rim analyses has a mean $^{206}Pb/^{238}U$ age of 95.3 ± 0.94 Ma (MSWD = 1.6).

Discordant leucosome in stromatic metatexite (14WM37a)

Sample 14WM37a is from a discordant leucosome that cross cuts an outcrop of folded and stromatic metatexite. The sampled leucosome cuts the metatexite layering at a high angle, and merges with a layer-parallel leucosome 1 meter to the north, before cutting across a larger diatexite body of granodioritic composition. This diatexite contains delicate magmatic structures (e.g., rootless folds) and has a weak and pervasive solid-state fabric. Equant to elongate zircon grains in this sample are 100 to 300 μm long and range from euhedral to anhedral crystals (Figure 11). Internal structure is variable, but grains typically exhibit sector and oscillatory-zoned euhedral to subhedral cores. Some grains display an oscillatory-zoned mantle surrounded by a light rim overgrowth. A few of the sector-zoned grains lack overgrowths that are distinguishable from the core domains. We analyzed 50 individual spots on 30 zircon grains in sample 14WM37a. Forty of these analyses give Late Cretaceous $^{206}Pb/^{238}U$ ages ranging from ca. 84 to 100 Ma, with the remaining 10 analyses extending into the Early Cretaceous as far back as ca. 116 Ma. Twenty-three of the Late Cretaceous analyses yield a statistically relevant age of 93.3 ± 0.7 Ma (MSWD = 1.4). Five younger grains have $^{206}Pb/^{238}U$ ages as young as ca. 84 Ma.

Leucosome in stromatic metatexite (13WM24)

Sample 13WM24 was collected from an outcrop in the metatexite domain in the northeastern part of the PPMD. This sample is from a granitic leucosome that parallels both synmigmatitic layering and amphibolite blocks present in stromatic metatexite. The leucosome merges seamlessly with melt that has accumulated in boudin necks, and anastomoses around amphibolite blocks that vary strain intensity perpendicular to strike. Zircon crystals in this sample are characterized by euhedral to subhedral grains, typically 200 to 300 μm long with variable length to width ratios ranging from 2:1 to >4:1. Under cathodoluminescence, grains typically exhibit oscillatory and sector-zoned core domains (Figure 12). Overgrowths range from wide rims that display oscillatory and sector zoning to thin rims with homogeneous and sector-zoned tips. A few grains exhibit portions of their core domain that have been resorbed and replaced by younger homogenous growth. We analyzed 30 zircon grains with 50 individual spot analyses in sample 13WM24. Forty-seven of the 50 analyses have Cretaceous $^{206}Pb/^{238}U$ ages ranging from ca. 89 to 136 Ma. The youngest 31 analyses from the Late Cretaceous yield a mean $^{206}Pb/^{238}U$ age of 93.5 ± 1.0 Ma (mean square of weighted deviates [MSWD] = 3.3). Eliminating 9 analyses that are slightly older results in a weighted mean age of 92.4 ± 0.7 Ma and a lower MSWD of 1.5.

Results of U-Pb Monazite Analyses

Fourteen monazite grains from sample 13WM24 were analyzed for a total of 19 analyses (Figure 13). The majority of the grains yield either discordant ages or negative $^{208}Pb/^{232}Th$ ages, and have therefore been discarded. Eight analyses on 5 grains yield

acceptable results with $^{206}Pb/^{238}U$ ages ranging from ca. 90 to 105 Ma. The grains from which these analyses were taken do not appear zoned, and ages show no correlation to their location in the monazite grains. The 8 analyses yield a mean $^{206}Pb/^{238}U$ age of 97.7 ± 2.3 Ma (MSWD = 1.3).

Twenty-four monazite grains from sample 13WM25 were analyzed for a total of 30 analyses (Figure 14). Almost all of the analyses (N= 29) give Late Cretaceous $^{206}Pb/^{238}U$ ages ranging from ca. 85 to 99 Ma, and show no correlation to spot location in monazite grains. A single analysis yields an Early Cretaceous age of ca. 106 Ma. The young cluster of 29 analyses gives a mean $^{206}Pb/^{238}U$ age of 91.5 ± 1.2 Ma (MSWD = 1.7).

Twenty-seven individual spots were analyzed on monazite grains in sample 13WM30 (Figure 15). All 27 analyses yield Late Cretaceous $^{206}Pb/^{238}U$ ages ranging from ca. 85 to 100 Ma, and have a weighted mean $^{206}Pb/^{238}U$ age of 90.3 ± 1.6 Ma (MSWD = 2.2).

Twenty-three monazite grains were analyzed with 33 individual spots in sample 14WM37a (Figure 16). Seven of these exhibited excessive discordance. The remaining 26 analyses give Late Cretaceous $^{206}Pb/^{238}U$ ages ranging from ca. 87 to 98 Ma, and yield a weighted mean age of 92.1 ± 1.1 Ma (MSWD = 1.1). No correlation is observed between spot location on a rim or core and its resulting age.

Twenty-four spots on 17 monazite grains were analyzed from sample 14WM39a (Figure 17). Twenty-three of these analyses are concordant, yielding $^{206}Pb/^{238}U$ ages ranging from ca. 87 to 98 Ma, showing no correlation to location within the monazite grains. All 23 concordant analyses give a weighted mean age of 91.4 ± 1.2 Ma (MSWD = 1.4).

Thirty-four individual spots on 21 monazite grains were analyzed in sample 14WM58, yielding $^{206}Pb/^{238}U$ ages ranging from ca. 89 to 101 Ma (Figure 18). There is no observed correlation between the analysis age and whether the spot was located in a core or rim domain. Thirty-two of these analyses display concordance, and give a mean $^{206}Pb/^{238}U$ age of 92.9 ± 1.4 Ma (MSWD = 1.4).

Two sector zoned monazite grains were recovered from sample 14WM115. Eight spots on each grain for a total of 16 analyses yield $^{206}Pb/^{238}U$ ages ranging from ca. 89 to 94 Ma (Figure 19). There is no correlation between the age acquired from a spot and the zone in which the spot is located. All 16 analyses yield a mean $^{206}Pb/^{238}U$ age of 92.7 ± 1.4 Ma (MSWD = 0.3).

DISCUSSION

Interpretation of the Geochronology Results

Schematic leucosome relationships of sampled migmatite units from the PPMD are shown in Figure 20. Field observations suggest that the melanocratic diatexite (14WM39a) formed during one of the oldest periods of partial melting. It is commonly cross-cut by folded metatexite, discordant leucosome (e.g., 14WM37a), and boudins of agmatic migmatite (e.g., 14WM115). Geochronology of this unit confirms it to be the oldest migmatization episode (ca. 137 Ma), with nearly all zircons analyzed crystallizing during the Early Cretaceous SRSZ event. Sample 14WM58 also has a population of $^{206}Pb/^{238}U$ ages correlative with the SRSZ (ca. 132 Ma).

Field observations indicate that the stromatic metatexite is one of the older generations of migmatite in the PPMD. Four samples collected for this study (13WM24,

13WM25, 13WM30, and 14WM37a) cross cut the metatexite, so we are able to provide a minimum estimate of its formation. Sample 13WM25 is the oldest of the four cross-cutting samples, with the 6 youngest analyses composing two peaks at ca. 97 and 110 Ma. Another 6 analyses yield a continuum of ages ranging from ca. 117 to 131 Ma, pushing the probable crystallization age of the stromatic metatexite into the Early Cretaceous. The 100.3 ± 0.92 Ma age obtained from sample 13WM30, and structural observations indicating that the body of schlieren-textured diatexite deforms stromatic metatexites along its margins, further supports this interpretation. The 93.3 ± 0.7 Ma age obtained for 14WM37a is logical based on structural overprinting relationships; this discordant leucosome clearly crosscuts structural fabrics within the stromatic metatexite, and correlative compositional fabrics in adjacent melanocratic diatexite layers. Sample 13WM24 yields the youngest migmatite crystallization age of leucosome within the stromatic metatexite. However, given that the sample was sourced from layer-parallel leucosome that merges seamlessly with melt accumulated in boudin necks, we interpret the 92.4 ± 0.7 Ma age to correspond to the last phases of migmatite crystallization in the PPMD.

The structural story of the agmatic diatexite (14WM115) is less clear. Lenses of agmatic diatexite share the same structural relationship with both the melanocratic diatexite and the schlieren-textured diatexite, which suggests its hornblende-bearing leucosomes could be either older (i.e., represent large blocks of older migmatite that have been included in younger diatexite) or younger (i.e., represent a formerly tabular migmatite body that has been boudinaged) than both of these units. Both of these interpretations suggest the PPMD experienced an episode of flux melting, either early in

the PPMD's history before switching to dehydration melting, or as a short episode in between periods of dehydration melting. However, results of geochronologic analysis place the age of crystallization at ca. 99 Ma, suggesting hornblende-bearing leucosomes are of intermediate age between the melanocratic diatexite and the schlieren-textured diatexite. This allows for a third interpretation: the formation of the hornblende and absence of garnet are related to composition of the protolith rather than an episode of flux melting. This interpretation is supported by the spatial distribution of the agmatic diatexite along the western margin of the PPMD, where there may have been a compositional layer that favored the formation of hornblende during anatexis and migmatite crystallization.

Sample 14WM58, the nebulitic diatexite in the northern part of the PPMD, shares structural relationships similar to sample 13WM30 – it forms a large intrusive body of magmatically deformed melt-rich diatexite enveloped by stromatic metatexite. It is worth noting that the 95.3 ± 0.94 Ma age obtained from sample 14WM58 is approximately 5 million years younger than that obtained from sample 13WM30. However, based on their structural and morphological similarities, it is likely that these large migmatite bodies formed coevally during a protracted period of migmatite crystallization.

U-Pb ages obtained from all zircon grains analyzed range from ca. 160 to 84 Ma, with analyses from two samples extending into the Paleozoic and Precambrian. $^{206}Pb/^{238}U$ ages obtained from rim overgrowths and new zircon growth attributed to migmatite crystallization are dominantly concentrated within two age populations ranging from ca. 145 to 128 Ma and ca. 104 to 90 Ma (Figure 21A). These data are interpreted to suggest that the PPMD records two protracted periods of migmatite crystallization. The older age

population is correlative to the accretion of ocean arc terranes of the Blue Mountains province with Laurentia and the formation of the SRSZ (e.g., Selverstone et al., 1992; Getty et al., 1993). The second, younger population of ages coincides with the timing of dextral transpressional deformation along the WISZ (e.g., Manduca et al., 1993; Giorgis et al., 2008; Braudy et al., in review). Mean $^{206}Pb/^{238}U$ ages from six of the seven monazite-bearing samples fall in a narrow range from ca. 93-90 Ma. The entire suite of monazite analyses (N=153) yields a mean age of 92.0 ± 0.4 Ma (MSWD = 1.0) (Figure 21B,C). This well-defined age is interpreted to record the initiation of exhumation of the PPMD, and therefore at least the local section of the western Idaho shear zone, at ca. 92 Ma.

The source of partial melt may have varied during the two protracted periods of crystallization. The majority of core and some rim analyses from sample 13WM25 extend into the Precambrian. While seven inherited Mesozoic ages ranging from ca. 246 to 149 Ma offer the possibility of inheritance from oceanic terranes, the remaining analyses all yielded Paleozoic or Precambrian ages. We interpret the bulk of Paleozoic and Precambrian ages as inherited ages from the North American continental crust. However, aside from two cores in sample 13WM24 and two Late Permian cores in sample 13WM30, all other inherited cores are Mesozoic and lack a North American signature. Mesozoic ages have commonly been identified in the Wallowa terrane of the Blue Mountains province (Schwartz et al., 2010, 2011; Kurz et al., 2011), suggesting the PPMD migmatites may be derived from a protolith related to oceanic terranes. Consequently, we interpret that there is likely both a Blue Mountain province and cratonic North America protolith for the migmatites comprising the PPMD. This

interpretation is consistent with that of Braudy et al. (in review) suggesting an eastward extension of the Salmon River suture zone on the cratonic side of the WISZ.

Tectonic Significance

Evidence of the timing and duration of western Idaho shear zone deformation is well established (Figure 22). The initiation of shearing is difficult to constrain. Nearly all of the plutonic rocks of the Little Goose Creek complex (LGCC) have been deformed by the WISZ (Manduca et al., 1993). While this observation does not require the age of the LGCC to correspond to the initiation of WISZ deformation, an examination of the strain recorded in the LGCC determined that the strain likely accumulated entirely after its intrusion, setting the lower age limit for WISZ deformation at ca. 105 Ma (Giorgis et al., 2005; Giorgis et al., 2008). Slightly younger metaplutonic rocks may indicate that ductile deformation began a few million years later. The ca. 104 Ma Crevice pluton – a correlative of the LGCC (Grey et al., 2012), and the ca. 101 Ma Four Bit Creek tonalite – a lightly deformed tonalite body within the westernmost WISZ suggest deformation may have started as late as 101 Ma (Braudy et al., in review).

Many studies have analyzed zircons from the Payette River tonalite (and correlatives) to determine cessation of ductile deformation in the WISZ. Weak solid-state fabric has been observed in western portions of the Payette River tonalite while eastern portions exhibit a magmatic foliation parallel to the solid state fabric of the WISZ (Manduca et al., 1993; Benford et al., 2010; Braudy et al., in review). These observations suggest WISZ deformation was waning during the emplacement of the Payette River tonalite. Recent U-Pb analysis of zircon from the Payette River tonalite yields ages of 91.5 ± 1.1 Ma and

89.7 ± 1.2 Ma (Giorgis et al., 2008), which agree with previous results (90 ± 5 Ma, Manduca et al., 1993; 89 ± 5 Ma, Lund and Snee, 1988) in other parts and correlatives of the Payette River tonalite (e.g., Whisky Ridge tonalite; Benford et al., 2010). Combined with a 90.0 ± 1.4 Ma undeformed pegmatite that cuts WISZ fabric (Giorgis et al., 2008), these data suggest the end of movement on the WISZ occurred ca. 90 Ma. New Lu-Hf garnet ages from Braudy et al. (in review) suggest peak metamorphism during WISZ deformation occurred ca. 98 Ma.

Migmatites in the Potters Pond migmatite domain provide an additional record of the timing and duration of WISZ deformation. The preservation of melt-present deformation structures throughout the PPMD allows us to conclude that deformation was ongoing during migmatization. The younger population of zircon ages therefore constrains the timing of migmatite crystallization in the PPMD, and also brackets the timing of WISZ deformation to between ca. 104 to 90 Ma, agreeing with previous studies.

Geochronologic studies that attempt to constrain the timing and duration of suturing focus on rocks from accreted Blue Mountain terranes and the Salmon River belt. Walker (1989) analyzed zircon from calc-alkaline plutons that cross-cut folded rocks of the Blue Mountains province. Emplacement ages of these plutons range from ca. 145 to 120 Ma, giving an early estimate on the initiation of collision. Sm-Nd dating of garnets in amphibolites from the Salmon River belt by Getty et al. (1993) revealed two stages of garnet growth: 1) ~144 Ma cores are interpreted to represent the initial collision of oceanic arc terranes with North America, and 2) ~128 Ma rim overgrowths record peak metamorphic conditions during underthrusting and burial of the Wallowa terrane (Getty et al., 1993). LaMaskin et al. (2015) recently suggested that the Wallowa terrane must

have accreted significantly earlier (by ~ 160 Ma), based on the presence of detrital North American zircons in sedimentary rocks overlying the Wallowa terrane.

The significance of the older population of $^{206}Pb/^{238}U$ zircon ages from the PPMD (ca. 145 to 128 Ma) is twofold. First, the melt-present deformation structures of the PPMD record a period of high temperature deformation that predates WISZ deformation. This range of ages correlates well with the proposed timing and duration of suturing presented in previous studies (e.g., Selverstone et al., 1992; Getty et al., 1993), and strengthens the constraints on the timing of deformation related to the SRSZ. Second, it has been commonly suggested that the WISZ is a temporally distinct event that has overprinted synmetamorphic fabric of the SRSZ (e.g., McClelland et al., 2000; Giorgis et al., 2005; Giorgis et al., 2008). However, no studies have identified direct evidence of overprinting within the WISZ, and some studies argue that the SRSZ and WISZ are both parts of a progressive deformation history associated with suturing (e.g., Grey et al., 2012). The PPMD records two periods of high temperature deformation with a ~25 m.y. gap in the deformational history. These data clearly show that WISZ and SRSZ structures are a result of two distinct events separated by a deformational hiatus, and offer the first direct evidence that Late Cretaceous mylonites of the WISZ have overprinted Early Cretaceous synmetamorphic structures associated with the SRSZ.

Summary

In summary, our data reveal two periods of partial melt crystallization within the PPMD (Figure 21A,22). The first period spans from ca. 145 to 128 Ma and records high temperature deformation associated with the collision, underthrusting, and suturing of

ocean arc terranes of the Blue Mountains province with North America. This timing agrees with metamorphic events dated by Sm-Nd garnet geochronology by Getty et al. (1993). The detrital zircon data reported in Lamaskin et al. (2015) suggests that the Wallowa terrane was adjacent to cratonic North America by the Late Jurassic. There are three complementary ways of explaining this apparent discrepancy. First, the Wallowa terrane may have been sufficiently adjacent to North America to receive sedimentation, but not yet colliding with western North America. Second, the collision of North America may have occurred by ca. 160 Ma, but the peak of migmatite crystallization did not begin within the collisional zone until ca. 10 m.y. later. The third option is that the initial collision of the Wallowa terrane was significantly south of its current location (e.g., Gaschnig et al., in review). Some northward movement of the accreted terranes is required by the subsequent activation of the right-lateral, transpressional western Idaho shear zone. This scenario, however, requires more translation than is implied by the minimum estimates of Giorgis et al. (2005). If significant right-lateral translation did occur, the timing of collision in Idaho is better recorded by our data and that of Getty et al. (1993), while the Lamaskin et al. (2015) data constrains collision to the south. We cannot evaluate between these possibilities with the present data.

The second period of melting spans from ca. 104 to 90 Ma, and records high temperature deformation associated with dextral transpression of the WISZ. Peak $^{206}Pb/^{238}U$ zircon ages for this period occur between ca. 98 and 94 Ma, agreeing with the timing of peak WISZ metamorphism evidenced by Lu-Hf garnet ages of ca. 98 Ma (Braudy et al., in review). Cross-cutting structural relationships in the PPMD provide evidence that melt-present deformational structures associated with the SRSZ were

overprinted by solid-state deformation associated with the first period of deformation. The planar diatexite of the PPMD contains boudinaged leucosomes of SRSZ age (e.g., sample 14WM39a; Figure 3E), and exhibits strong solid-state fabric. This fabric is cross-cut by leucosomes and diatexite of WISZ age that are not deformed in the solid-state. A narrow range of monazite ages from ca. 90 to 93 Ma indicates exhumation of the PPMD began by ca. 92 Ma, which agrees with the cessation of WISZ deformation by 90 Ma.

CONCLUSIONS

Structural and geochronologic data from the Potters Pond migmatite domain (PPMD) provide additional constraints to timing of deformation in western Idaho, and offer new insights into the deformation conditions of the deep crust during Cretaceous deformation. Migmatites from the PPMD preserve high temperature deformation structures which indicates deformation occurred in the presence of melt. Geochronology of leucosomes from the PPMD confirms that there have been two episodes of melting which record two protracted periods of high temperature deformation. The older period of migmatite crystallization corresponds to melting and deformation associated with the Salmon River suture zone (ca. 145-128 Ma; SRSZ); the younger period of migmatite crystallization corresponds to melting and deformation associated with the formation of the western Idaho shear zone (ca. 104-90 Ma; WISZ). Various cross-cutting relationships observed in the field indicate the PPMD experienced varying deformation conditions during the Cretaceous. The melt-present structures associated with the SRSZ were overprinted by solid-state fabric attributed to deformation during contraction in the SRSZ. During WISZ deformation, the PPMD experienced melt-present deformation in the deep crust while the

rest of the WISZ experienced solid-state deformation. The changes in deformation conditions experienced by the PPMD during SRSZ contraction and WISZ transpression, and the gap in migmatization recorded by U-Pb geochronology of zircons from PPMD leucosomes, provide the first structural evidence that the SRSZ is distinct from – and has been overprinted by – the WISZ. Exhumation of the PPMD began by 92 Ma, and WISZ deformation had ceased by the time the PPMD cooled and reached mid-crustal levels.

ACKNOWLEDGEMENTS

This research was supported by a Geological Society of America student research grant to W. Montz, research funds from Boston College to S. Kruckenberg, and by NSF-EAR 1338583 in support of the Arizona LaserChron Center. I thank Basil Tikoff for helpful discussions and insightful comments and that significantly improved upon early versions of this research. I thank Nicholas Cokonis for assistance in the field, and the efforts of Mark Pecha and staff at the Arizona LaserChron Center (Tucson, Arizona) are gratefully acknowledged.

REFERENCES CITED

Armstrong, R.L., Taubeneck, W.H., and Hales, P.O., 1977, Rb-Sr and K-Ar geochronometry of Mesozoic granitic rocks and their Sr isotopic composition: Oregon, Washington, and Idaho: Geological Society of America Bulletin, v. 88, p. 397–411.

Avé Lallemant, H.G., 1995, Pre-Cretaceous tectonic evolution of the Blue Mountains province, northeastern Oregon, *in* Vallier, T.L., and Brooks, H.C., eds., Geology of the Blue Mountains Region of Oregon, Idaho, and Washington: Petrology and Tectonic Evolution of Pre-Tertiary Rocks of the Blue Mountains Region: U.S. Geological Survey Professional Paper 1438, p. 271–304.

Benford, B., Crowley, J., Schmitz, M., Northrup, C.J., and Tikoff, B., 2010, Mesozoic magmatism and deformation in the northern Owyhee Mountains, Idaho: Implications of along-zone variations for the western Idaho shear zone: Lithosphere, v. 2, no. 2, p. 93–11, doi:10.1130/L76.1

Blake, D.E., Gray, K.D., Giorgis, S., and Tikoff, B., 2009, A tectonic transect through the Salmon River suture zone along the Salmon River Canyon in the Riggins region of west-central Idaho, in O'Connor, J.E. and Madin, I.P., eds., Volcanoes to Vineyards: Geologic Field Trips through the Dynamic Landscape of the Pacific Northwest: Geological Society of America Field Guide 15, p. 357–385.

Bonnichsen, W., 1987, Pre-Cenozoic geology of the West Moutain-Council Mountain-New Meadows area, west-central Idaho, in Vallier, T. L. and Brooks, H. C., eds., Geology of the Blue Mountains Region of Oregon, Idaho, and Washington: The

Idaho batholith and its border zone: US Geological Survey Professional Paper 1436, p. 151–170.

Braudy, N., 2013, Deformation history of West Mountain, west-central Idaho: implications for the western Idaho shear zone [Masters thesis]: University of Wisconsin - Madison, Madison, WI.

Braudy, N., Gaschnig, R., Wilford, D., Vervoort, J., Nelson, C.L., Davidson, C., Kahn, M.J., and Tikoff, B., in review, Timing and deformation conditions of the western Idaho shear zone, West Mountain, west-central Idaho: Lithosphere.

Brown, M., 1973, The definition of metatexis, diatexis and migmatite: Proceedings of the Geologists' Association, v. 84, p. 371–382.

Brown, M., 1994, The generation, segregation, ascent and emplacement of granite magma: The migmatite-to-crustally-derived granite connection in thickened orogens: Earth-Science Reviews, v. 36, p. 83–130, doi:10.1016/0012-8252(94)90009-4.

Brown, M., and Solar, G.S., 1998, Shear-zone systems and melts: Feedback relations and self-organization in orogenic belts: Journal of Structural Geology, v. 20, p. 211–227, doi:10.1016/S0191-8141(97)00068-0.

Getty, S.R., Selverstone, J., Wernicke, B.P., Jacobsen, S.B., Aliberti, E., and Lux, D.R., 1993, Sm-Nd dating of multiple garnet growth events in an arc-continent collision zone, northwestern U.S. Cordillera: Contributions to Mineralogy and Petrology, v. 115, p. 45–57.

Giorgis, S. and Tikoff, B., 2004, Constraints on kinematics and strain from feldspar porphyroclast populations., in Alsop, G.I., Holdsworth, R.E., McCaffrey, K.J.W. and

Hand, M., eds., Flow Processes in Faults and Shear Zones: Geological Society, London, Special publication 224, p. 83–100.

Giorgis, S., Tikoff, B., and McClelland, W.C., 2005, Missing Idaho arc: Transpressional modification of the $^{87}Sr/^{86}Sr$ transition on the western edge of the Idaho batholith; Geology, v. 33, p. 469–472, doi:10.1130/G20911.1.

Giorgis, S., McClelland, W., Fayon, A., Singer, B.S., and Tikoff, B., 2008, Timing of deformation and exhumation in the western Idaho shear zone, McCall, Idaho: Geological Society of America Bulletin, v. 120, p. 1119–1133, doi:1030/B26291.1.

Giorgis, S., Michels, Z., Dair, L., Braudy, N., and Tikoff, B., in review, Kinematic and vorticity analyses of the western Idaho shear zone, USA: Lithosphere.

Gray, K.D., and Oldow, J.S., 2005, Contrasting structural histories of the Salmon River belt and Wallowa terrane: Implications for terrane accretion in the northeastern Oregon and west-central Idaho: Geological Society of America Bulletin, v. 117, p. 687–706, doi:10.1130/B25411.1.

Grey, K.D., Watkinston, J.A., Gaschnig, R.M., and Isakson, V.H., 2012, Age and structure of the Crevice pluton: overlapping orogens in west-central Idaho?: Canadian Journal of Earth Science, v. 49, p. 707–731, doi:10.1139/E2012-016.

Hamilton, W.R., 1963, Overlapping of late Mesozoic orogens in western Idaho: Geologic Society of America Bulletin, v. 74, p. 779–788, doi: 10.1130/0016-7606(1963)74[779:OOLMOI]2.0.CO;2

Hamilton, W.R., 1969, Reconnaissance geologic map of the Riggins quadrangle, west-central Idaho: U.S. Geological Survey Map I-579, scale, 1:125,000.

Holness, M., 2008, Decoding migmatite microstructures, *in* Sawyer, E.W., and Brown, M., eds., Working with Migmatites, Short Course Series: Mineralogical Association of Canada, Quebec, Quebec, Canada, v. 38, p. 57–76,

Kurz, G.A., Schmitz, M.D., Northrup, C.J., and Vallier, T.L., 2012, U-Pb geochronology and geochemistry of intrusive rocks from the Cougar Creek Complex, Wallowa arc terrane, Blue Mountains Province, Oregon-Idaho: Geological Society of America Bulletin, v. 124, p. 578–595, doi:10.1130/B30452.1.

Lamaskin, T.A., Dorsey, R.J., Vervoort, J., Schmitz, M.D., Tumpane, K.P, and Moore, N.O., 2015, Westward growth of Laurentia by pre-late Jurassic terrane accretion, easter Oregon and western Idaho, United States: Journal of Geology, v. 123, p. 233–267, doi:10.1086/861724.

Lewis, R.S., Burmester, R.F., Kauffman, J.D., Breckenridge, R.M., Schmidt, K.L., McFaddan, M.D., and Myers, P.E., 2007, Geologic map of the Kooskia 30 x 60 minute quadrangle,Idaho: Idaho Geological Survey Digital Web Map 93, scale 1:100,000.

Lewis, R.S., Schmidt, K.L., Gaschnig, R.M., LaMaskin, T.A., Lund, K., Gray, K.D., Tikoff, B., Stetson-Lee, T., Moore, N., 2014, Hells Canyon to the Bitterroot front: A transect from the accretionary margin eastward across the Idaho batholith: Geological Society of America Field Guide 37, 50 p.

Ludwig, K.R., 2012, User's Manual for Isoplot 3.75: A geochronological toolkit for Microsoft Excel: Berkeley Geochronology Center Special Publication, v. 5, 75 p.

Lund, K., and Snee, L.W., 1988, Metamorphism, structural development, and age of the continent-island arc junction in west-central Idaho, *in* Ernst, W.G., ed.,

Metamorphism and Crustal Evolution, Western Conterminous United States: Englewood Cliffs, New Jersey, Prentice Hall, p. 296–331.

Manduca, C.A., Kuntz, M.A., and Silver, L.T., 1993, Emplacement and deformation history of the western margin of the Idaho batholith near McCall, Idaho: Influence of a major terrane boundary: Geological Society of America Bulletin, v. 105, no. 6, p. 749–765.

Marchildon, N., and Brown, M., 2002, Grain-scale melt distribution in two contact aureole rocks: Implications for controls on melt localization and deformation: Journal of Metamorphic Geology, v. 20, p. 381–396, doi: 10.1046/j.1525-1314.2002.00376.x.

Marchildon, N., and Brown, M., 2003, Spatial distribution of melt-bearing structures in anatectic rocks from Southern Brittany, France: Implications for melt transfer at grain- to orogen-scale: Tectonophysics, v. 364, p. 215–235, doi: 10.1016/S0040-1951(03)00061-1.

McClelland, W.C., and Oldow, J.S., 2007, Late Cretaceous truncation of the western Idaho shear zone in the central North American Cordillera: Geology, v. 35, no. 8, p. 723–726, doi:10.1130/G23623A.1

McLellan, E.L., 1988, Migmatite structures in the Central Gneiss Complex, Boca de Quadra, Alaska: Journal of Metamorphic Geology, v. 6(4), p. 517–542, doi:10.1111/j.1525-1314.1988.tb00437.x.

McClelland, W.C., Tikoff, B., and Manduca, C.A., 2000, Two-phase evolution of accretionary margins: examples from the North American Cordillera: Tectonophysics, v. 326, p. 37–55.

Mehnert, K. R., 1968, Migmatites and the Origin of Granitic Rocks: New York, Elsevier Sci., 393 p.

Mitchell, V.E. and Bennett, E.H., 1979, Geologic map of the Baker Quadrangle, Idaho: Idaho Bureau of Mines Geology, Department of lands, scale 1:250,000.

Sawyer, E. W., 1994, Melt segregation in the continental crust: Geology, v. 22, p. 1019–1022.

Sawyer, E. W., 2001, Melt segregation in the continental crust: Distribu- tion and movement of melt in anatectic rocks, Journal of Metamorphic Geology, v. 19, p. 291–309, doi:10.1046/j.0263-4929.2000.00312.x.

Sawyer, E. W., 2008, Working with migmatites: Nomenclature for the constituent parts, *in* Sawyer, E.W., and Brown, M., eds., Working with Migmatites, Short Course Series: Mineralogical Association of Canada, Quebec, Quebec, Canada, v. 38, p. 1–28

Schmidt, K.L., Lewis, R.S., Vervoort, J., Stetson-Lee, T.A., Michels, Z.D., Tikoff, B., in review, Tectonic evolution of the Syringa embayment in the central North American Cordilleran accretionary boundary: Lithosphere

Schwartz, J.J., Snoke, A.W., Frost, C.D., Barnes, C.G., Gromet, L.P., and Johnson, K., 2010, Analysis of the Wallowa-Baker terrane boundary: Implications for tectonic accretion in the Blue Mountains province, northeastern Oregon: Geological Society of America Bulletin, v. 122, p. 517–536, doi:10.1130/B26493.1.

Schwartz, J.J., Snoke, A.W., Cordey, F., Johnson, K., Frost, C.D., Barnes, C.G., LaMaskin, T.A., and Wooden, J.L., 2011, Late Jurassic magmatism, metamorphism and deformation in the Blue Mountains province, northeast Oregon: Geological Society of America Bulletin, v. 123, p. 2083–2111, doi:10.1130/B30327.1.

Selverstone, J., Wernicke, B., and Aliberti, E., 1992, Intracontinental subduction and hinged uplift along the Salmon River suture zone in west central Idaho. Tectonics, v. 11, pp. 124–144.

Snee, L.W., Lund, K., Sutter, J.G., Balcer, D.E., and Evans, K.V., 1995, An $^{40}Ar/^{39}Ar$ chronicle of the tectonic development of the Salmon River suture zone, western Idaho, *in* Vallier, T.L., and Brooks, H.C., eds., Geology of the Blue Mountains Region of Oregon, Idaho, and Washington: Petrology and Tectonic Evolution of Pre-Tertiary Rocks of the Blue Mountains Retions: U.S. Geological Survey Professional Paper 1438, p. 359–414.

Tikoff, B., Kelso, P., Manduca, C.A., Markley, M.J. and Gillaspy, J., 2001, Lithospheric and crustal reactivation of an ancient plate boundary; the assembly and disassembly of the Salmon River suture zone, Idaho, USA: Geological Society Special Publications, v. 186, p. 213–231.

Unruh, D.M., Lund, K., Kuntz, M.E., and Snee, L.W., 2008, Uranium-lead zircon ages and Sr, Nd, and Pb isotope geochemistry of selected pluton rocks from western Idaho: U.S. Geological Survey Open-File Report, 2008-1142, 36 p.

Vallier, T.L., 1995, Petrology of pre-Tertiary igneous rocks in the Bout Mountains retion of Oregon, Idaho, and Washington; implications for the geologic evolution of a complex island arc, *in* Vallier, T.L., and Brooks, H.C., eds., Geology of the Blue Mountains Region of Oregon, Idaho, and Washington: Petrology and Tectonic Evolution of Pre-Tertiary Rocks of the Blue Mountains Retions: U.S. Geological Survey Professional Paper 1438, p. 125–209.

Vanderhadghe, O., 2001, Melt segregation, pervasive melt migration and magma mobility in the continental crust: the structural record from pores to orogens: Physics and Chemistry of the Earth, Part A: Solid Earth and Geodesy, v. 26, p. 213–223.

Vanderhaeghe, O., 2009, Migmatites, granites and orogeny: Flow modes of partially molten rocks and magmas associated with melt/solid segregation in orogenic belts: Tectonophysics, v. 477, p. 119–134, doi:10.1016/j.tecto. 2009.06.021.

Walker, N.W., 1989, U-Pb geochronologic and petrologic studies of the Blue Mountains terrane, northeastern Oregon and west-central Idaho—Implications for pre-Tertiary tectonic evolution [Ph.D. thesis]: Santa Barbara, University of California, 224 p.

Weinberg, R.F., and Mark, G., 2008, Magma migration, folding, and disaggregation of migmatites in the Karakoram Shear Zone, Ladakh, NW India: Geological Society of America Bulletin, v. 120, n. 7/8, p. 994-1009.

Wickham, S. M., 1987, The segregation and emplacement of granitic magmas: Journal of the Geological Society, v. 144, p. 281–297, doi:10.1144/gsjgs.144.2.0281.

Wilford, D.E., 2012, Lu-Hf garnet geochronology of the Salmon River suture zone, west-central Idaho [M.S. thesis]: Washington State University, Pullman, WA, 97 p.

FIGURES

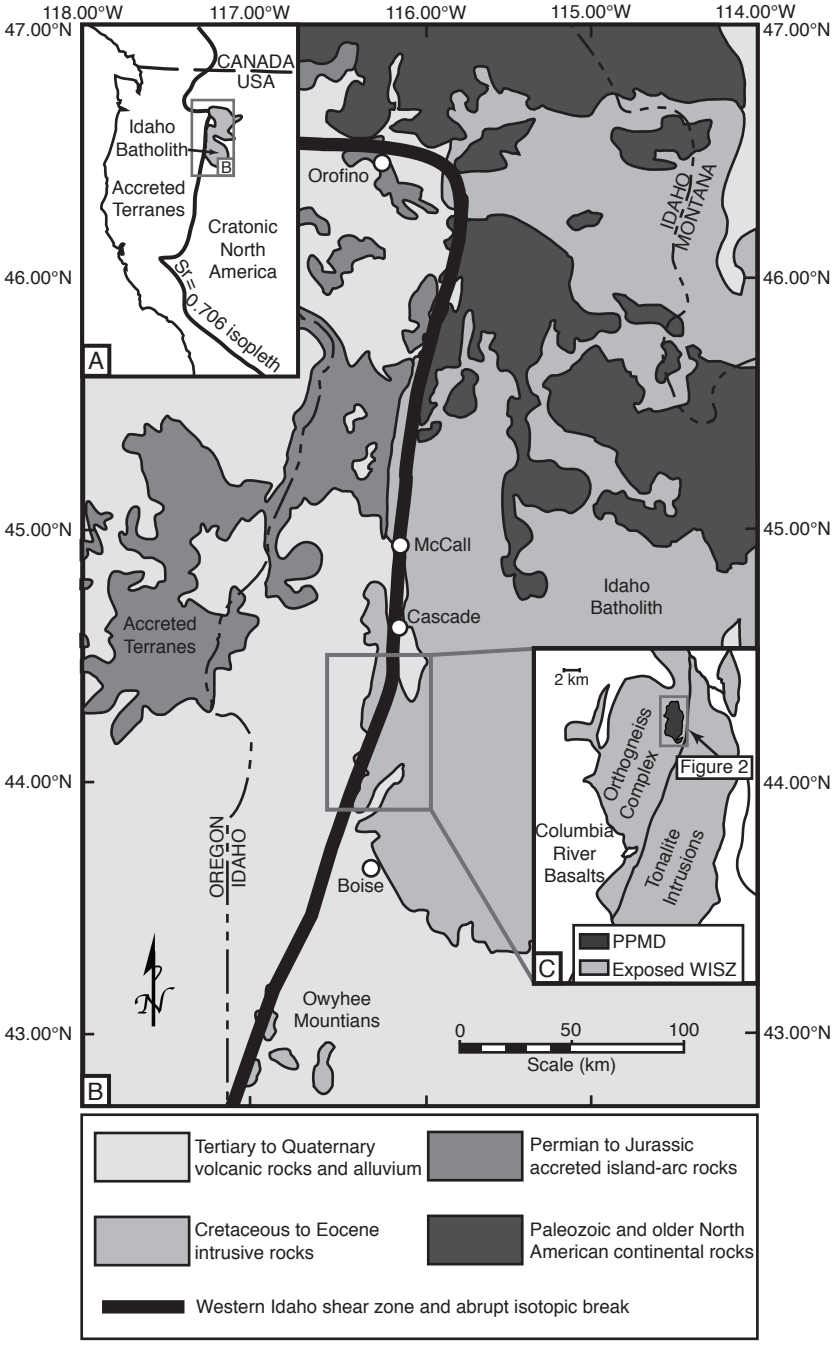

Figure 1

Figure 1. Location of the western Idaho shear zone and the Potters Pond migmatite domain (PPMD) in the North American cordillera. (A) Trace of the initial 87Sr/86Sr 0.706 isopleth in the North American cordillera marks the extent of accreted oceanic terranes against the North American craton. (B) The western Idaho shear zone (WISZ) is a ~5 km wide high strain zone that follows the initial 87Sr/86Sr 0.706 isopleth in western Idaho (modified from Tikoff et al., 2001). C. The PPMD is located southwest of Cascade, Idaho. Its location coincides with the primary bend in the orientation of WISZ fabric. (Modified from Braudy et al., in review).

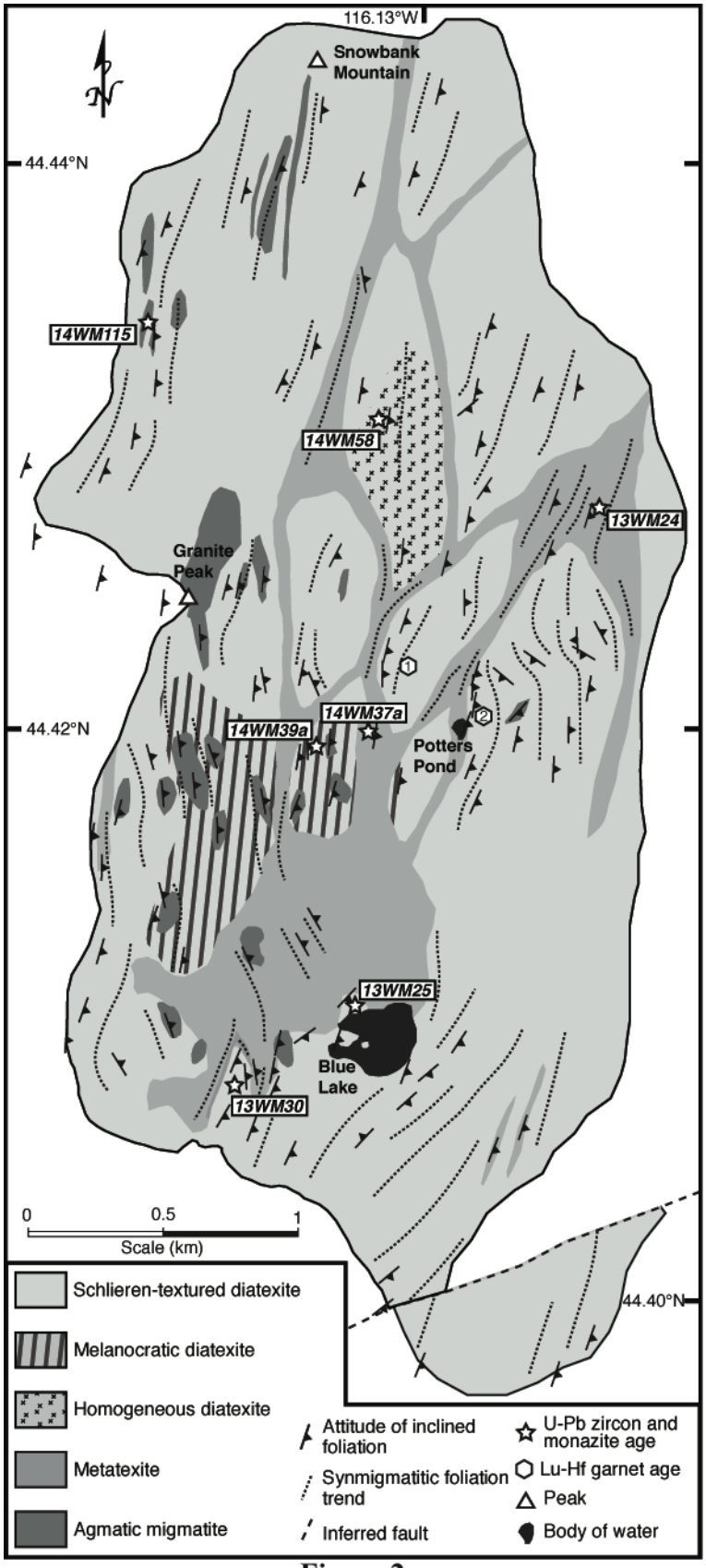
116.13°W
Snowbank Mountain
44.44°N
14WM115
14WM58
13WM24
Granite Peak
44.42°N
14WM39a
14WM37a
Potters Pond
13WM25
Blue Lake
13WM30
0
0.5
1
Scale (km)
44.40°N
Schlieren-textured diatexite
Melanocratic diatexite
Homogeneous diatexite
Metatexite
Agmatic migmatite
Attitude of inclined foliation
Synmigmatitic foliation trend
Inferred fault
U-Pb zircon and monazite age
Lu-Hf garnet age
Peak
Body of water

Figure 2

Figure 2. Map of the Potters Pond migmatite domain showing distribution of migmatite morphologies, trend of synmigmatitic foliation, and locations of samples collected for U-Pb geochronology. Hexagons represent the locations of samples collected for Lu-Hf garnet geochronology (1: sample 11NB377; 2: sample 11NB379) (Braudy et al., in review).

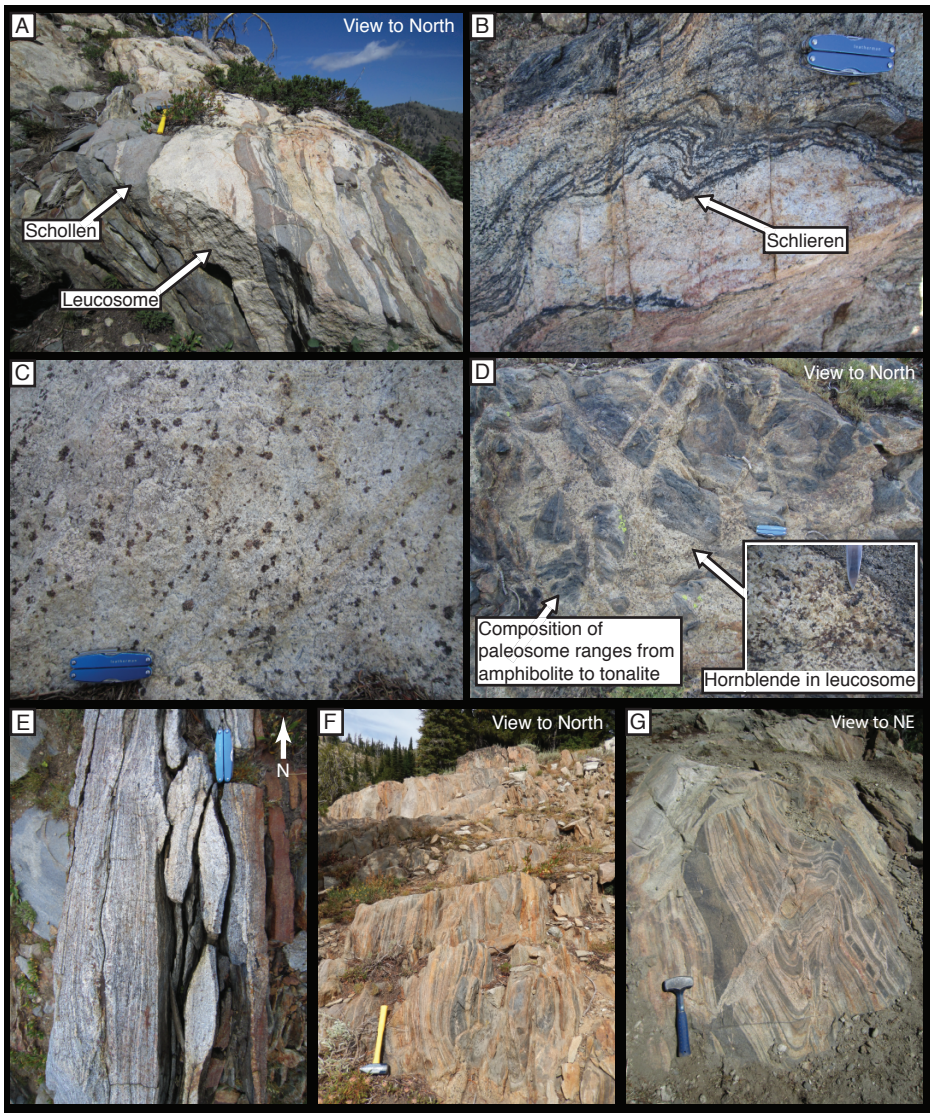
A
View to North
Schollen
Leucosome
B
Schlieren
C
D
View to North
Composition of paleosome ranges from amphibolite to tonalite
Hornblende in leucosome
E
N
F
View to North
G
View to NE

Figure 3

Figure 3. Representative field photographs of migmatites in the Potters Pond migmatite domain (PPMD). (A) Diatexite with gneissic and amphibolite schollen parallel to and defining synmigmatitic layering. (B) Wispy biotite schlieren characteristic of diatexite in the PPMD. (C) Leucocratic nebulite with garnet clusters concentrated in faint leucosomes. (D) Agmatic migmatite. Note that the biotite- and hornblende-bearing leucosomes lack garnet. (E) Boudinaged leucosome within melanocratic diatexite. (F) Planar stromatic metatexite. (G) Folded stromatic metatexite.

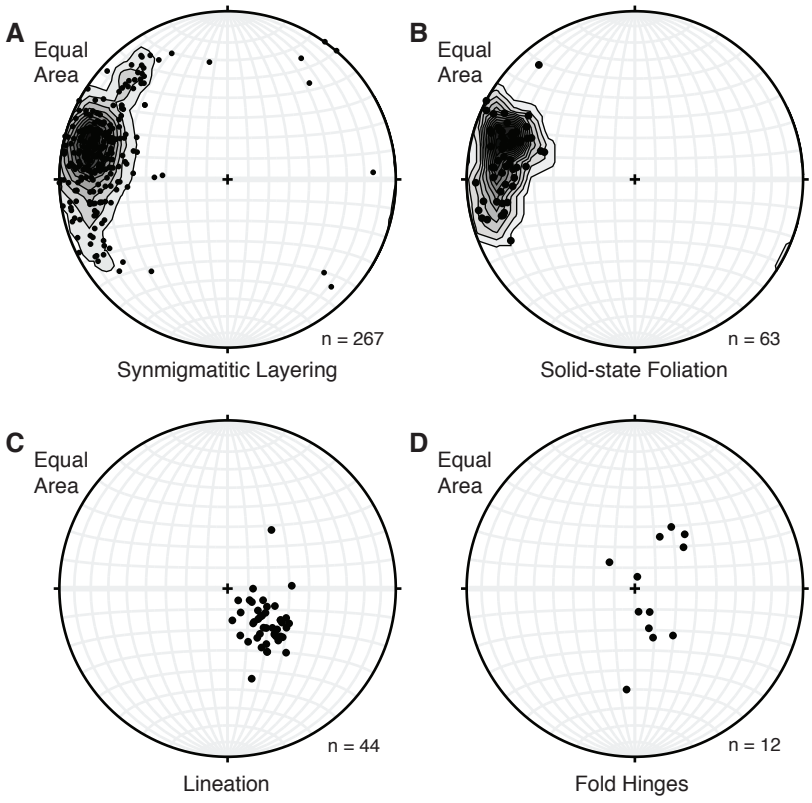
A
Equal
Area
n = 267
Synmigmatitic Layering
B
Equal
Area
n = 63
Solid-state Foliation
C
Equal
Area
n = 44
Lineation
D
Equal
Area
n = 12
Fold Hinges

Figure 4

Figure 4. Lower-hemisphere equal-area net plots of (A) poles to synmigmatitic layering, (B) poles to solid state foliation, (C) lineation, and (D) fold hinges measured from migmatites in the PPMD. Both synmigmatitic layering and solid-state foliation trend dominantly towards ~015°, and lineation is typically down dip. Orientation of fold hinges generally corresponds to lineation orientation.

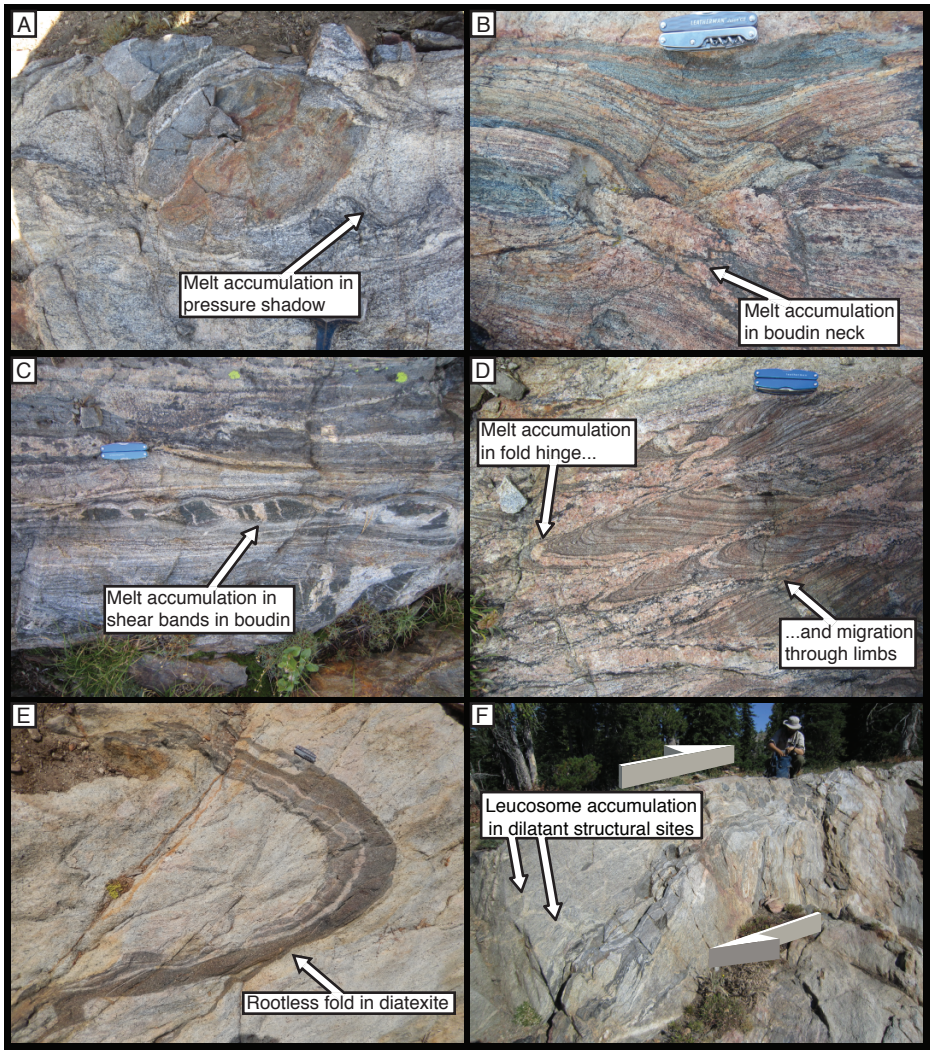
A
Melt accumulation in pressure shadow
B
Melt accumulation in boudin neck
C
Melt accumulation in shear bands in boudin
D
Melt accumulation in fold hinge...
...and migration through limbs
E
Rootless fold in diatexite
F
Leucosome accumulation in dilatant structural sites

Figure 5

Figure 5. Evidence of melt-present deformation is recorded by migmatites in the PPMD. During deformation, migrating melt preferentially accumulates in dilatant structural sites: (A) Melt accumulation preserved in the pressure shadow of block of paleosome rotated during shearing. (B) Accumulation of melt preserved in boudin necks of paleosome within the stromatic metatexite. (C) Melt preserved in boudin necks and shear bands within boudins. (D) Flanking structures in folded migmatites. (D) Melt accumulation in the hinge region of rootless fold in schlieren-textured diatexite. (E) Small shear zone within the PPMD with melt accumulation preserved in dilatant structural sites.

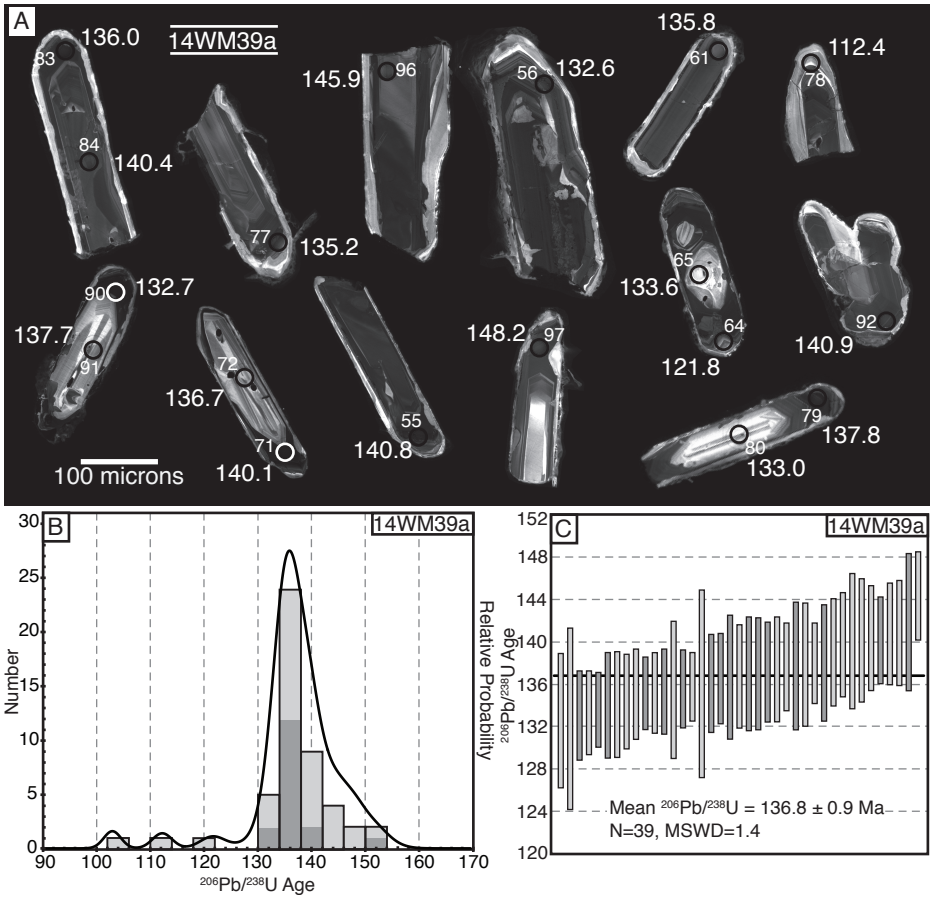
A
14WM39a
136.0
83
84
140.4
145.9
96
56
132.6
135.8
61
112.4
78
77
135.2
65
133.6
64
121.8
92
140.9
90
132.7
137.7
91
72
136.7
71
140.1
55
140.8
148.2
97
79
137.8
80
133.0
100 microns
B
14WM39a
Number
Relative Probability
206Pb/238U Age
C
14WM39a
206Pb/238U Age
Mean 206Pb/238U = 136.8 ± 0.9 Ma
N=39, MSWD=1.4

Figure 6

Figure 6. Cathodoluminescence images of representative zircon grains dated using the laser ablation – inductively coupled plasma – mass spectrometer (LA-ICP-MS) for sample 14WM39a (boudinaged leucosome within melanocratic diatexite). Small numbers refer spot number in Table DR1. Larger numbers are 206Pb/238U ages in Ma for individual spot analyses (see Table DR1 for corresponding error on spot analyses). (B) Probability density plots with stacked histogram of 206Pb/238U ages from zircon in sample 14WM39a. Light gray bars represent rim analyses and dark gray bars represent core analyses. (C) Weighted mean 206Pb/238U age calculation and uncertainty is given at 95% confidence limits. Light and dark gray bars represent rim and core analyses, respectively. Plots and calculations based on Isoplot of Ludwig (2012).

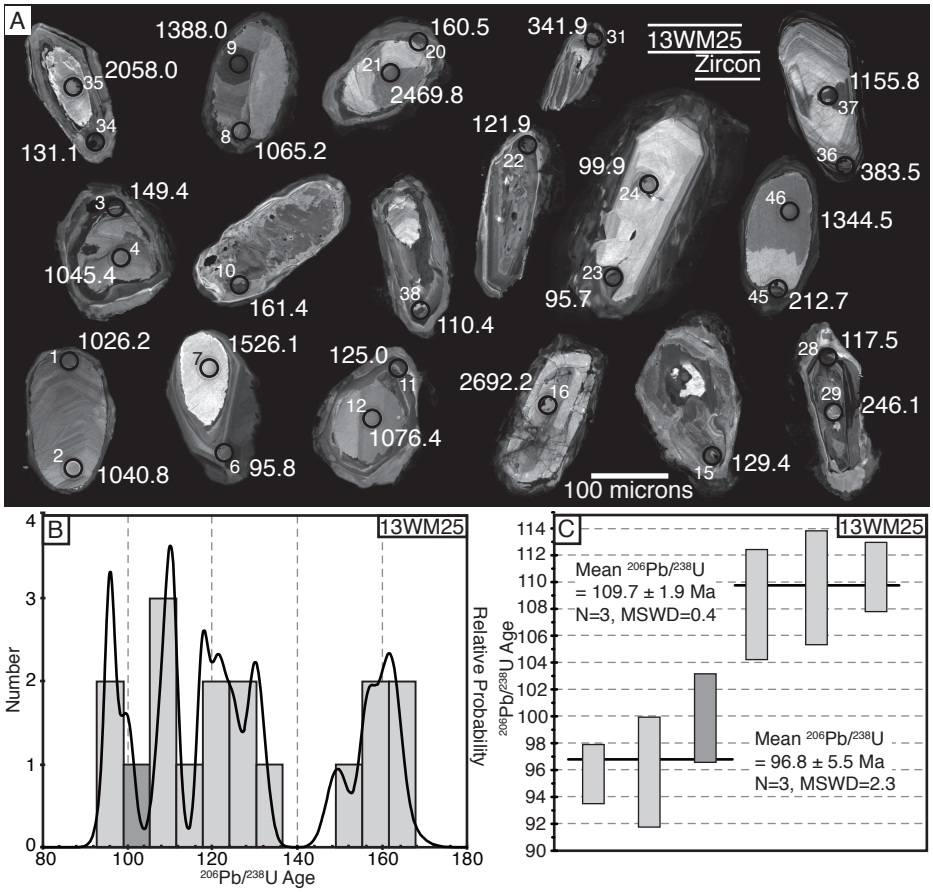
A
13WM25
Zircon
1388.0
2058.0
131.1
1065.2
160.5
2469.8
341.9
1155.8
383.5
121.9
99.9
149.4
1045.4
161.4
110.4
95.7
1344.5
212.7
1026.2
1526.1
125.0
2692.2
1076.4
1040.8
95.8
129.4
117.5
246.1
100 microns
B
13WM25
Number
Relative Probability
206Pb/238U Age
C
13WM25
Mean 206Pb/238U
= 109.7 ± 1.9 Ma
N=3, MSWD=0.4
Mean 206Pb/238U
= 96.8 ± 5.5 Ma
N=3, MSWD=2.3
206Pb/238U Age

Figure 7

Figure 7. (A) Cathodoluminescence images of representative zircon grains dated using the laser ablation – inductively coupled plasma – mass spectrometer (LA-ICP-MS) for sample 13WM25 (schlieren-textured granodiorite diatexite). Small numbers refer spot number in Table DR1. Larger numbers are 206Pb/238U ages in Ma for individual spot analyses (see Table DR1 for corresponding error on spot analyses). (B) Probability density plots with stacked histogram of 206Pb/238U ages from zircon in sample 13WM25. Light gray bars represent rim analyses and dark gray bars represent core analyses. (C) Weighted mean 206Pb/238U age calculation and uncertainty is given at 95% confidence limits. Light and dark gray bars represent rim and core analyses, respectively. Plots and calculations based on Isoplot of Ludwig (2012).

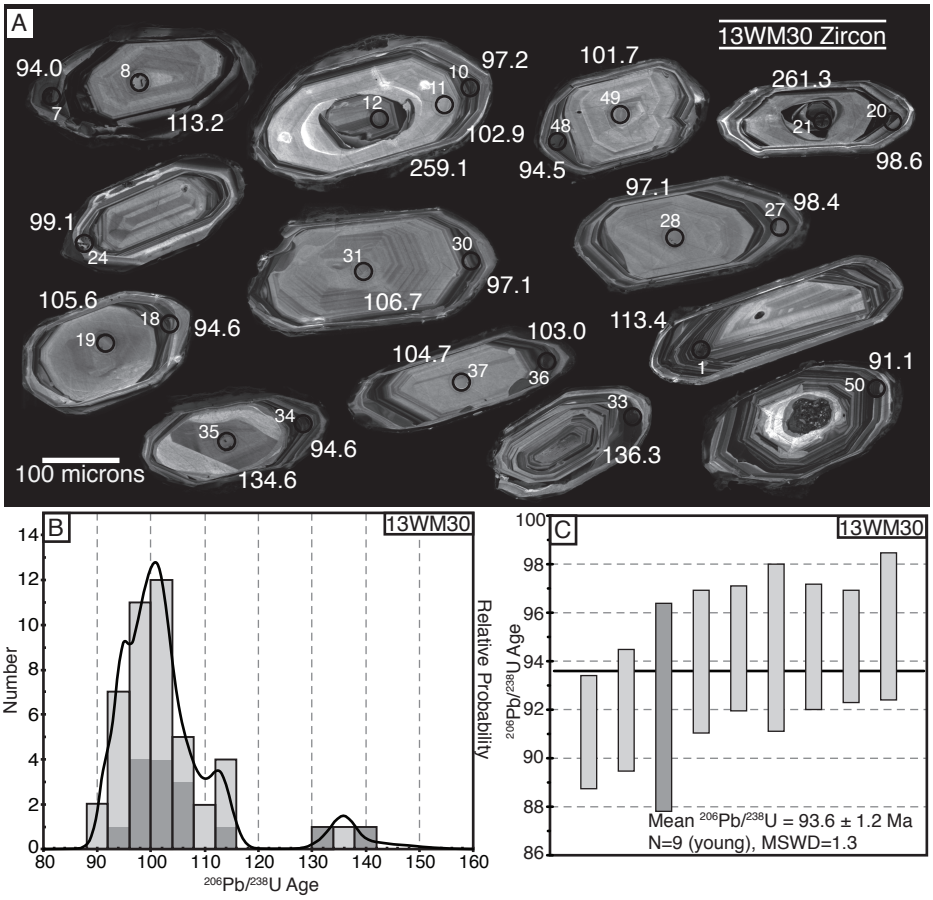
A
13WM30 Zircon
94.0
8
7
113.2
97.2
10
11
12
102.9
259.1
101.7
49
48
94.5
261.3
20
21
98.6
99.1
24
97.1
28
27
98.4
31
30
106.7
97.1
105.6
18
19
94.6
103.0
113.4
1
91.1
50
104.7
37
36
33
136.3
35
34
94.6
134.6
100 microns
B
13WM30
Number
Relative Probability
206Pb/238U Age
C
13WM30
206Pb/238U Age
Mean 206Pb/238U = 93.6 ± 1.2 Ma
N=9 (young), MSWD=1.3

Figure 8

Figure 8. (A) Cathodoluminescence images of representative zircon grains dated using the laser ablation – inductively coupled plasma – mass spectrometer (LA-ICP-MS) for sample 13WM30 (Schlieren-textured granodiorite diatexite). Small numbers refer spot number in Table DR1. Larger numbers are 206Pb/238U ages in Ma for individual spot analyses (see Table DR1 for corresponding error on spot analyses). (B) Probability density plots with stacked histogram of 206Pb/238U ages from zircon in sample 13WM30. Light gray bars represent rim analyses and dark gray bars represent core analyses. (C) Weighted mean 206Pb/238U age calculation and uncertainty is given at 95% confidence limits. Light and dark gray bars represent rim and core analyses, respectively. Plots and calculations based on Isoplot of Ludwig (2012).

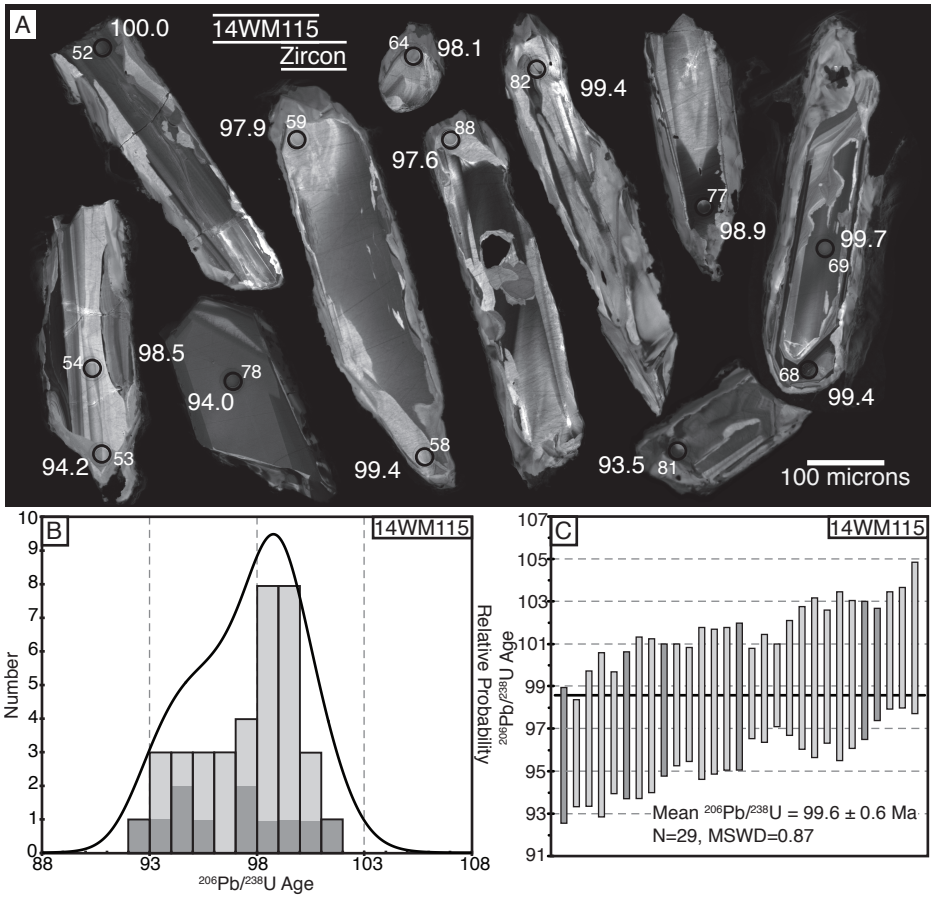
A
14WM115
Zircon
100.0
52
64
98.1
82
99.4
97.9
59
88
97.6
77
98.9
99.7
69
54
98.5
78
94.0
68
99.4
94.2
53
99.4
58
93.5
81
100 microns
B
14WM115
Number
Relative Probability
206Pb/238U Age
C
14WM115
206Pb/238U age
Mean 206Pb/238U = 99.6 ± 0.6 Ma
N=29, MSWD=0.87

Figure 9

Figure 9. (A) Cathodoluminescence images of representative zircon grains dated using the laser ablation – inductively coupled plasma – mass spectrometer (LA-ICP-MS) for sample 14WM115 (agmatic migmatite). Small numbers refer spot number in Table DR1. Larger numbers are 206Pb/238U ages in Ma for individual spot analyses (see Table DR1 for corresponding error on spot analyses). (B) Probability density plots with stacked histogram of 206Pb/238U ages from zircon in sample 14WM115. Light gray bars represent rim analyses and dark gray bars represent core analyses. (C) Weighted mean 206Pb/238U age calculation and uncertainty is given at 95% confidence limits. Light and dark gray bars represent rim and core analyses, respectively. Plots and calculations based on Isoplot of Ludwig (2012).

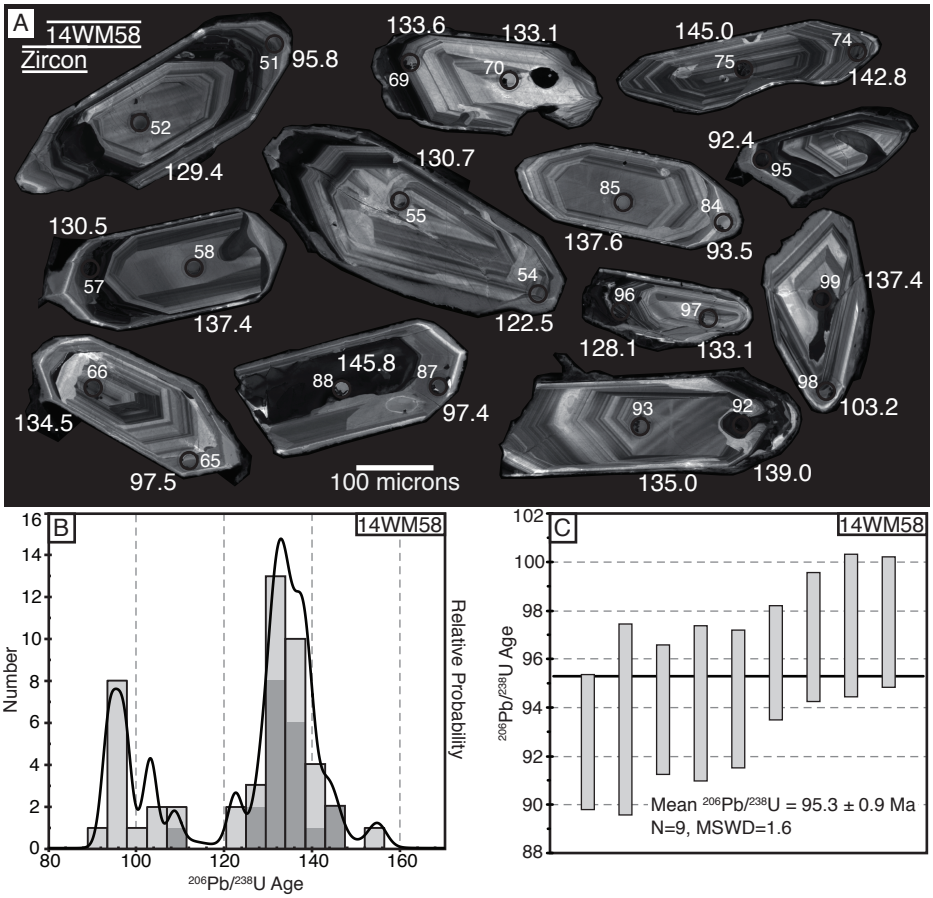
A
14WM58
Zircon
51
95.8
52
129.4
133.6
69
133.1
70
145.0
74
75
142.8
130.7
55
92.4
95
85
84
137.6
93.5
130.5
58
57
137.4
54
122.5
96
97
128.1
133.1
99
137.4
98
103.2
66
134.5
65
97.5
145.8
88
87
97.4
93
92
135.0
139.0
100 microns
B
14WM58
Number
Relative Probability
206Pb/238U Age
C
14WM58
206Pb/238U Age
Mean 206Pb/238U = 95.3 ± 0.9 Ma
N=9, MSWD=1.6

Figure 10

Figure 10. (A) Cathodoluminescence images of representative zircon grains dated using the laser ablation – inductively coupled plasma – mass spectrometer (LA-ICP-MS) for sample 14WM58 (Nebulitic diatexite). Small numbers refer spot number in Table DR1. Larger numbers are 206Pb/238U ages in Ma for individual spot analyses (see Table DR1 for corresponding error on spot analyses). (B) Probability density plots with stacked histogram of 206Pb/238U ages from zircon in sample 14WM58. Light gray bars represent rim analyses and dark gray bars represent core analyses. (C) Weighted mean 206Pb/238U age calculation and uncertainty is given at 95% confidence limits. Light and dark gray bars represent rim and core analyses, respectively. Plots and calculations based on Isoplot of (2012).

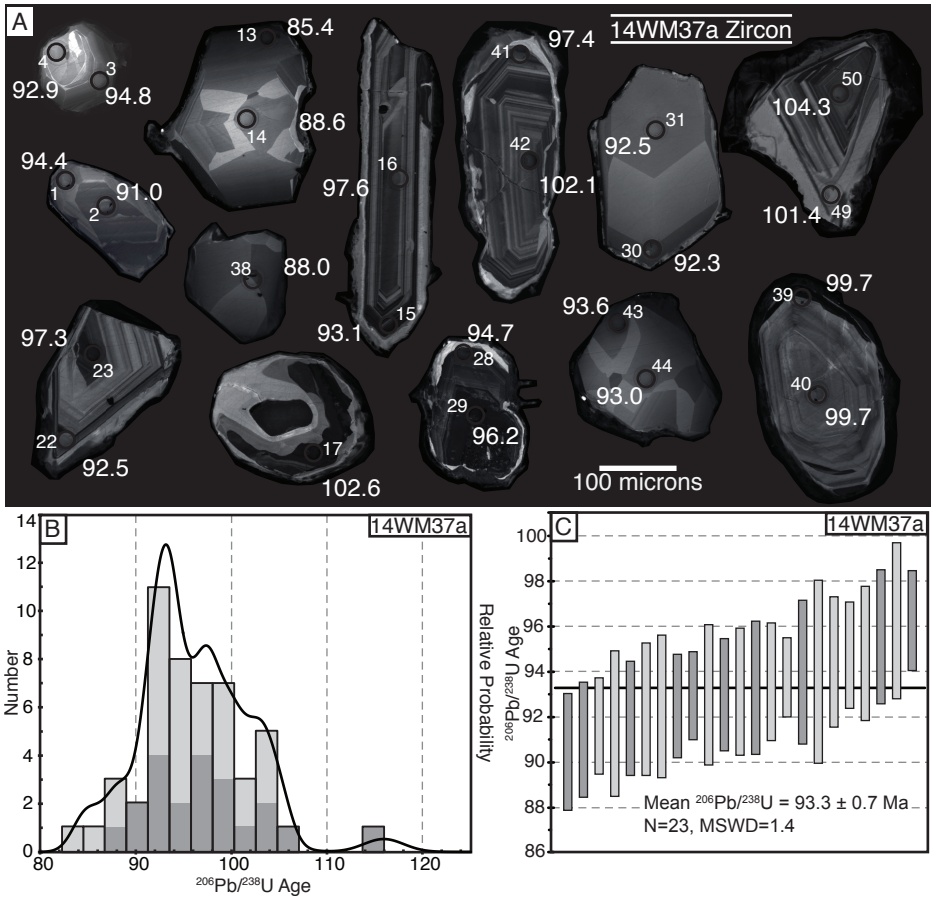
A
14WM37a Zircon
92.9
94.8
85.4
88.6
94.4
91.0
97.6
88.0
97.4
102.1
92.5
104.3
101.4
92.3
99.7
93.6
93.1
94.7
97.3
92.5
102.6
96.2
93.0
99.7
100 microns
B
14WM37a
Number
Relative Probability
206Pb/238U Age
C
14WM37a
206Pb/238U Age
Mean 206Pb/238U = 93.3 ± 0.7 Ma
N=23, MSWD=1.4

Figure 11

Figure 11. (A) Cathodoluminescence images of representative zircon grains dated using the laser ablation – inductively coupled plasma – mass spectrometer (LA-ICP-MS) for sample 14WM37a (discordant leucosome in stromatic metatexite). Small numbers refer spot number in Table 1. Larger numbers are 206Pb/238U ages in Ma for individual spot analyses (see Table 1 for corresponding error on spot analyses). (B) Probability density plots with stacked histogram of 206Pb/238U ages from zircon in sample 14WM37a. Light gray bars represent rim analyses and dark gray bars represent core analyses. (C) Weighted mean 206Pb/238U age calculation and uncertainty is given at 95% confidence limits. Light and dark gray bars represent rim and core analyses, respectively. Plots and calculations based on Isoplot of Ludwig (2012).

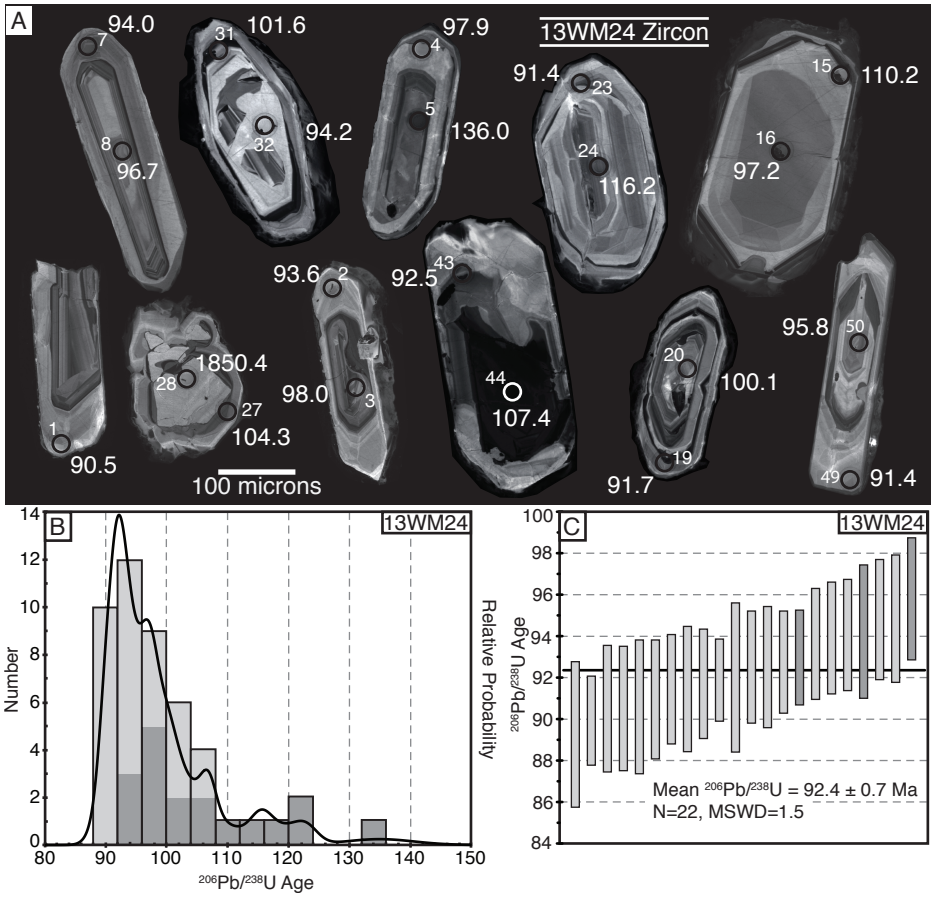
A
13WM24 Zircon
94.0
101.6
97.9
91.4
110.2
94.2
136.0
96.7
116.2
97.2
93.6
92.5
95.8
1850.4
98.0
100.1
104.3
107.4
90.5
91.7
91.4
100 microns
B
13WM24
Number
Relative Probability
206Pb/238U Age
C
13WM24
206Pb/238U Age
Mean 206Pb/238U = 92.4 ± 0.7 Ma
N=22, MSWD=1.5

Figure 12

Figure 12. (A) Cathodoluminescence images of representative zircon grains dated using the laser ablation – inductively coupled plasma – mass spectrometer (LA-ICP-MS) for sample 13WM24 (leucosome in stromatic metatexite). Small numbers refer spot number in Table 1. Larger numbers are 206Pb/238U ages in Ma for individual spot analyses (see Table 1 for corresponding error on spot analyses). (B) Probability density plots with stacked histogram of 206Pb/238U ages from zircon in sample 13WM24. Light gray bars represent rim analyses and dark gray bars represent core analyses. (C) Weighted mean 206Pb/238U age calculation and uncertainty is given at 95% confidence limits. Light and dark gray bars represent rim and core analyses, respectively. Plots and calculations based on Isoplot of Ludwig (2012).

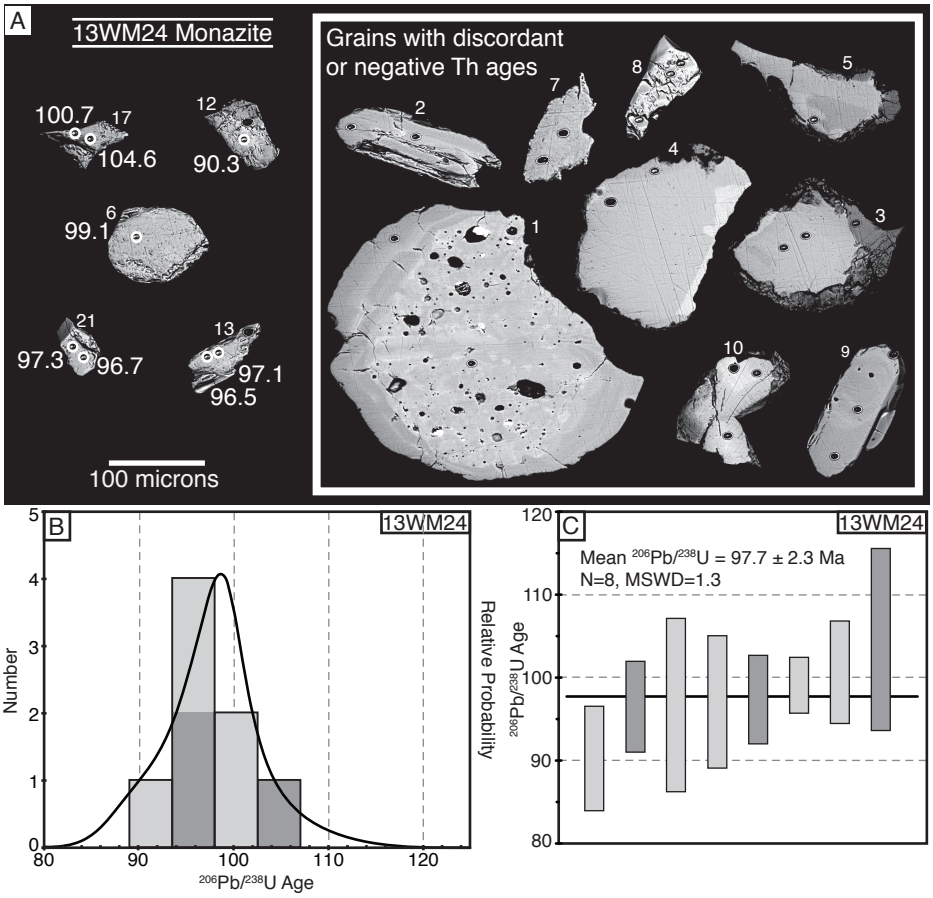
A
13WM24 Monazite
100.7
17
104.6
12
90.3
6
99.1
21
97.3
96.7
13
97.1
96.5
100 microns
Grains with discordant
or negative Th ages
2
7
8
5
4
1
3
10
9
B
13WM24
Number
Relative Probability
206Pb/238U Age
C
13WM24
Mean 206Pb/238U = 97.7 ± 2.3 Ma
N=8, MSWD=1.3
206Pb/238U Age

Figure 13

Figure 13. (A) Back-scattered electron (BSE) images of represented monazite grains dated using the laser ablation – inductively coupled plasma – mass spectrometer (LA-ICP-MS) for sample 13WM24 (leucosome in stromatic metatexite). Small numbers refer to grain number designations in Table 2. Larger numbers are 206Pb/238U ages in Ma for individual spot analyses (see Table 2 for corresponding error on spot analyses). (B) Probability density plot with stacked histogram of 206Pb/238U ages from monazite in sample 13WM24. Light gray bars represent rim analyses and dark gray bars represent core analyses. (C) Weighted average age plot of monazite from sample 13WM24; the weighted mean 206Pb/238U age calculation and uncertainty is given at 95% confidence limits. Light and dark gray bars represent rim and core analyses, respectively. Plots and calculations based on Isoplot of Ludwig (2012).

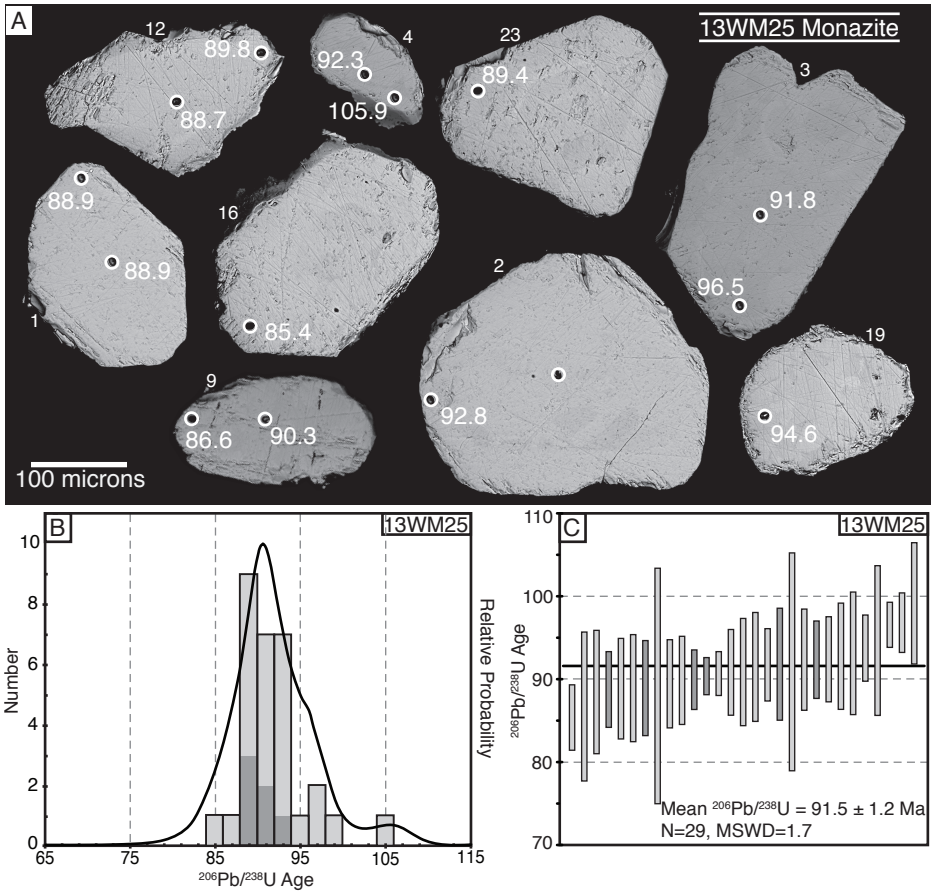
A
13WM25 Monazite
12
89.8
88.7
4
92.3
105.9
23
89.4
3
91.8
88.9
16
88.9
1
85.4
2
96.5
19
9
86.6
90.3
92.8
94.6
100 microns
B
13WM25
Number
Relative Probability
206Pb/238U Age
C
13WM25
206Pb/238U Age
Mean 206Pb/238U = 91.5 ± 1.2 Ma
N=29, MSWD=1.7

Figure 14

Figure 14. (A) Back-scattered electron (BSE) images of represented monazite grains dated using the laser ablation – inductively coupled plasma – mass spectrometer (LA-ICP-MS) for sample 13WM25 (leucosome in stromatic metatexite). Small numbers refer to grain number designations in Table 2. Larger numbers are 206Pb/238U ages in Ma for individual spot analyses (see Table 2 for corresponding error on spot analyses). (B) Probability density plot with stacked histogram of 206Pb/238U ages from monazite in sample 13WM25. Light gray bars represent rim analyses and dark gray bars represent core analyses. (C) Weighted average age plot of monazite from sample 13WM25; the weighted mean 206Pb/238U age calculation and uncertainty is given at 95% confidence limits. Light and dark gray bars represent rim and core analyses, respectively. Plots and calculations based on Isoplot of Ludwig (2012).

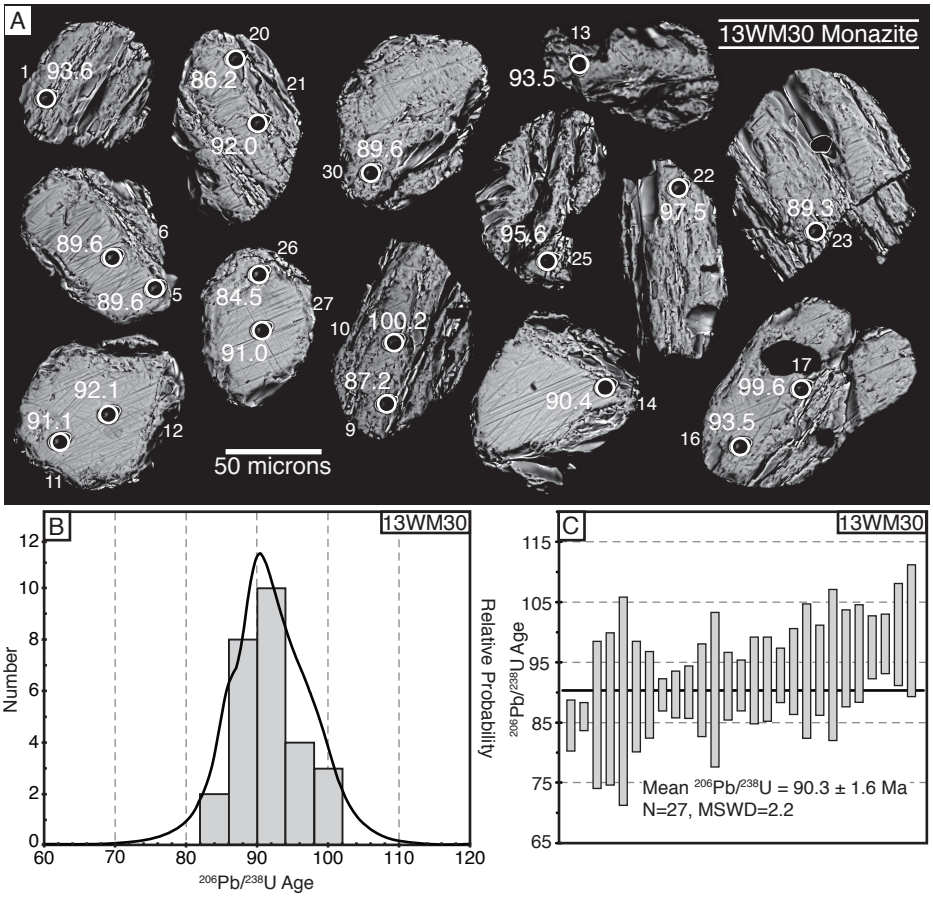
A
13WM30 Monazite
1
93.6
20
86.2
21
92.0
89.6
30
13
93.5
22
97.5
89.3
23
95.6
25
89.6
6
89.6
5
26
84.5
27
91.0
10
100.2
87.2
9
92.1
91.1
12
11
50 microns
90.4
14
17
99.6
93.5
16
B
13WM30
Number
Relative Probability
$^{206}Pb/^{238}U$ Age
C
13WM30
$^{206}Pb/^{238}U$ Age
Mean $^{206}Pb/^{238}U$ = 90.3 ± 1.6 Ma
N=27, MSWD=2.2

Figure 15

Figure 15. (A) Back-scattered electron (BSE) images of represented monazite grains dated using the laser ablation – inductively coupled plasma – mass spectrometer (LA-ICP-MS) for sample 13WM30 (schlieren-textured granodiorite diatexite). Small numbers refer to spot number designations in Table 2. Larger numbers are 206Pb/238U ages in Ma for individual spot analyses (see Table 2 for corresponding error on spot analyses). (B) Probability density plot with stacked histogram of 206Pb/238U ages from monazite in sample 13WM30. Light gray bars represent rim analyses and dark gray bars represent core analyses. (C) Weighted average age plot of monazite from sample 13WM30; the weighted mean 206Pb/238U age calculation and uncertainty is given at 95% confidence limits. Light and dark gray bars represent rim and core analyses, respectively. Plots and calculations based on Isoplot of Ludwig (2012).

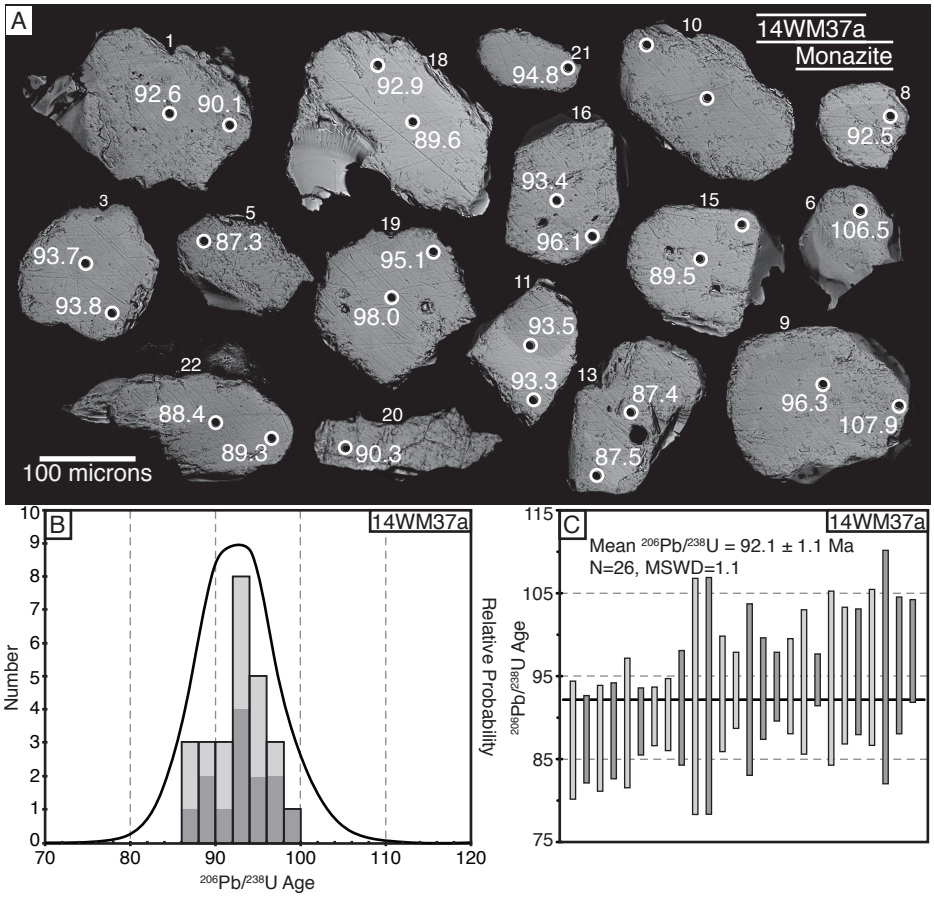
A
14WM37a
Monazite
1
92.6
90.1
18
92.9
89.6
21
94.8
10
8
92.5
16
93.4
96.1
3
93.7
93.8
5
87.3
19
95.1
98.0
15
89.5
6
106.5
11
93.5
93.3
9
96.3
107.9
22
88.4
89.3
20
90.3
13
87.4
87.5
100 microns
B
14WM37a
Number
Relative Probability
206Pb/238U Age
C
14WM37a
Mean 206Pb/238U = 92.1 ± 1.1 Ma
N=26, MSWD=1.1
206Pb/238U Age

Figure 16

Figure 16. (A) Back-scattered electron (BSE) images of represented monazite grains dated using the laser ablation – inductively coupled plasma – mass spectrometer (LA-ICP-MS) for sample 14WM37a (discordant leucosome in stromatic metatexite). Small numbers refer to grain number designations in Table 2. Larger numbers are 206Pb/238U ages in Ma for individual spot analyses (see Table 2 for corresponding error on spot analyses). (B) Probability density plot with stacked histogram of 206Pb/238U ages from monazite in sample 14WM37a. Light gray bars represent rim analyses and dark gray bars represent core analyses. (C) Weighted average age plot of monazite from sample 14WM37a; the weighted mean 206Pb/238U age calculation and uncertainty is given at 95% confidence limits. Light and dark gray bars represent rim and core analyses, respectively. Plots and calculations based on Isoplot of Ludwig (2012).

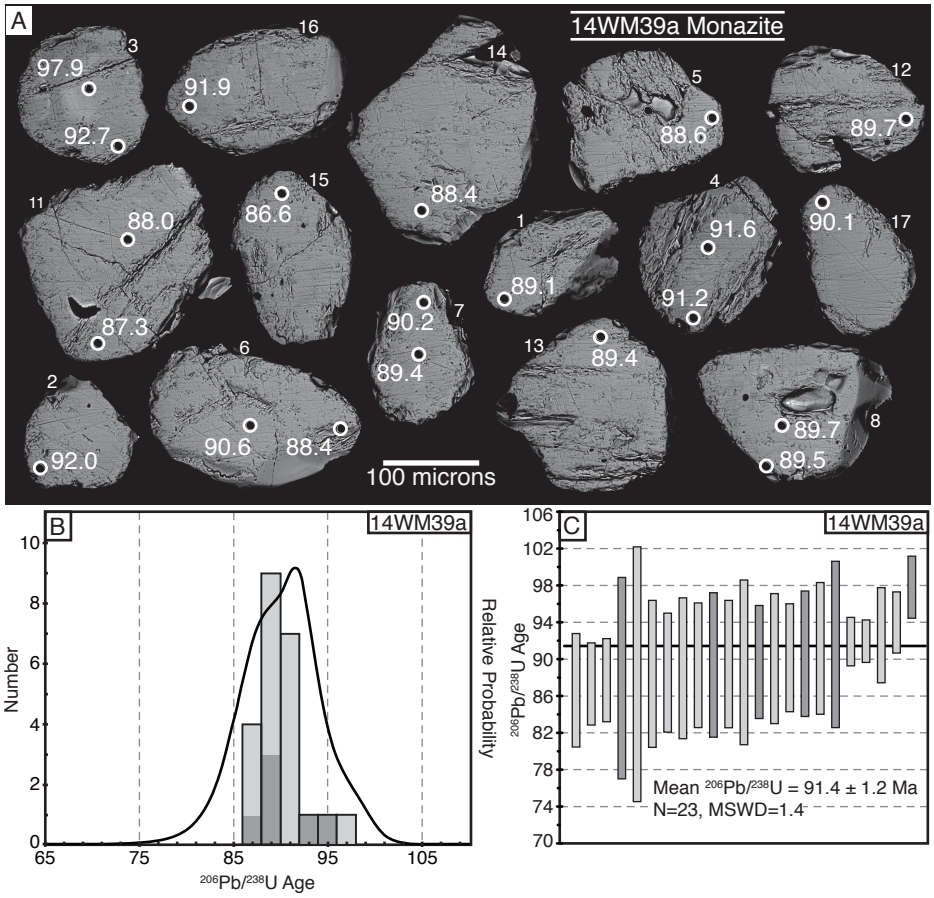
A
14WM39a Monazite
97.9
3
16
91.9
14
92.7
5
88.6
12
89.7
11
88.0
15
86.6
88.4
1
4
91.6
90.1
17
89.1
91.2
87.3
90.2
7
6
13
89.4
89.4
2
92.0
90.6
88.4
89.7
8
89.5
100 microns
B
14WM39a
Number
Relative Probability
206Pb/238U Age
C
14WM39a
206Pb/238U Age
Mean 206Pb/238U = 91.4 ± 1.2 Ma
N=23, MSWD=1.4

Figure 17

Figure 17. (A) Back-scattered electron (BSE) images of represented monazite grains dated using the laser ablation – inductively coupled plasma – mass spectrometer (LA-ICP-MS) for sample 14WM39a (boudinaged leucosome within melanocratic diatexite). Small numbers refer to grain number designations in Table 2. Larger numbers are 206Pb/238U ages in Ma for individual spot analyses (see Table 2 for corresponding error on spot analyses). (B) Probability density plot with stacked histogram of 206Pb/238U ages from monazite in sample 14WM39a. Light gray bars represent rim analyses and dark gray bars represent core analyses. (C) Weighted average age plot of monazite from sample 14WM39a; the weighted mean 206Pb/238U age calculation and uncertainty is given at 95% confidence limits. Light and dark gray bars represent rim and core analyses, respectively. Plots and calculations based on Isoplot of Ludwig (2012).

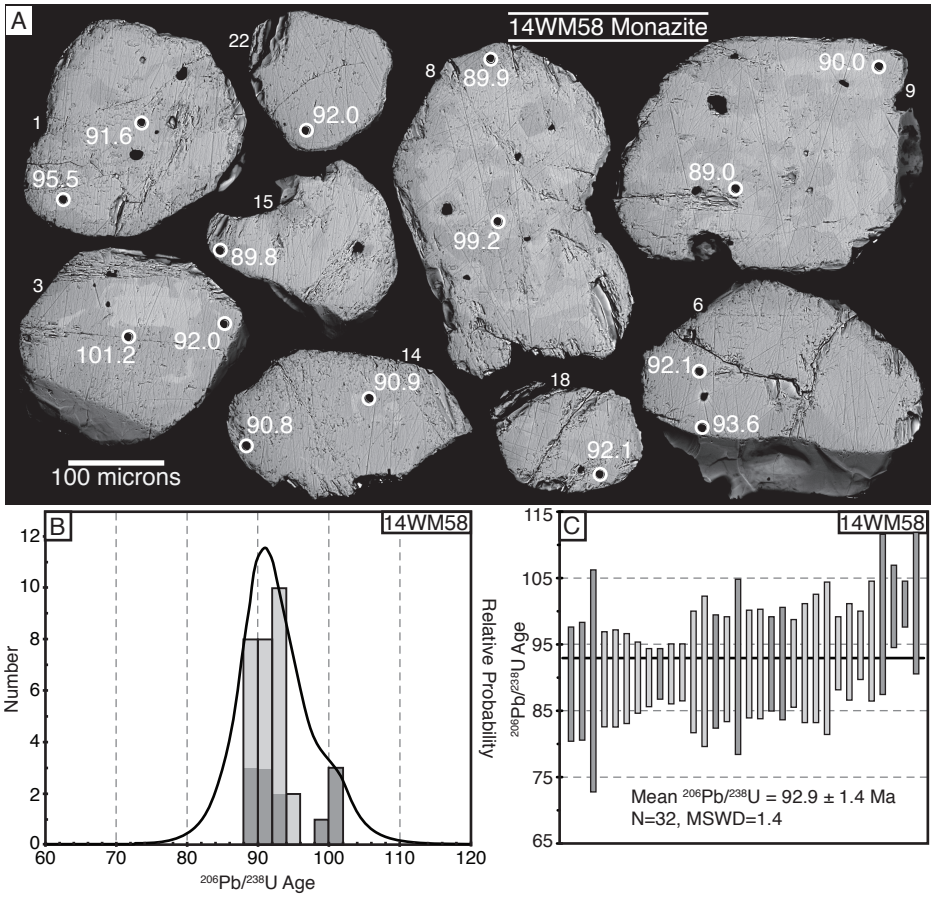
A
14WM58 Monazite
1
91.6
95.5
22
92.0
15
89.8
3
101.2
92.0
8
89.9
99.2
14
90.9
90.8
18
92.1
9
90.0
89.0
6
92.1
93.6
100 microns
B
14WM58
Number
Relative Probability
206Pb/238U Age
C
14WM58
206Pb/238U Age
Mean 206Pb/238U = 92.9 ± 1.4 Ma
N=32, MSWD=1.4

Figure 18

Figure 18. (A) Back-scattered electron (BSE) images of represented monazite grains dated using the laser ablation – inductively coupled plasma – mass spectrometer (LA-ICP-MS) for sample 14WM58 (nebulitic diatexite). Small numbers refer to grain number designations in Table 2. Larger numbers are 206Pb/238U ages in Ma for individual spot analyses (see Table 2 for corresponding error on spot analyses). (B) Probability density plot with stacked histogram of 206Pb/238U ages from monazite in sample 14WM58. Light gray bars represent rim analyses and dark gray bars represent core analyses. (C) Weighted average age plot of monazite from sample 14WM58; the weighted mean 206Pb/238U age calculation and uncertainty is given at 95% confidence limits. Light and dark gray bars represent rim and core analyses, respectively. Plots and calculations based on Isoplot of Ludwig (2012).

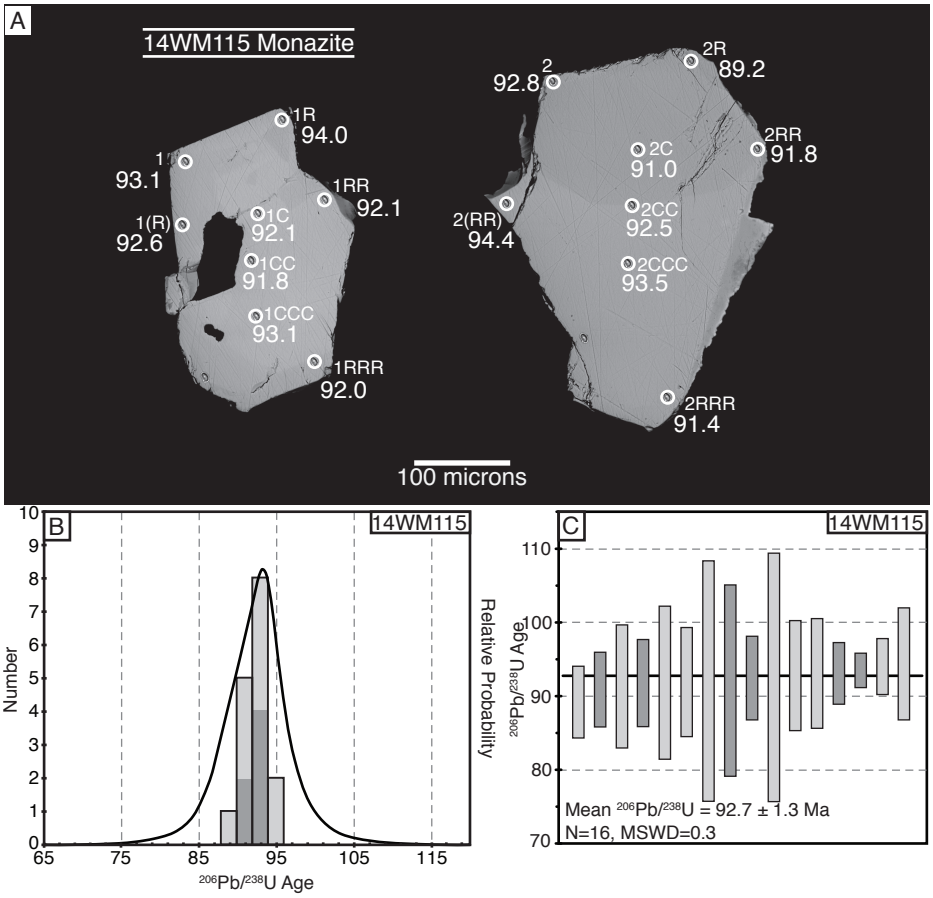
A
14WM115 Monazite
1
93.1
1R
94.0
1RR
92.1
1(R)
92.6
1C
92.1
1CC
91.8
1CCC
93.1
1RRR
92.0
2
92.8
2R
89.2
2RR
91.8
2C
91.0
2CC
92.5
2(RR)
94.4
2CCC
93.5
2RRR
91.4
100 microns
B
14WM115
Number
Relative Probability
206Pb/238U Age
C
14WM115
206Pb/238U Age
Mean 206Pb/238U = 92.7 ± 1.3 Ma
N=16, MSWD=0.3

Figure 19

Figure 19 (A) Back-scattered electron (BSE) images of represented monazite grains dated using the laser ablation – inductively coupled plasma – mass spectrometer (LA-ICP-MS) for sample 14WM115 (agmatic migmatite). Small numbers refer to spot number designations in Table 2. Larger numbers are 206Pb/238U ages in Ma for individual spot analyses (see Table 2 for corresponding error on spot analyses). (B) Probability density plot with stacked histogram of 206Pb/238U ages from monazite in sample 14WM115. Light gray bars represent rim analyses and dark gray bars represent core analyses. (C) Weighted average age plot of monazite from sample 14WM115; the weighted mean 206Pb/238U age calculation and uncertainty is given at 95% confidence limits. Light and dark gray bars represent rim and core analyses, respectively. Plots and calculations based on Isoplot of Ludwig (2012).

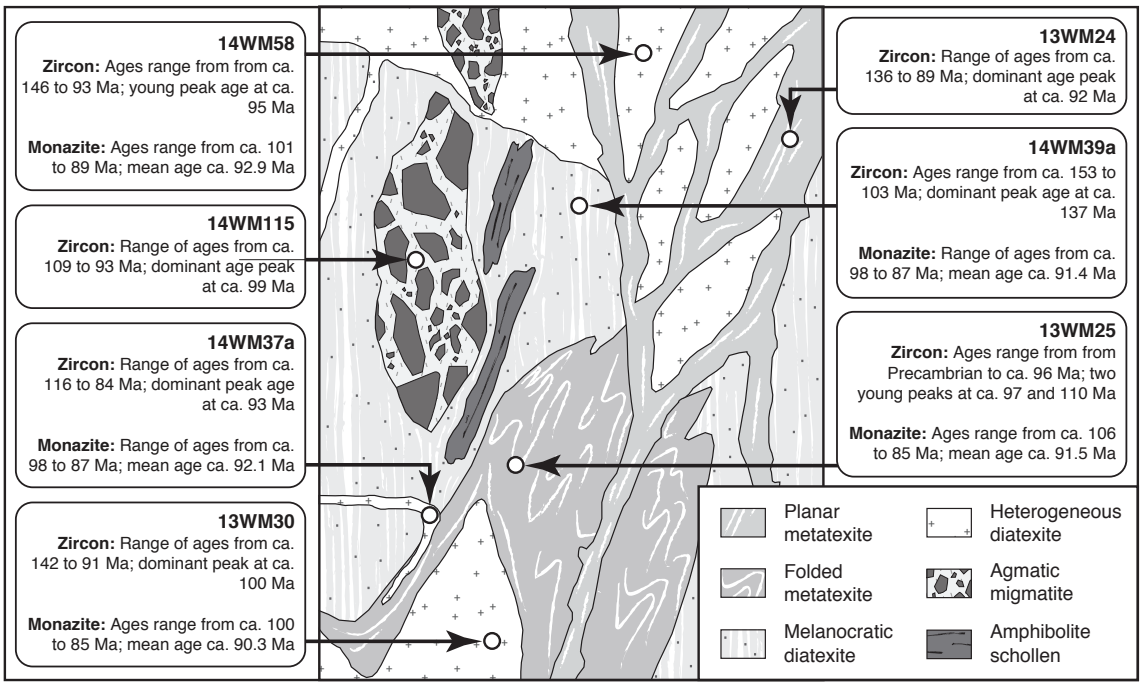
14WM58
Zircon: Ages range from from ca. 146 to 93 Ma; young peak age at ca. 95 Ma
Monazite: Ages range from ca. 101 to 89 Ma; mean age ca. 92.9 Ma
14WM115
Zircon: Range of ages from ca. 109 to 93 Ma; dominant age peak at ca. 99 Ma
14WM37a
Zircon: Range of ages from ca. 116 to 84 Ma; dominant peak age at ca. 93 Ma
Monazite: Range of ages from ca. 98 to 87 Ma; mean age ca. 92.1 Ma
13WM30
Zircon: Range of ages from ca. 142 to 91 Ma; dominant peak at ca. 100 Ma
Monazite: Ages range from ca. 100 to 85 Ma; mean age ca. 90.3 Ma
13WM24
Zircon: Range of ages from ca. 136 to 89 Ma; dominant age peak at ca. 92 Ma
14WM39a
Zircon: Ages range from ca. 153 to 103 Ma; dominant peak age at ca. 137 Ma
Monazite: Range of ages from ca. 98 to 87 Ma; mean age ca. 91.4 Ma
13WM25
Zircon: Ages range from from Precambrian to ca. 96 Ma; two young peaks at ca. 97 and 110 Ma
Monazite: Ages range from ca. 106 to 85 Ma; mean age ca. 91.5 Ma
Planar metatexite
Folded metatexite
Melanocratic diatexite
Heterogeneous diatexite
Agmatic migmatite
Amphibolite schollen

Figure 20

Figure 20. Schematic drawing synthesizing leucosome relationships of sampled migmatite units in the PPMD and summary of acquired LA-ICP-MS zircon and monazite ages. Figure combines structural relationships observed over the entire PPMD.

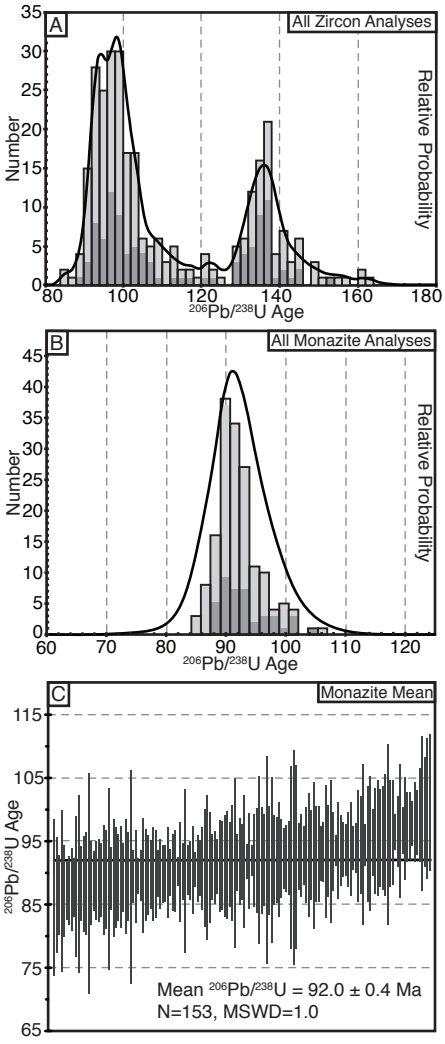
A
All Zircon Analyses
Number
Relative Probability
206Pb/238U Age
B
All Monazite Analyses
Number
Relative Probability
206Pb/238U Age
C
Monazite Mean
206Pb/238U Age
Mean 206Pb/238U = 92.0 ± 0.4 Ma
N=153, MSWD=1.0

Figure 21

Figure 21. (A) Probability density plot with stacked histogram of 206Pb/238U ages from all zircon analyses from the seven sampled migmatite units. Note the two dominant populations of ages (ca. 145-128 Ma and ca. 104-90 Ma). (B) Probability density plot with stacked histogram of 206Pb/238U ages from all monazite analyses, and (C) weighted mean 206Pb/238U age calculated from all monazite analyses. Weighted mean 206Pb/238U age calculation and uncertainty is given at 95% confidence limits. Light and dark gray bars represent rim and core analyses, respectively.

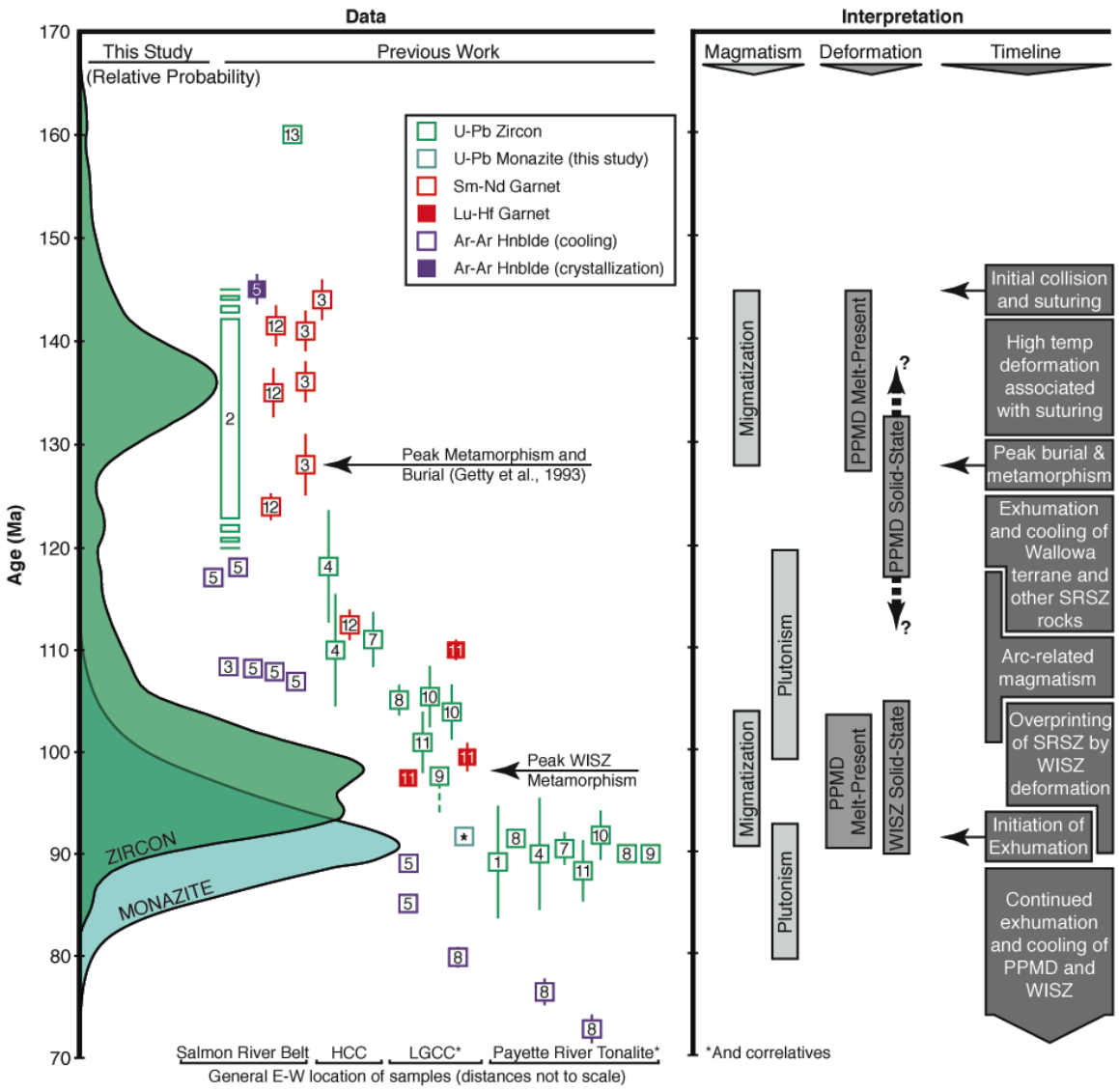
Data
Interpretation
This Study
Previous Work
(Relative Probability)
Magmatism
Deformation
Timeline
U-Pb Zircon
U-Pb Monazite (this study)
Sm-Nd Garnet
Lu-Hf Garnet
Ar-Ar Hnblde (cooling)
Ar-Ar Hnblde (crystallization)
Age (Ma)
Peak Metamorphism and Burial (Getty et al., 1993)
Peak WISZ Metamorphism
ZIRCON
MONAZITE
Migmatization
Plutonism
PPMD Melt-Present
PPMD Solid-State
WISZ Solid-State
Initial collision and suturing
High temp deformation associated with suturing
Peak burial & metamorphism
Exhumation and cooling of Wallowa terrane and other SRSZ rocks
Arc-related magmatism
Overprinting of SRSZ by WISZ deformation
Initiation of Exhumation
Continued exhumation and cooling of PPMD and WISZ
Salmon River Belt
HCC
LGCC*
Payette River Tonalite*
General E-W location of samples (distances not to scale)
*And correlatives

Figure 22

Figure 22. Summary of 206Pb/238U ages of zircon and monazite samples from this study, and visualization of geochronologic data collected from other work in the western Idaho shear zone and Salmon River suture zone. Interpretations made from geochronologic data in this figure as well as structural data presented in this paper. Further discussion of these interpretations is included in the text. References for data are as follows: 1) Lund and Snee, 1988; 2) Walker 1989; 3) Getty et al., 1993; 4) Manduca et al., 1993; 5) Snee et al, 1995; 6) Snee et al., 2005; 7) McClelland and Oldow, 2007; 8) Giorgis et al., 2008; 9) Benford et al., 2010; 10) Grey et al., 2012; 11) Braudy et al., in review; 12) Mckay, 2011; 13) LaMaskin et al., 2015.

TABLE 1. Summary of LA-ICP-MS U-Pb zircon results for migmatitic rocks in the Potters Pond migmatite domain

Spot Number	U (ppm)	Th (ppm)	U/Th	Isotope Ratios $^{206}Pb^*/^{207}Pb^*$	±1σ (%)	$^{207}Pb^*/^{235}U$	±1σ (%)	$^{206}Pb^*/^{238}U$	±1σ (%)	Ages (in Ma) $^{206}Pb^*/^{207}Pb^*$	±1σ (Ma)	$^{207}Pb/^{235}U$	±1σ (Ma)	$^{206}Pb/^{238}U$	±1σ (Ma)
Sample 13WM24 - *Leucosome in stromatic metatexite (N44.42670°, W116.12759°)*															
Rims															
1	332	71	4.693	20.8175	2.1	0.0936	2.7	0.0141	1.7	101.1	49.2	90.9	2.3	90.5	1.5
2	363	56	6.442	20.5004	2.3	0.0984	2.7	0.0146	1.4	137.3	53.0	95.3	2.4	93.6	1.3
4	131	23	5.696	20.3499	4.8	0.1037	5.3	0.0153	2.0	154.5	113.6	100.1	5.0	97.9	2.0
6	384	70	5.488	20.5344	2.8	0.1024	3.3	0.0153	1.7	133.4	64.8	99.0	3.1	97.6	1.7
7	546	98	5.569	20.1985	2.4	0.1003	2.8	0.0147	1.4	172.0	56.1	97.1	2.6	94.0	1.3
9	344	60	5.783	20.3463	2.5	0.0994	2.9	0.0147	1.4	155.0	58.5	96.3	2.6	93.9	1.3
10	411	87	4.718	20.3310	2.3	0.0953	2.6	0.0140	1.2	156.7	53.2	92.4	2.3	89.9	1.1
12	588	101	5.827	20.5788	2.3	0.1051	2.9	0.0157	1.7	128.3	55.1	101.5	2.8	100.4	1.7
13	1117	997	1.120	20.1775	1.4	0.1136	2.0	0.0166	1.4	174.4	33.5	109.2	2.1	106.3	1.5
15	255	61	4.205	20.3146	3.4	0.1171	4.1	0.0172	2.2	158.6	80.5	112.4	4.3	110.2	2.4
17	387	81	4.758	20.7476	2.8	0.0954	3.0	0.0144	1.1	109.0	65.1	92.5	2.6	91.9	1.0
18	178	42	4.269	20.7328	3.8	0.0927	4.3	0.0139	2.0	110.7	89.2	90.0	3.7	89.2	1.8
19	1144	122	9.353	20.6433	1.7	0.0957	2.3	0.0143	1.5	120.9	40.8	92.8	2.0	91.7	1.3
21	370	60	6.212	20.8373	2.5	0.0951	3.2	0.0144	2.0	98.8	59.4	92.3	2.8	92.0	1.8
22	493	123	4.003	20.1115	2.8	0.0970	3.3	0.0142	1.8	182.0	65.1	94.0	3.0	90.6	1.6
23	448	52	8.593	20.6992	2.7	0.0952	3.2	0.0143	1.7	114.5	63.3	92.3	2.8	91.4	1.5
25	903	59	15.315	20.5637	1.4	0.1025	2.2	0.0153	1.7	130.0	31.9	99.1	2.1	97.8	1.7
27	644	6	115.509	20.1157	2.3	0.1118	2.6	0.0163	1.3	181.5	53.0	107.6	2.7	104.3	1.4
29	429	80	5.358	20.2168	2.6	0.1010	3.1	0.0148	1.5	169.9	61.5	97.7	2.8	94.8	1.5
31	1112	195	5.703	20.4107	1.9	0.1073	2.7	0.0159	2.0	147.5	44.0	103.5	2.7	101.6	2.0
33	335	61	5.479	20.2296	3.2	0.0985	3.6	0.0145	1.6	168.4	75.1	95.4	3.3	92.5	1.5
35	921	68	13.468	21.1999	1.8	0.1040	2.2	0.0160	1.3	57.8	41.8	100.4	2.1	102.2	1.3
37	652	85	7.660	21.0249	2.4	0.1002	2.9	0.0153	1.7	77.5	56.5	96.9	2.7	97.7	1.6
38	594	159	3.727	20.7297	1.7	0.0986	2.4	0.0148	1.6	111.0	40.4	95.5	2.2	94.8	1.5
40	306	54	5.717	20.1376	2.7	0.0973	3.1	0.0142	1.6	179.0	63.3	94.3	2.8	90.9	1.4
41	402	83	4.855	21.2238	2.6	0.0941	3.0	0.0145	1.3	55.1	62.8	91.4	2.6	92.7	1.2
43	689	96	7.146	20.8199	2.1	0.0957	2.5	0.0145	1.5	100.8	49.0	92.8	2.3	92.5	1.4
45	301	56	5.396	20.2598	3.7	0.0962	4.1	0.0141	1.7	164.9	87.2	93.3	3.7	90.5	1.5
47	747	63	11.849	20.9128	1.9	0.1035	2.3	0.0157	1.3	90.3	45.8	100.0	2.2	100.4	1.3
49	352	91	3.865	20.6761	2.9	0.0953	3.3	0.0143	1.5	117.1	69.4	92.4	2.9	91.4	1.3
Cores															
3	719	194	3.705	20.4099	1.9	0.1035	2.5	0.0153	1.6	147.6	43.5	100.0	2.4	98.0	1.6
5	600	84	7.175	20.1370	1.5	0.1460	4.6	0.0213	4.3	179.1	35.8	138.4	5.9	136.0	5.8
8	223	98	2.271	21.1496	3.5	0.0985	4.0	0.0151	1.8	63.5	84.3	95.4	3.6	96.7	1.7
11	614	409	1.504	18.8314	1.4	0.3908	3.3	0.0534	3.0	333.2	31.0	334.9	9.4	335.2	9.7
14	550	192	2.859	18.2226	1.6	0.2455	3.0	0.0324	2.5	407.2	36.4	222.9	6.0	205.8	5.2
16	485	96	5.044	20.4767	2.4	0.1023	2.8	0.0152	1.4	140.0	56.9	98.9	2.7	97.2	1.4
20	180	51	3.499	19.7241	3.7	0.1094	4.1	0.0156	1.7	227.2	86.5	105.4	4.1	100.1	1.7
24	470	29	16.206	20.2812	1.9	0.1237	2.4	0.0182	1.5	162.5	43.3	118.4	2.7	116.2	1.7
26	107	60	1.782	21.1277	4.8	0.1046	5.3	0.0160	2.2	66.0	114.4	101.0	5.1	102.5	2.2

TABLE 1. Summary of LA-ICP-MS U-Pb zircon results for migmatitic rocks in the Potters Pond migmatite domain — Continued

Spot Number	U (ppm)	Th (ppm)	U/Th	Isotope Ratios $^{206}Pb^*/^{207}Pb^*$	±1σ (%)	$^{207}Pb^*/^{235}U$	±1σ (%)	$^{206}Pb^*/^{238}U$	±1σ (%)	Ages (in Ma) $^{206}Pb^*/^{207}Pb^*$	±1σ (Ma)	$^{207}Pb/^{235}U$	±1σ (Ma)	$^{206}Pb/^{238}U$	±1σ (Ma)
28	148	60	2.451	8.8386	0.9	4.5613	1.5	0.2924	1.1	1850.4	16.4	1742.2	12.1	1653.5	16.6
30	1063	84	12.651	20.9562	1.6	0.1105	2.4	0.0168	1.8	85.4	38.6	106.4	2.5	107.4	1.9
32	161	53	3.035	20.4248	3.9	0.0994	4.3	0.0147	1.7	145.9	91.8	96.2	3.9	94.2	1.6
34	478	95	5.029	20.8112	2.1	0.1000	2.6	0.0151	1.6	101.8	49.9	96.8	2.4	96.6	1.5
36	1284	718	1.790	16.4813	4.7	0.1574	5.1	0.0188	2.0	627.7	100.6	148.4	7.0	120.1	2.4
39	179	61	2.942	20.5517	3.5	0.1023	3.9	0.0152	1.7	131.4	81.6	98.9	3.6	97.5	1.7
42	268	86	3.125	19.4876	2.6	0.1370	3.0	0.0194	1.6	255.0	59.2	130.4	3.7	123.7	1.9
44	3466	242	14.327	20.8969	1.2	0.1108	1.6	0.0168	1.2	92.1	27.4	106.7	1.7	107.4	1.2
46	255	74	3.465	20.5154	3.2	0.0976	3.4	0.0145	1.2	135.5	75.1	94.6	3.1	93.0	1.1
48	608	509	1.194	20.1710	1.9	0.1234	3.1	0.0180	2.4	175.1	44.6	118.1	3.4	115.3	2.7
50	447	113	3.976	20.8211	2.2	0.0991	2.7	0.0150	1.5	100.6	52.8	96.0	2.5	95.8	1.5
Sample 13WM25 - *Schlierin-textured granodiorite diatexite (N44.41028°, W116.13582°)*															
Rims															
1	183	45	4.047	13.6156	1.1	1.5534	1.9	0.1534	1.6	1026.2	23.1	951.9	12.0	1026.2	23.1
3	902	19	47.808	19.2857	1.2	0.1676	2.1	0.0234	1.7	278.9	27.7	157.4	3.1	149.4	2.5
5	382	18	21.730	11.7109	1.8	0.4521	2.9	0.0384	2.3	1324.4	34.9	378.7	9.2	242.9	5.5
6	550	13	43.520	21.2309	2.1	0.0973	3.0	0.0150	2.2	54.4	50.0	94.2	2.7	95.8	2.1
8	159	22	7.208	13.3555	1.4	1.5887	2.3	0.1539	1.8	1065.2	27.9	965.8	14.1	1065.2	27.9
10	636	13	49.420	18.6155	2.3	0.1878	3.8	0.0254	3.0	359.2	51.3	174.8	6.0	161.4	4.8
11	618	3	206.432	20.6863	1.7	0.1305	2.2	0.0196	1.3	116.0	40.4	124.5	2.5	125.0	1.6
13	420	11	36.636	20.2711	2.1	0.1275	2.6	0.0187	1.6	163.6	48.0	121.9	3.0	119.7	1.9
15	519	7	72.434	18.4262	3.9	0.1518	4.2	0.0203	1.4	382.3	88.2	143.5	5.6	129.4	1.9
17	308	11	27.720	20.5628	2.7	0.1136	3.3	0.0169	1.9	130.1	64.1	109.3	3.4	108.3	2.1
20	583	8	76.050	14.8761	2.0	0.2336	2.5	0.0252	1.5	844.6	41.4	213.2	4.8	160.5	2.4
22	612	4	160.260	20.5769	1.7	0.1279	2.2	0.0191	1.4	128.5	39.7	122.2	2.5	121.9	1.7
23	619	6	98.613	20.5003	1.4	0.1006	1.8	0.0150	1.2	137.3	33.0	97.3	1.7	95.7	1.1
27	1026	8	128.494	20.8095	1.4	0.1628	1.8	0.0246	1.2	102.0	32.6	153.1	2.6	156.4	1.8
28	538	12	43.130	21.0157	1.5	0.1206	1.9	0.0184	1.1	78.6	36.1	115.7	2.0	117.5	1.3
30	443	7	60.640	20.5999	1.6	0.1147	2.5	0.0171	2.0	125.8	37.8	110.3	2.6	109.6	2.1
31	470	60	7.884	15.0639	1.6	0.4985	2.3	0.0545	1.6	818.5	33.2	410.7	7.6	341.9	5.3
34	443	7	64.383	19.6498	2.4	0.1440	2.8	0.0205	1.6	235.9	54.4	136.6	3.6	131.0	2.1
36	281	24	11.794	14.2448	1.4	0.5933	2.1	0.0613	1.5	934.2	29.6	473.0	8.0	383.5	5.7
38	586	17	34.860	20.2495	1.4	0.1176	1.9	0.0173	1.2	166.1	33.4	112.9	2.0	110.4	1.3
45	663	22	30.479	19.2380	1.0	0.2404	1.9	0.0335	1.6	284.6	22.8	218.8	3.7	212.7	3.4
46	34	24	1.433	11.5899	1.5	2.5650	1.9	0.2156	1.2	1344.5	28.4	1290.7	13.7	1344.5	28.4
47	253	33	7.711	16.5271	2.4	0.2133	2.7	0.0256	1.3	621.7	51.2	196.3	4.9	162.7	2.2
Cores															
2	27	7	4.014	13.5179	2.3	1.6524	2.6	0.1620	1.1	1040.8	47.1	990.5	16.2	967.9	9.7
4	161	35	4.588	13.4871	1.2	1.7328	1.8	0.1695	1.3	1045.4	24.4	1020.8	11.3	1009.4	11.8
7	19	5	3.876	10.5374	2.1	3.1022	2.6	0.2371	1.5	1526.1	39.4	1433.2	19.9	1371.5	19.0
9	66	30	2.194	11.3310	1.2	2.7532	2.0	0.2263	1.5	1388.0	23.3	1343.0	14.6	1314.9	18.3

TABLE 1. Summary of LA-ICP-MS U-Pb zircon results for migmatitic rocks in the Potters Pond migmatite domain — Continued

Spot Number	U (ppm)	Th (ppm)	U/Th	Isotope Ratios $^{206}Pb^*/^{207}Pb^*$	±1σ (%)	$^{207}Pb^*/^{235}U$	±1σ (%)	$^{206}Pb^*/^{238}U$	±1σ (%)	Ages (in Ma) $^{206}Pb^*/^{207}Pb^*$	±1σ (Ma)	$^{207}Pb/^{235}U$	±1σ (Ma)	$^{206}Pb/^{238}U$	±1σ (Ma)
12	240	76	3.147	13.2813	1.1	1.8163	1.6	0.1749	1.1	1076.4	22.2	1051.3	10.3	1039.3	10.7
16	82	42	1.954	5.4252	1.4	10.2943	2.2	0.4051	1.6	2692.2	23.9	2461.6	20.3	2192.3	30.6
21	168	88	1.907	6.1979	1.0	8.7970	1.7	0.3954	1.4	2469.8	17.5	2317.2	15.7	2148.0	25.1
24	148	15	9.622	20.3602	3.8	0.1057	4.2	0.0156	1.7	153.3	90.0	102.1	4.1	99.9	1.7
26	89	78	1.139	10.9260	1.1	3.0387	1.8	0.2408	1.4	1457.5	21.8	1417.4	13.6	1390.8	17.0
29	507	40	12.791	15.0501	5.7	0.3566	10.9	0.0389	9.3	820.4	118.4	309.7	29.0	246.1	22.4
35	53	43	1.220	7.8689	1.2	5.9219	1.9	0.3380	1.4	2058.0	21.7	1964.5	16.3	1876.9	23.1
37	71	56	1.279	12.7629	1.1	2.0968	1.8	0.1941	1.4	1155.8	22.3	1147.7	12.4	1143.5	14.9
44	33	33	0.996	8.9323	1.1	4.7869	2.1	0.3101	1.7	1831.3	20.3	1782.6	17.4	1741.3	26.6
Sample 13WM30 - *Schlierin-textured granodiorite diatexite (N44.40779°, W116.13957°)*															
Rims															
1	967	183	5.277	20.8979	2.0	0.1171	2.8	0.0177	1.9	91.9	47.9	112.4	3.0	113.4	2.2
2	329	55	5.942	20.9528	2.8	0.0981	3.2	0.0149	1.6	85.7	66.5	95.1	2.9	95.4	1.5
4	252	100	2.526	20.5093	3.1	0.1062	3.3	0.0158	1.2	136.2	73.0	102.5	3.2	101.1	1.2
5	1939	257	7.541	20.7587	1.4	0.1169	2.2	0.0176	1.7	107.8	33.8	112.2	2.3	112.5	1.9
7	597	69	8.611	20.0614	2.1	0.1009	2.7	0.0147	1.6	187.8	49.6	97.6	2.5	94.0	1.5
10	2019	28	73.291	20.6864	1.6	0.1013	2.3	0.0152	1.6	116.0	37.5	98.0	2.1	97.2	1.5
11	125	20	6.391	20.7499	3.9	0.1069	4.2	0.0161	1.5	108.7	92.9	103.1	4.1	102.9	1.6
13	1085	72	14.989	20.9337	1.5	0.1033	2.0	0.0157	1.4	87.9	34.6	99.8	1.9	100.3	1.4
15	1685	147	11.440	20.6985	1.8	0.1077	2.5	0.0162	1.7	114.6	43.6	103.9	2.4	103.4	1.7
17	1516	69	22.084	20.6202	1.3	0.0988	1.9	0.0148	1.4	123.5	29.9	95.6	1.7	94.5	1.3
18	1355	32	41.857	20.5926	1.6	0.0990	2.1	0.0148	1.4	126.7	37.7	95.8	1.9	94.6	1.3
20	597	72	8.264	20.6561	2.3	0.1029	2.8	0.0154	1.6	119.5	53.3	99.5	2.6	98.6	1.6
22	745	63	11.899	20.9893	1.5	0.0995	2.1	0.0152	1.6	81.6	34.8	96.3	2.0	96.9	1.5
24	447	62	7.262	20.3191	2.3	0.1052	3.0	0.0155	1.8	158.1	53.9	101.5	2.9	99.1	1.8
25	1391	32	43.402	20.2948	1.3	0.1094	2.0	0.0161	1.5	160.9	31.2	105.4	2.0	102.9	1.5
27	436	79	5.553	20.1325	2.3	0.1054	3.0	0.0154	2.0	179.6	53.4	101.7	2.9	98.4	1.9
29	705	66	10.615	21.0215	1.9	0.0942	2.4	0.0144	1.4	77.9	45.8	91.4	2.1	92.0	1.3
30	2492	158	15.795	20.3789	1.3	0.1027	2.1	0.0152	1.6	151.2	30.6	99.3	2.0	97.1	1.5
32	1256	50	24.983	20.6871	1.3	0.1027	1.9	0.0154	1.5	115.9	30.0	99.3	1.8	98.6	1.4
33	3126	158	19.833	20.4348	1.2	0.1442	1.9	0.0214	1.5	144.8	28.4	136.8	2.5	136.3	2.0
34	1195	67	17.921	21.1751	1.6	0.0963	2.0	0.0148	1.2	60.7	38.8	93.3	1.8	94.6	1.2
36	1502	62	24.249	20.4939	1.3	0.1084	2.6	0.0161	2.3	138.0	30.6	104.5	2.6	103.0	2.3
38	1291	64	20.232	20.8290	1.2	0.1060	1.9	0.0160	1.4	99.7	29.3	102.3	1.8	102.4	1.4
39	951	13	76.027	20.3372	1.6	0.1150	2.3	0.0170	1.6	156.0	37.7	110.5	2.4	108.4	1.7
41	1196	98	12.168	20.4396	1.9	0.1197	2.8	0.0177	2.0	144.2	45.4	114.8	3.0	113.4	2.2
42	836	106	7.900	20.4724	2.0	0.1125	2.7	0.0167	1.8	140.4	47.9	108.2	2.8	106.8	1.9
43	1095	185	5.913	20.6233	1.3	0.1151	2.1	0.0172	1.6	123.2	31.6	110.7	2.2	110.1	1.8
45	1324	56	23.727	20.8906	1.8	0.1036	2.4	0.0157	1.7	92.8	41.7	100.1	2.3	100.4	1.7
47	606	115	5.283	21.1510	2.7	0.1063	3.6	0.0163	2.4	63.3	64.5	102.6	3.6	104.3	2.5
48	858	55	15.563	20.1894	2.0	0.1009	2.7	0.0148	1.8	173.0	46.0	97.6	2.5	94.5	1.7

TABLE 1. Summary of LA-ICP-MS U-Pb zircon results for migmatitic rocks in the Potters Pond migmatite domain — Continued

Spot Number	U (ppm)	Th (ppm)	U/Th	Isotope Ratios $^{206}Pb^*/^{207}Pb^*$	±1σ (%)	$^{207}Pb^*/^{235}U$	±1σ (%)	$^{206}Pb^*/^{238}U$	±1σ (%)	Ages (in Ma) $^{206}Pb^*/^{207}Pb^*$	±1σ (Ma)	$^{207}Pb/^{235}U$	±1σ (Ma)	$^{206}Pb/^{238}U$	±1σ (Ma)
50	1729	41	42.315	20.5806	1.2	0.0953	1.8	0.0142	1.3	128.1	28.0	92.4	1.6	91.1	1.2
Cores															
3	616	312	1.975	18.1142	2.6	0.2051	3.3	0.0269	1.9	420.5	58.7	189.4	5.6	171.4	3.3
6	181	98	1.846	21.1831	3.0	0.1027	3.2	0.0158	1.3	59.8	71.1	99.2	3.1	100.9	1.3
8	93	90	1.025	20.9492	4.4	0.1166	4.7	0.0177	1.7	86.2	103.2	112.0	4.9	113.2	1.9
9	116	74	1.567	20.9621	5.4	0.1066	5.6	0.0162	1.7	84.7	127.6	102.9	5.5	103.7	1.8
12	686	244	2.817	19.4213	1.5	0.2911	2.4	0.0410	1.8	262.8	35.0	259.4	5.4	259.1	4.6
14	144	45	3.194	20.0892	3.8	0.1096	4.0	0.0160	1.5	184.6	87.9	105.6	4.1	102.2	1.5
16	184	173	1.065	20.7396	2.9	0.1034	3.2	0.0156	1.4	109.9	67.4	99.9	3.0	99.5	1.4
19	161	55	2.949	19.9567	2.6	0.1141	3.2	0.0165	1.9	200.0	59.5	109.7	3.3	105.6	1.9
21	512	242	2.115	19.5898	1.6	0.2912	2.3	0.0414	1.7	242.9	36.1	259.5	5.3	261.3	4.4
23	128	78	1.637	19.6404	5.0	0.1010	5.5	0.0144	2.3	237.0	115.3	97.7	5.1	92.1	2.1
26	100	58	1.710	22.1076	5.9	0.0962	6.2	0.0154	1.7	43.1	144.4	93.2	5.5	98.6	1.7
28	62	35	1.766	20.4271	7.0	0.1024	7.4	0.0152	2.3	145.7	164.4	99.0	6.9	97.1	2.2
31	148	53	2.775	18.4886	5.4	0.1244	5.7	0.0167	1.8	374.7	122.7	119.1	6.5	106.7	1.9
35	151	50	3.021	19.5386	3.7	0.1488	4.2	0.0211	2.0	248.9	85.0	140.9	5.6	134.6	2.7
37	60	41	1.466	23.4634	6.6	0.0962	7.0	0.0164	2.3	189.8	166.3	93.3	6.3	104.7	2.4
40	31	17	1.792	23.9115	7.6	0.0896	8.0	0.0155	2.5	237.3	192.2	87.1	6.7	99.3	2.5
46	1301	108	12.086	20.3409	1.7	0.1511	4.4	0.0223	4.0	155.6	39.6	142.9	5.8	142.1	5.7
49	89	69	1.288	21.0867	5.8	0.1039	6.1	0.0159	2.1	70.6	137.1	100.4	5.9	101.7	2.1
Sample 14WM37a - *Discordant leucosome in stromatic metatexite (N44.41924°, W116.13478°)*															
Rims															
1	1466	456	3.213	21.1259	1.5	0.0963	2.1	0.0148	1.5	66.2	35.0	93.4	1.9	94.4	1.4
3	1394	336	4.147	20.9681	2.0	0.0974	2.5	0.0148	1.6	84.0	47.5	94.4	2.3	94.8	1.5
5	515	234	2.200	20.7039	2.7	0.1038	3.2	0.0156	1.7	114.0	64.9	100.3	3.1	99.7	1.7
7	792	163	4.856	21.0627	2.1	0.0961	3.0	0.0147	2.2	73.3	50.9	93.2	2.7	94.0	2.0
9	426	80	5.333	20.6177	3.1	0.1081	4.1	0.0162	2.7	123.8	73.0	104.2	4.1	103.4	2.8
11	2254	109	20.630	21.0414	1.6	0.0952	2.3	0.0145	1.7	75.7	37.5	92.3	2.0	93.0	1.6
12	2157	406	5.312	20.7584	1.3	0.0874	2.0	0.0132	1.5	107.8	31.4	85.1	1.6	84.3	1.3
13	3063	456	6.715	21.1271	1.2	0.0870	1.9	0.0133	1.5	66.1	29.2	84.7	1.6	85.4	1.3
15	1553	381	4.076	20.7741	1.8	0.0966	2.3	0.0145	1.5	106.0	41.7	93.6	2.1	93.1	1.4
17	2864	62	46.381	19.9130	1.3	0.1111	1.8	0.0160	1.2	205.1	29.5	107.0	1.8	102.6	1.3
18	514	123	4.169	20.8712	2.4	0.0994	3.0	0.0150	1.8	95.0	57.4	96.2	2.8	96.2	1.7
20	302	96	3.136	20.5178	2.4	0.1220	3.0	0.0181	1.8	135.2	56.4	116.9	3.3	116.0	2.1
22	1203	81	14.779	20.6911	1.8	0.0963	2.5	0.0144	1.7	115.5	43.5	93.3	2.2	92.5	1.6
24	10162	139	73.356	21.0023	1.0	0.0962	1.4	0.0147	0.9	80.1	22.9	93.2	1.2	93.8	0.9
26	2242	449	4.996	20.8036	1.2	0.0948	1.7	0.0143	1.2	102.6	27.7	92.0	1.5	91.6	1.1
28	2269	107	21.175	21.0993	1.1	0.0967	1.6	0.0148	1.3	69.2	25.5	93.8	1.5	94.7	1.2
30	2764	539	5.126	21.0386	1.3	0.0945	2.1	0.0144	1.6	76.0	30.5	91.7	1.8	92.3	1.5
32	461	177	2.603	21.4799	2.9	0.0920	3.4	0.0143	1.8	26.5	70.7	89.3	2.9	91.7	1.6
34	1385	120	11.580	21.0613	1.3	0.1040	2.0	0.0159	1.5	73.4	30.0	100.5	1.9	101.6	1.6

TABLE 1. Summary of LA-ICP-MS U-Pb zircon results for migmatitic rocks in the Potters Pond migmatite domain — Continued

Spot Number	U (ppm)	Th (ppm)	U/Th	Isotope Ratios $^{206}Pb^*/^{207}Pb^*$	±1σ (%)	$^{207}Pb^*/^{235}U$	±1σ (%)	$^{206}Pb^*/^{238}U$	±1σ (%)	Ages (in Ma) $^{206}Pb^*/^{207}Pb^*$	±1σ (Ma)	$^{207}Pb/^{235}U$	±1σ (Ma)	$^{206}Pb/^{238}U$	±1σ (Ma)
35	1123	305	3.684	21.0839	1.8	0.1059	2.1	0.0162	1.2	70.9	42.5	102.2	2.1	103.6	1.2
37	2659	121	22.054	20.5830	1.1	0.0914	1.9	0.0136	1.5	127.8	26.3	88.8	1.6	87.3	1.3
38	895	352	2.545	21.0705	1.8	0.0900	2.4	0.0137	1.6	72.4	41.9	87.5	2.0	88.0	1.4
39	1173	55	21.402	20.5813	1.6	0.1044	2.1	0.0156	1.4	128.0	37.0	100.8	2.0	99.7	1.4
41	1786	115	15.590	20.9885	1.3	0.1000	1.8	0.0152	1.3	81.7	30.8	96.7	1.7	97.4	1.2
43	1411	401	3.520	21.0823	2.0	0.0956	2.5	0.0146	1.4	71.1	48.1	92.7	2.2	93.6	1.3
45	374	161	2.320	20.8950	3.5	0.1015	3.8	0.0154	1.5	92.3	82.0	98.2	3.5	98.4	1.5
46	3252	96	33.759	20.9787	1.2	0.0998	1.7	0.0152	1.2	82.8	27.7	96.6	1.5	97.1	1.1
47	1729	337	5.132	20.9871	1.4	0.1029	2.2	0.0157	1.7	81.8	33.3	99.5	2.1	100.2	1.7
48	2079	456	4.558	21.0021	1.6	0.0957	2.2	0.0146	1.6	80.1	37.8	92.8	2.0	93.3	1.5
49	392	42	9.275	21.1675	2.8	0.1032	3.3	0.0158	1.6	61.5	66.9	99.7	3.1	101.4	1.6
Cores															
2	1645	760	2.166	20.7708	1.4	0.0943	2.0	0.0142	1.4	106.4	33.5	91.5	1.8	91.0	1.3
4	515	214	2.412	20.5992	2.2	0.0972	2.4	0.0145	1.1	125.9	50.8	94.2	2.2	92.9	1.0
6	583	411	1.420	21.2599	2.1	0.1052	2.5	0.0162	1.2	51.1	51.0	101.6	2.4	103.8	1.3
8	1328	952	1.395	20.4422	1.8	0.1007	2.3	0.0149	1.6	143.9	41.1	97.4	2.2	95.5	1.5
10	376	32	11.904	21.0792	2.5	0.1016	2.8	0.0155	1.3	71.4	59.8	98.3	2.6	99.4	1.3
14	774	211	3.675	21.5067	2.4	0.0887	2.7	0.0138	1.3	23.5	57.2	86.3	2.3	88.6	1.2
16	475	278	1.708	21.1588	2.6	0.0994	3.1	0.0153	1.7	62.5	62.5	96.2	2.9	97.6	1.7
19	1057	643	1.642	20.9553	1.5	0.1086	1.8	0.0165	1.1	85.5	35.5	104.7	1.8	105.5	1.1
21	128	54	2.390	20.3539	5.2	0.1055	5.7	0.0156	2.4	154.0	121.1	101.8	5.5	99.6	2.3
23	1401	414	3.381	20.7501	2.0	0.1011	2.5	0.0152	1.5	108.7	46.7	97.7	2.3	97.3	1.5
25	5614	104	53.937	20.3439	1.2	0.0958	1.9	0.0141	1.4	155.2	27.4	92.9	1.6	90.5	1.3
27	1481	311	4.769	20.6417	1.7	0.0959	2.2	0.0144	1.4	121.1	39.6	93.0	1.9	91.9	1.3
29	3982	111	35.762	20.1466	1.5	0.1029	1.9	0.0150	1.2	178.0	34.7	99.5	1.8	96.2	1.1
31	1249	255	4.894	20.8324	1.8	0.0956	2.2	0.0144	1.2	99.4	42.8	92.7	1.9	92.5	1.1
33	786	226	3.476	20.9840	1.6	0.0965	2.3	0.0147	1.7	82.2	38.1	93.5	2.1	94.0	1.6
36	2677	1043	2.566	20.5635	1.4	0.1024	1.7	0.0153	1.0	130.0	32.4	99.0	1.6	97.7	1.0
40	144	72	2.006	20.5413	4.3	0.1046	4.7	0.0156	1.8	132.5	101.2	101.0	4.5	99.7	1.8
42	1321	123	10.735	20.9521	1.6	0.1051	2.3	0.0160	1.6	85.8	38.3	101.4	2.2	102.1	1.6
44	719	209	3.436	20.8005	1.9	0.0963	2.4	0.0145	1.3	103.0	45.6	93.4	2.1	93.0	1.2
50	645	127	5.090	21.0725	1.8	0.1067	2.2	0.0163	1.3	72.2	42.8	103.0	2.2	104.3	1.3
Sample 14WM39a - *Boudinaged leucosome within melanocratic diatexite (N44.41895°, W116.13708°)*															
Rims															
51	4107	719	5.714	20.2902	1.1	0.1617	1.9	0.0238	1.5	161.4	25.0	152.2	2.7	151.6	2.3
53	1747	96	18.241	20.1304	1.2	0.1594	2.0	0.0233	1.5	179.8	29.1	150.2	2.8	148.3	2.3
55	6167	471	13.107	18.2564	2.6	0.1667	3.1	0.0221	1.7	403.0	58.1	156.6	4.5	140.8	2.4
56	3686	433	8.521	13.5784	7.2	0.2110	7.6	0.0208	2.4	1031.8	145.3	194.4	13.4	132.6	3.2
57	1038	18	56.689	20.7325	1.9	0.1072	2.5	0.0161	1.6	110.8	45.4	103.4	2.4	103.1	1.6
59	2520	15	165.407	20.2018	1.2	0.1445	2.0	0.0212	1.6	171.6	28.5	137.1	2.6	135.1	2.1
61	1372	278	4.935	20.6475	1.8	0.1421	2.1	0.0213	1.2	120.4	41.6	134.9	2.7	135.8	1.6

TABLE 1. Summary of LA-ICP-MS U-Pb zircon results for migmatitic rocks in the Potters Pond migmatite domain — Continued

Spot Number	U (ppm)	Th (ppm)	U/Th	Isotope Ratios $^{206}Pb^*/^{207}Pb^*$	±1σ (%)	$^{207}Pb^*/^{235}U$	±1σ (%)	$^{206}Pb^*/^{238}U$	±1σ (%)	Ages (in Ma) $^{206}Pb^*/^{207}Pb^*$	±1σ (Ma)	$^{207}Pb/^{235}U$	±1σ (Ma)	$^{206}Pb/^{238}U$	±1σ (Ma)
62	2151	260	8.274	19.8552	1.5	0.1522	2.3	0.0219	1.8	211.8	35.0	143.8	3.1	139.7	2.5
64	1018	15	69.841	20.1894	2.7	0.1302	3.4	0.0191	1.9	173.0	64.1	124.3	3.9	121.8	2.3
66	3688	319	11.546	20.0168	1.0	0.1486	1.8	0.0216	1.5	193.1	23.4	140.7	2.4	137.6	2.1
68	6271	1254	4.999	20.3440	0.9	0.1439	2.6	0.0212	2.4	155.2	21.1	136.5	3.3	135.5	3.2
69	2358	48	49.273	18.3624	1.5	0.1610	2.4	0.0214	1.8	390.1	34.6	151.6	3.4	136.8	2.5
71	6235	1453	4.292	20.3656	0.9	0.1487	2.5	0.0220	2.3	152.7	20.7	140.8	3.2	140.1	3.2
73	192	161	1.188	20.4113	2.9	0.1461	3.2	0.0216	1.4	147.5	67.8	138.5	4.2	138.0	1.9
75	4181	765	5.462	20.3284	0.9	0.1461	2.0	0.0215	1.8	157.0	21.4	138.5	2.6	137.4	2.5
76	1754	82	21.357	20.3240	1.6	0.1429	2.3	0.0211	1.7	157.5	36.7	135.6	2.9	134.4	2.2
77	4020	110	36.592	20.3032	1.2	0.1439	1.8	0.0212	1.4	159.9	27.2	136.5	2.3	135.2	1.9
78	867	23	37.428	21.0000	2.2	0.1155	2.7	0.0176	1.6	80.4	51.2	110.9	2.8	112.4	1.8
79	5621	1211	4.642	20.4603	1.1	0.1456	2.4	0.0216	2.1	141.8	26.0	138.1	3.1	137.8	2.9
81	2187	19	114.764	20.5869	1.1	0.1517	1.9	0.0226	1.5	127.4	26.8	143.4	2.5	144.4	2.1
83	7062	1748	4.040	20.4311	1.2	0.1439	3.5	0.0213	3.3	145.2	28.5	136.5	4.5	136.0	4.4
85	1941	63	30.634	20.4487	1.7	0.1470	2.5	0.0218	1.8	143.2	40.3	139.3	3.3	139.0	2.5
87	1288	29	44.405	20.4823	1.6	0.1415	2.5	0.0210	1.9	139.3	37.0	134.4	3.1	134.1	2.5
89	5201	922	5.640	20.6573	1.3	0.1395	2.0	0.0209	1.5	119.3	30.7	132.6	2.5	133.3	2.0
90	6601	1389	4.754	20.3495	1.2	0.1409	3.5	0.0208	3.3	154.6	28.3	133.9	4.4	132.7	4.3
92	4832	907	5.327	20.2135	1.1	0.1507	2.1	0.0221	1.8	170.2	26.4	142.5	2.8	140.9	2.5
94	990	188	5.253	20.6877	1.7	0.1467	2.5	0.0220	1.8	115.9	40.2	139.0	3.2	140.4	2.5
96	1333	344	3.876	20.7251	1.5	0.1523	2.5	0.0229	1.9	111.6	36.6	143.9	3.3	145.9	2.8
97	3407	588	5.793	20.7650	1.3	0.1544	1.9	0.0233	1.4	107.1	30.3	145.8	2.6	148.2	2.0
98	4525	682	6.630	16.4873	2.5	0.1838	3.3	0.0220	2.1	626.9	53.9	171.3	5.1	140.1	2.9
99	2617	852	3.072	20.5886	1.2	0.1526	1.9	0.0228	1.5	127.2	27.1	144.2	2.5	145.2	2.2
100	1966	246	7.989	20.8252	1.4	0.1508	2.3	0.0228	1.8	100.2	33.6	142.6	3.0	145.1	2.5
Cores															
52	205	121	1.692	20.5747	3.3	0.1435	3.6	0.0214	1.6	128.8	76.8	136.1	4.6	136.5	2.1
54	1021	230	4.429	20.7317	1.4	0.1594	2.5	0.0240	2.0	110.8	34.1	150.2	3.4	152.7	3.0
58	382	249	1.536	20.1330	2.3	0.1456	2.6	0.0213	1.4	179.5	52.6	138.0	3.4	135.6	1.8
60	3604	106	33.874	19.9086	1.2	0.1467	1.8	0.0212	1.3	205.6	28.3	139.0	2.3	135.1	1.7
63	110	45	2.427	19.9912	5.4	0.1483	5.7	0.0215	1.7	196.0	125.0	140.4	7.4	137.2	2.4
65	254	116	2.180	20.6067	2.5	0.1401	2.9	0.0209	1.3	125.1	59.6	133.1	3.6	133.6	1.8
67	3978	244	16.316	20.4569	1.6	0.1438	2.4	0.0213	1.7	142.2	38.2	136.4	3.0	136.1	2.3
70	659	110	6.019	20.3036	2.1	0.1511	3.1	0.0222	2.3	159.9	49.3	142.9	4.2	141.9	3.2
72	225	160	1.413	20.5717	3.5	0.1436	4.1	0.0214	2.2	129.1	82.9	136.3	5.3	136.7	2.9
74	396	426	0.929	21.0612	2.1	0.1406	2.9	0.0215	2.0	73.4	50.2	133.6	3.6	137.0	2.7
80	291	294	0.992	20.2838	2.7	0.1418	3.2	0.0209	1.6	162.1	64.0	134.6	4.0	133.0	2.1
82	170	96	1.774	20.5688	3.3	0.1422	3.6	0.0212	1.5	129.4	77.9	135.0	4.6	135.3	2.0
84	2056	722	2.845	20.4322	1.6	0.1486	2.1	0.0220	1.4	145.0	37.7	140.7	2.8	140.4	1.9
86	292	295	0.989	20.6911	2.9	0.1400	3.4	0.0210	1.9	115.5	67.7	133.0	4.3	134.0	2.5
88	114	47	2.404	21.2013	4.1	0.1397	4.6	0.0215	2.0	57.7	98.6	132.8	5.7	137.0	2.6
91	253	231	1.093	18.9238	4.0	0.1573	4.6	0.0216	2.2	322.1	90.7	148.4	6.3	137.7	3.0

TABLE 1. Summary of LA-ICP-MS U-Pb zircon results for migmatitic rocks in the Potters Pond migmatite domain — Continued

Spot Number	U (ppm)	Th (ppm)	U/Th	Isotope Ratios $^{206}Pb^*/^{207}Pb^*$	±1σ (%)	$^{207}Pb^*/^{235}U$	±1σ (%)	$^{206}Pb^*/^{238}U$	±1σ (%)	Ages (in Ma) $^{206}Pb^*/^{207}Pb^*$	±1σ (Ma)	$^{207}Pb/^{235}U$	±1σ (Ma)	$^{206}Pb/^{238}U$	±1σ (Ma)
95	985	169	5.815	20.8780	1.9	0.1429	2.8	0.0216	2.0	94.2	45.9	135.6	3.5	138.0	2.7
Sample 14WM58 - *Nebulitic diatexite (N44.42994°, W116.13438°)*															
Rims															
51	576	33	17.220	20.1695	2.3	0.1024	2.6	0.0150	1.2	175.3	54.2	99.0	2.5	95.8	1.2
53	590	29	20.011	20.4502	1.9	0.0989	2.4	0.0147	1.4	143.0	45.7	95.8	2.2	93.9	1.3
54	527	48	11.065	20.3090	1.4	0.1302	1.9	0.0192	1.3	159.2	33.6	124.3	2.2	122.5	1.5
57	3130	29	106.322	19.9595	0.9	0.1413	1.6	0.0204	1.4	199.7	21.0	134.2	2.0	130.5	1.7
59	2576	155	16.670	20.5126	1.2	0.1631	1.8	0.0243	1.3	135.8	28.1	153.4	2.5	154.5	2.0
61	468	39	12.122	20.5163	1.8	0.1018	2.3	0.0151	1.4	135.4	41.8	98.4	2.1	96.9	1.3
63	1951	9	221.933	20.5899	1.1	0.1397	1.7	0.0209	1.3	127.0	25.7	132.8	2.1	133.1	1.7
65	437	23	19.182	20.9360	2.6	0.1004	2.9	0.0152	1.4	87.6	60.6	97.1	2.7	97.5	1.3
67	608	31	19.381	20.4937	2.4	0.0992	2.9	0.0147	1.5	138.0	57.1	96.0	2.6	94.3	1.4
68	563	33	16.906	20.2262	1.6	0.1522	2.2	0.0223	1.6	168.8	37.1	143.9	3.0	142.4	2.2
69	359	69	5.192	20.2264	1.7	0.1427	2.3	0.0209	1.6	168.7	40.1	135.5	3.0	133.6	2.1
71	1458	38	38.786	13.3089	2.6	0.1669	2.9	0.0161	1.3	1072.2	52.0	156.8	4.2	103.0	1.3
73	716	59	12.201	20.4741	1.6	0.1454	2.1	0.0216	1.4	140.3	37.3	137.8	2.7	137.7	1.9
74	718	81	8.819	20.2765	1.7	0.1524	2.1	0.0224	1.3	163.0	39.1	144.0	2.9	142.8	1.9
76	446	21	20.852	20.9644	2.0	0.0951	2.5	0.0145	1.5	84.4	47.5	92.3	2.2	92.6	1.4
78	266	59	4.512	19.9106	2.3	0.1443	2.8	0.0208	1.6	205.4	52.7	136.8	3.5	132.9	2.0
80	173	43	4.064	19.9994	2.9	0.1479	3.3	0.0215	1.5	195.1	67.0	140.0	4.3	136.8	2.0
82	752	54	14.058	20.4612	1.9	0.1435	2.5	0.0213	1.7	141.7	43.5	136.2	3.2	135.8	2.3
84	198	28	7.059	20.5819	3.9	0.0979	4.4	0.0146	2.1	127.9	91.1	94.8	4.0	93.5	2.0
86	365	50	7.284	20.3346	2.4	0.1294	2.9	0.0191	1.5	156.3	57.1	123.6	3.3	121.9	1.8
87	544	29	18.752	20.6666	2.1	0.1016	2.6	0.0152	1.5	118.2	49.9	98.2	2.4	97.4	1.5
89	932	86	10.816	20.4865	1.5	0.1407	2.2	0.0209	1.7	138.8	34.2	133.7	2.8	133.4	2.2
90	719	55	13.007	20.0207	1.7	0.1490	2.2	0.0216	1.3	192.6	39.5	141.0	2.9	138.0	1.8
92	2141	7	302.200	20.4574	1.1	0.1469	1.7	0.0218	1.3	142.2	25.4	139.2	2.2	139.0	1.8
94	852	18	47.797	20.0808	1.7	0.1092	2.4	0.0159	1.8	185.6	38.5	105.2	2.4	101.7	1.8
95	1800	35	51.843	20.4429	1.5	0.0993	2.3	0.0147	1.7	143.8	34.3	96.1	2.1	94.2	1.6
96	1736	128	13.580	19.3182	1.9	0.1432	2.5	0.0201	1.6	275.0	44.2	135.9	3.2	128.1	2.0
98	644	42	15.264	20.7581	1.6	0.1071	2.2	0.0161	1.4	107.8	38.8	103.4	2.1	103.2	1.5
100	786	33	24.062	20.5220	1.7	0.1139	2.3	0.0169	1.4	134.8	40.8	109.5	2.3	108.3	1.5
Cores															
52	574	47	12.215	20.1988	1.7	0.1384	2.5	0.0203	1.8	171.9	38.9	131.6	3.1	129.4	2.4
55	273	26	10.370	20.5132	1.9	0.1377	2.3	0.0205	1.3	135.8	43.9	131.0	2.8	130.7	1.7
58	525	48	10.987	20.1182	2.1	0.1477	2.4	0.0215	1.1	181.3	48.8	139.8	3.1	137.4	1.5
60	561	69	8.102	20.6341	1.8	0.1461	2.1	0.0219	1.1	121.9	42.9	138.5	2.7	139.4	1.5
62	637	68	9.422	20.4405	1.6	0.1414	2.4	0.0210	1.8	144.1	37.4	134.3	3.0	133.7	2.3
64	853	62	13.777	20.4002	1.7	0.1159	5.5	0.0171	5.3	148.7	39.0	111.4	5.8	109.6	5.7
66	764	92	8.289	20.3680	1.9	0.1427	2.5	0.0211	1.6	152.5	44.1	135.4	3.2	134.5	2.2
70	130	34	3.827	21.2557	3.1	0.1353	3.5	0.0209	1.7	51.6	73.3	128.8	4.2	133.1	2.2

TABLE 1. Summary of LA-ICP-MS U-Pb zircon results for migmatitic rocks in the Potters Pond migmatite domain — Continued

Spot Number	U (ppm)	Th (ppm)	U/Th	Isotope Ratios $^{206}Pb^*/^{207}Pb^*$	±1σ (%)	$^{207}Pb^*/^{235}U$	±1σ (%)	$^{206}Pb^*/^{238}U$	±1σ (%)	Ages (in Ma) $^{206}Pb^*/^{207}Pb^*$	±1σ (Ma)	$^{207}Pb/^{235}U$	±1σ (Ma)	$^{206}Pb/^{238}U$	±1σ (Ma)
72	366	32	11.408	20.0169	2.5	0.1420	3.2	0.0206	1.9	193.0	58.3	134.8	4.0	131.5	2.5
75	951	133	7.173	20.6713	1.5	0.1517	2.0	0.0227	1.4	117.7	34.7	143.4	2.7	145.0	2.0
77	167	30	5.493	20.0333	3.4	0.1401	3.9	0.0204	1.8	191.1	79.7	133.2	4.9	129.9	2.4
79	206	48	4.298	20.2253	3.0	0.1404	3.4	0.0206	1.6	168.9	69.6	133.4	4.2	131.4	2.1
81	219	43	5.098	20.4821	2.7	0.1353	3.2	0.0201	1.7	139.4	62.2	128.8	3.8	128.3	2.2
83	494	36	13.769	20.3308	2.1	0.1430	2.7	0.0211	1.7	156.7	49.2	135.7	3.4	134.5	2.2
85	375	39	9.738	20.5197	2.2	0.1450	2.7	0.0216	1.5	135.0	52.0	137.5	3.5	137.6	2.1
88	1172	50	23.324	20.1778	2.5	0.1563	4.8	0.0229	4.1	174.4	57.5	147.5	6.6	145.8	5.9
91	278	70	3.986	20.2367	2.3	0.1404	2.6	0.0206	1.2	167.6	53.1	133.4	3.2	131.5	1.5
93	625	81	7.700	20.5070	1.6	0.1423	2.3	0.0212	1.6	136.5	38.2	135.1	2.9	135.0	2.2
97	402	37	10.878	19.4595	2.4	0.1478	2.8	0.0209	1.4	258.3	54.8	140.0	3.6	133.1	1.8
99	1512	67	22.571	20.2249	1.1	0.1469	1.6	0.0215	1.2	168.9	25.6	139.2	2.1	137.4	1.6
Sample 14WM115 - *Agmatic diatexite (44.43280°, W116.14230°)*															
Rims															
51	141	142	0.993	20.6436	4.2	0.1038	4.7	0.0155	2.0	120.9	99.7	100.3	4.5	99.5	2.0
53	178	48	3.713	20.9709	3.2	0.0968	3.5	0.0147	1.3	83.7	76.5	93.8	3.1	94.2	1.2
55	96	23	4.207	20.5555	3.8	0.1062	4.2	0.0158	1.8	130.9	90.5	102.5	4.1	101.3	1.8
56	82	10	7.926	19.7872	4.9	0.1098	5.1	0.0158	1.4	219.8	114.4	105.8	5.2	100.8	1.4
57	258	423	0.610	20.2518	2.6	0.1072	3.0	0.0157	1.4	165.8	61.8	103.4	2.9	100.7	1.4
58	124	31	4.034	20.1327	3.9	0.1064	4.1	0.0155	1.4	179.6	90.8	102.7	4.0	99.4	1.4
60	405	27	14.834	21.1671	2.0	0.1002	2.6	0.0154	1.7	61.6	47.8	96.9	2.4	98.4	1.7
62	796	312	2.549	20.8517	1.8	0.0983	2.3	0.0149	1.4	97.2	42.5	95.2	2.1	95.1	1.3
64	64	20	3.274	20.1691	5.3	0.1048	5.5	0.0153	1.5	175.4	123.0	101.2	5.3	98.1	1.4
65	210	33	6.363	21.0517	3.6	0.0991	3.9	0.0151	1.5	74.5	84.8	95.9	3.5	96.8	1.4
66	130	90	1.449	20.9776	3.6	0.1023	4.0	0.0156	1.8	82.9	85.9	98.9	3.8	99.5	1.7
67	88	59	1.494	20.7506	4.8	0.1013	5.2	0.0152	2.0	108.7	112.7	97.9	4.8	97.5	1.9
68	2131	189	11.297	20.6326	1.2	0.1039	2.0	0.0155	1.6	122.1	27.9	100.4	1.9	99.4	1.6
70	94	19	4.816	20.5817	3.7	0.1012	4.2	0.0151	2.0	128.0	87.3	97.9	3.9	96.7	1.9
71	124	20	6.119	20.3550	3.4	0.1022	3.8	0.0151	1.7	154.0	80.8	98.8	3.6	96.5	1.6
72	413	255	1.618	21.1405	1.5	0.1112	2.3	0.0170	1.7	64.5	34.6	107.1	2.3	109.0	1.9
73	86	57	1.497	21.7663	5.5	0.0972	5.8	0.0153	1.8	5.4	132.9	94.2	5.2	98.2	1.8
74	696	65	10.663	21.1737	1.5	0.1012	2.4	0.0155	1.9	60.8	34.7	97.9	2.2	99.4	1.9
75	685	68	10.007	21.0781	2.0	0.1013	2.2	0.0155	1.0	71.6	46.9	97.9	2.1	99.0	1.0
77	608	655	0.929	20.9546	1.6	0.1017	2.1	0.0155	1.3	85.5	38.9	98.4	2.0	98.9	1.3
79	921	78	11.886	20.9676	1.2	0.1014	1.6	0.0154	1.1	84.0	29.3	98.1	1.5	98.6	1.1
81	492	45	10.956	20.7809	1.6	0.0969	2.5	0.0146	1.9	105.2	38.8	93.9	2.3	93.5	1.8
82	147	15	10.052	21.6379	3.8	0.0990	4.1	0.0155	1.7	8.9	90.3	95.8	3.8	99.4	1.7
83	126	5	24.583	20.6561	4.7	0.0980	5.0	0.0147	1.6	119.5	111.6	95.0	4.5	94.0	1.5
84	2305	310	7.443	21.0705	1.4	0.0980	1.9	0.0150	1.3	72.4	32.2	94.9	1.7	95.8	1.3
86	495	526	0.941	20.5528	2.2	0.1029	2.6	0.0153	1.4	131.2	52.7	99.4	2.5	98.1	1.3
87	92	24	3.866	20.7888	3.8	0.1019	4.2	0.0154	1.8	104.4	89.7	98.5	3.9	98.3	1.7

TABLE 1. Summary of LA-ICP-MS U-Pb zircon results for migmatitic rocks in the Potters Pond migmatite domain — Continued

Spot Number	U (ppm)	Th (ppm)	U/Th	Isotope Ratios $^{206}Pb^*/^{207}Pb^*$	±1σ (%)	$^{207}Pb^*/^{235}U$	±1σ (%)	$^{206}Pb^*/^{238}U$	±1σ (%)	Ages (in Ma) $^{206}Pb^*/^{207}Pb^*$	±1σ (Ma)	$^{207}Pb/^{235}U$	±1σ (Ma)	$^{206}Pb/^{238}U$	±1σ (Ma)
88	70	6	10.867	21.4221	5.1	0.0982	5.4	0.0153	1.9	32.9	121.4	95.1	4.9	97.6	1.8
Cores															
52	307	426	0.721	20.7972	2.7	0.1037	3.0	0.0156	1.3	103.4	64.2	100.1	2.9	100.0	1.3
54	108	79	1.368	20.8668	4.0	0.1017	4.4	0.0154	1.8	95.5	94.1	98.4	4.1	98.5	1.7
59	54	7	7.556	20.8657	4.7	0.1011	5.0	0.0153	1.6	95.6	111.8	97.8	4.6	97.9	1.6
61	81	6	13.386	20.1027	5.6	0.1026	5.8	0.0150	1.7	183.1	129.5	99.2	5.5	95.7	1.6
63	395	196	2.019	21.0516	2.5	0.0968	3.0	0.0148	1.7	74.6	59.9	93.8	2.7	94.5	1.6
69	498	557	0.895	20.7286	2.1	0.1037	2.6	0.0156	1.6	111.2	48.9	100.2	2.5	99.7	1.6
76	2273	83	27.464	20.0581	1.3	0.0996	1.7	0.0145	1.2	188.2	29.1	96.4	1.6	92.7	1.1
78	531	322	1.649	20.8968	1.9	0.0969	2.4	0.0147	1.6	92.1	44.7	93.9	2.2	94.0	1.5
80	160	137	1.168	20.6011	3.3	0.1016	3.8	0.0152	1.8	125.7	78.8	98.3	3.6	97.1	1.7
85	1574	520	3.027	20.9441	1.4	0.0968	2.0	0.0147	1.4	86.7	32.5	93.8	1.8	94.1	1.3

Analyses with >10% uncertainty (1-sigma) in 206Pb/238U age are not included.
Analyses with >10% uncertainty (1-sigma) in 207Pb/235U age are not included, unless 206Pb/238U age is <400Ma.
Concordance is based on 206Pb/238U age / 206Pb/207Pb age. Value is not reported for 206Pb/238U ages <400 Ma because of large uncertainty in 206Pb/207Pb age.
Analyses with 206Pb/238U age >400 Ma and with >20% discordance (<80% concordance) are not included.
Analyses with 206Pb/238U age >400 Ma and with >5% reverse discordance (<105% concordance) are not included.
All uncertainties are reported at the 1-sigma level, and include only measurement errors.
Systematic errors are as follows (at 2-sigma level): [sample 13WM24: 1.4% (206Pb/238U) & 1.0% (206Pb/207Pb); sample 13WM25: 1.2% (206Pb/238U) & 1.0% (206Pb/207Pb); sample 13WM30: 1.2% (206Pb/238U) & 1.0% (206Pb/207Pb); sample 14WM37a: 1.4% (206Pb/238U) & 0.9% (206Pb/207Pb); sample 14WM39a: 1.4% (206Pb/238U) & 0.9% (206Pb/207Pb); sample 14WM58: 1.4% (206Pb/238U) & 1.0% (206Pb/207Pb); sample 14WM115: 1.2% (206Pb/238U) & 1.0% (206Pb/207Pb)].
Analyses conducted by LA-ICPMS, as described by Gehrels et al. (2008) and Gehrels and Pecha (2014).
U concentration and U/Th are calibrated relative to FC-1 zircon standard and are accurate to ~20%
Common Pb correction is from measured 204Pb with common Pb composition interpreted from Stacey and Kramers (1975).
Common Pb composition assigned uncertainties of 1.5 for 206Pb/204Pb, 0.3 for 207Pb/204Pb, and 2.0 for 208Pb/204Pb.
U/Pb and 206Pb/207Pb fractionation is calibrated relative to fragments of large Sri Lanka zircons and individual crystals of FC-1, and R33.
U decay constants and composition as follows: 238U = 9.8485 x 10-10, 235U = 1.55125 x 10-10, 238U/235U = 137.88.
Weighted mean determined with Isoplot 3.75 (Ludwig, 2012).

TABLE 2. Summary of LA-ICP-MS U-Pb monazite results for migmatitic rocks in the Potters Pond migmatite domain

Grain Number	U (ppm)	Th (ppm)	U/Th	Isotope Ratios $^{206}Pb^*/^{207}Pb^*$	±1σ (%)	$^{208}Pb^*/^{232}Th$	±1σ (%)	$^{207}Pb^*/^{235}U$	±1σ (%)	$^{206}Pb^*/^{238}U$	±1σ (%)	Ages (in Ma) $^{206}Pb^*/^{207}Pb^*$	±1σ (%)	$^{208}Pb^*/^{232}Th$	±1σ (%)	$^{207}Pb^*/^{235}U$	±1σ (%)	$^{206}Pb^*/^{238}U$	±1σ (%)
Sample 13WM24 - *Leucosome in stromatic metatexite (N44.42670°, W116.12759°)*																			
Rims																			
6	1990	39740	0.050	20.4581	1.1	0.0047	3.7	0.1044	2.0	0.0155	1.7	142.1	25.6	94.9	3.5	100.8	1.9	99.1	1.7
12	5717	122548	0.047	20.6069	0.8	0.0043	2.8	0.0944	3.6	0.0141	3.5	125.0	19.8	87.4	2.4	91.6	3.2	90.3	3.1
13	2291	51217	0.045	20.3638	0.8	0.0046	6.6	0.1028	4.2	0.0152	4.1	152.9	19.6	93.3	6.1	99.3	4.0	97.1	4.0
17	2329	19059	0.122	20.3160	0.8	0.0050	2.5	0.1068	3.2	0.0157	3.1	158.4	19.1	100.9	2.5	103.0	3.1	100.7	3.1
21	2145	61770	0.035	20.4551	1.6	0.0046	5.5	0.1019	5.7	0.0151	5.4	142.4	36.9	92.8	5.1	98.5	5.3	96.7	5.2
Cores																			
13	2344	51521	0.045	20.3701	1.7	0.0046	3.8	0.1021	3.3	0.0151	2.9	152.2	39.5	92.6	3.5	98.7	3.1	96.5	2.7
17	1547	18216	0.085	20.4142	1.5	0.0051	3.3	0.1105	5.5	0.0164	5.3	147.2	34.6	102.8	3.4	106.4	5.5	104.6	5.5
21	2077	60596	0.034	20.5781	1.8	0.0046	3.1	0.1020	3.3	0.0152	2.8	128.4	42.0	93.4	2.9	98.6	3.1	97.3	2.7
Sample 13WM25 - *Schlieren-textured granodiorite diatexite (N44.41028°, W116.13582°)*																			
Rims																			
1	804	48962	0.016	21.0770	0.9	0.0044	4.0	0.0908	3.8	0.0139	3.6	71.7	22.2	89.2	3.6	88.3	3.2	88.9	3.2
2	3928	40165	0.098	20.8783	0.7	0.0046	2.0	0.0957	3.6	0.0145	3.5	94.2	17.0	91.8	1.8	92.8	3.2	92.8	3.2
3	457	29918	0.015	22.3912	2.9	0.0047	2.5	0.0929	3.2	0.0151	1.4	-74.1	70.1	94.3	2.4	90.2	2.8	96.5	1.4
4	1524	40137	0.038	20.2930	1.6	0.0049	1.8	0.1126	2.6	0.0166	2.1	161.1	37.4	99.6	1.8	108.3	2.7	105.9	2.2
5	2352	41415	0.057	20.4092	1.0	0.0046	10.3	0.0971	7.2	0.0144	7.2	147.7	22.7	92.7	9.5	94.1	6.5	92.0	6.6
7	1384	40994	0.034	19.4456	2.3	0.0044	3.0	0.1099	4.4	0.0155	3.7	259.9	53.3	88.1	2.6	105.8	4.4	99.1	3.7
8	783	47604	0.016	20.5861	1.5	0.0044	3.4	0.1013	2.4	0.0151	1.9	127.5	34.2	88.7	3.1	98.0	2.2	96.8	1.8
9	846	37006	0.023	20.2435	1.6	0.0046	2.4	0.0922	5.4	0.0135	5.2	166.8	36.6	93.1	2.2	89.5	4.7	86.6	4.5
10	999	35792	0.028	20.7860	1.6	0.0045	1.5	0.0948	4.0	0.0143	3.6	104.6	37.5	91.5	1.4	92.0	3.5	91.5	3.3
12	508	55486	0.009	21.4836	1.8	0.0045	2.9	0.0900	3.5	0.0140	3.0	26.0	42.3	89.8	2.6	87.5	2.9	89.8	2.6
13	869	28192	0.031	20.3239	1.7	0.0044	3.7	0.0942	3.9	0.0139	3.5	157.5	39.8	89.6	3.3	91.4	3.4	88.9	3.1
14	1456	36127	0.040	20.5164	1.1	0.0046	3.5	0.0952	1.9	0.0142	1.5	135.4	26.5	92.1	3.2	92.3	1.6	90.7	1.3
15	919	40383	0.023	20.3123	1.3	0.0045	11.7	0.0937	4.4	0.0138	4.2	158.9	30.5	90.6	10.6	91.0	3.8	88.4	3.7
16	306	44714	0.007	21.9527	3.7	0.0044	5.1	0.0837	4.4	0.0133	2.3	-26.0	90.4	88.5	4.5	81.7	3.5	85.4	2.0
17	543	33717	0.016	21.4665	1.9	0.0045	4.0	0.0920	3.0	0.0143	2.4	27.9	45.0	90.2	3.6	89.4	2.6	91.7	2.2
18	3235	31769	0.102	20.9535	0.5	0.0045	4.4	0.0949	3.4	0.0144	3.3	85.7	12.8	90.0	3.9	92.1	3.0	92.3	3.0
19	745	35480	0.021	22.2294	2.0	0.0046	5.6	0.0917	5.2	0.0148	4.8	-56.4	49.4	92.7	5.2	89.1	4.4	94.6	4.5
20	506	42508	0.012	21.1549	2.5	0.0046	2.1	0.0925	4.4	0.0142	3.6	62.9	60.0	92.1	2.0	89.8	3.8	90.8	3.2
21	557	30113	0.019	20.4728	3.2	0.0046	1.3	0.0980	5.1	0.0145	4.0	140.4	74.6	92.5	1.2	94.9	4.6	93.1	3.7
22	2627	25729	0.102	20.9847	0.7	0.0044	6.0	0.0915	8.0	0.0139	8.0	82.1	15.6	87.9	5.3	88.9	6.8	89.2	7.1
23	1145	43682	0.026	20.1919	1.3	0.0045	2.7	0.0954	3.2	0.0140	3.0	172.7	29.4	90.3	2.4	92.5	2.9	89.4	2.6
24	3642	23479	0.155	21.1333	0.7	0.0045	2.8	0.0941	2.9	0.0144	2.8	65.3	15.7	91.3	2.5	91.4	2.5	92.4	2.6
25	1471	33964	0.043	20.9961	1.5	0.0045	5.1	0.0962	2.6	0.0146	2.1	80.8	36.0	91.0	4.6	93.2	2.3	93.7	2.0
26	1114	31796	0.035	21.1436	1.1	0.0044	3.3	0.0925	3.0	0.0142	2.9	64.2	25.1	88.8	2.9	89.8	2.6	90.8	2.6
Cores																			
1	761	40399	0.019	19.2226	1.5	0.0045	4.9	0.1007	2.5	0.0140	2.0	286.4	34.3	89.9	4.4	97.5	2.3	89.9	1.8
3	511	32227	0.016	20.5642	2.2	0.0047	4.1	0.0961	4.3	0.0143	3.7	129.9	51.3	94.7	3.9	93.2	3.8	91.8	3.4
4	653	38284	0.017	20.7700	2.0	0.0045	3.6	0.0957	3.2	0.0144	2.5	106.4	46.6	91.6	3.3	92.8	2.9	92.3	2.3
9	1004	31004	0.032	21.4317	1.8	0.0044	1.6	0.0908	2.1	0.0141	1.2	31.9	42.0	89.6	1.4	88.2	1.8	90.3	1.1
12	780	51579	0.015	20.3055	2.3	0.0044	6.1	0.0941	3.5	0.0139	2.6	159.7	54.2	88.3	5.4	91.3	3.0	88.7	2.3
15	892	42823	0.021	20.9851	0.8	0.0045	3.8	0.0912	3.3	0.0139	3.2	82.0	18.6	90.2	3.4	88.7	2.8	88.9	2.9
Sample 13WM30 - *Schlieren-textured granodiorite diatexite (N44.40779°, W116.13957°)*																			
1	555	40074	0.014	20.2891	2.0	0.0047	2.0	0.0994	4.5	0.0146	4.0	161.5	46.7	94.5	1.9	96.3	4.1	93.6	3.7
2	2135	51612	0.041	21.1799	0.6	0.0045	2.3	0.0944	2.5	0.0145	2.5	60.1	14.2	90.5	2.1	91.6	2.2	92.8	2.3
3	2182	35685	0.061	20.7064	1.2	0.0045	8.2	0.0921	9.9	0.0138	9.8	113.7	28.0	91.2	7.5	89.4	8.5	88.5	8.6
5	1262	43751	0.029	21.0521	0.7	0.0041	5.7	0.0917	1.7	0.0140	1.5	74.5	17.8	83.5	4.7	89.0	1.4	89.6	1.3
6	404	45136	0.009	19.9669	2.1	0.0045	5.4	0.0966	4.5	0.0140	4.0	198.8	47.9	91.0	4.9	93.7	4.1	89.6	3.6
7	727	36489	0.020	20.4843	1.5	0.0047	9.7	0.1015	4.5	0.0151	4.2	139.1	35.2	93.9	9.1	98.1	4.2	96.5	4.1
8	559	30326	0.018	21.5641	2.1	0.0045	2.6	0.0902	4.8	0.0141	4.3	17.1	50.4	90.8	2.4	87.7	4.0	90.3	3.9
9	306	38511	0.008	20.2009	5.9	0.0046	2.8	0.0929	9.4	0.0136	7.3	171.7	137.3	91.8	2.6	90.2	8.1	87.2	6.3
10	662	18330	0.036	22.0375	1.3	0.0050	5.3	0.0980	5.7	0.0157	5.5	-35.3	30.8	101.6	5.3	95.0	5.1	100.2	5.5
11	821	71061	0.012	23.0444	1.8	0.0044	6.3	0.0852	2.9	0.0142	2.3	-144.9	43.7	88.0	5.5	83.0	2.3	91.1	2.1

TABLE 2. Summary of LA-ICP-MS U-Pb monazite results for migmatitic rocks in the Potters Pond migmatite domain — Continued

				Isotope Ratios								Ages (in Ma)							
Grain Number	U (ppm)	Th (ppm)	U/Th	$^{206}Pb^*$ / $^{207}Pb^*$	±1σ (%)	$^{208}Pb^*$ / ^{232}Th	±1σ (%)	$^{207}Pb^*$ / ^{235}U	±1σ (%)	$^{206}Pb^*$ / ^{238}U	±1σ (%)	$^{206}Pb^*$ / $^{207}Pb^*$	±1σ (%)	$^{208}Pb^*$ / ^{232}Th	±1σ (%)	$^{207}Pb^*$ / ^{235}U	±1σ (%)	$^{206}Pb^*$ / ^{238}U	±1σ (%)
12	747	69620	0.011	21.2471	0.8	0.0044	3.1	0.0934	3.9	0.0144	3.8	52.5	18.6	89.0	2.8	90.7	3.4	92.2	3.5
13	263	17718	0.015	20.2440	3.5	0.0046	10.2	0.0995	5.2	0.0146	3.9	166.7	81.7	93.1	9.5	96.3	4.8	93.5	3.6
14	882	57786	0.015	21.2706	2.1	0.0044	3.7	0.0916	7.4	0.0141	7.1	49.9	50.6	88.8	3.3	89.0	6.3	90.4	6.4
15	456	30239	0.015	21.0755	1.7	0.0048	2.9	0.1002	3.1	0.0153	2.6	71.9	40.4	95.8	2.7	97.0	2.8	98.0	2.5
16	580	39596	0.015	22.2308	1.9	0.0046	2.8	0.0906	6.3	0.0146	6.0	-56.6	46.1	92.6	2.6	88.1	5.3	93.5	5.6
17	1758	27719	0.063	20.9285	0.9	0.0046	13.3	0.1026	4.4	0.0156	4.3	88.5	21.0	93.7	12.4	99.2	4.1	99.6	4.3
18	882	40336	0.022	21.2139	0.8	0.0044	2.4	0.0960	6.7	0.0148	6.7	56.3	19.2	88.7	2.1	93.1	6.0	94.5	6.3
19	680	32719	0.021	15.8769	8.1	0.0045	1.9	0.1165	8.2	0.0134	1.3	707.7	172.3	90.3	1.7	111.9	8.7	85.9	1.1
20	438	38356	0.011	22.3292	2.0	0.0044	2.2	0.0831	7.4	0.0135	7.1	-67.3	49.7	89.3	2.0	81.1	5.8	86.2	6.1
21	451	35072	0.013	21.3670	1.2	0.0046	1.0	0.0927	4.1	0.0144	4.0	39.1	28.6	93.5	1.0	90.0	3.6	92.0	3.6
22	513	37383	0.014	24.0904	1.7	0.0046	2.3	0.0872	3.2	0.0152	2.7	-256.1	44.2	93.3	2.2	84.9	2.6	97.5	2.6
23	457	21186	0.022	20.4697	3.6	0.0047	3.0	0.0939	6.3	0.0139	5.2	140.8	84.3	94.8	2.9	91.2	5.5	89.3	4.6
25	1417	31715	0.045	21.3340	1.5	0.0047	5.5	0.0966	4.5	0.0149	4.2	42.8	36.2	94.8	5.2	93.6	4.0	95.6	4.0
26	301	44911	0.007	19.5477	4.3	0.0045	5.2	0.0931	5.0	0.0132	2.5	247.9	98.5	90.5	4.7	90.4	4.3	84.5	2.1
27	730	43202	0.017	22.8289	1.1	0.0046	1.9	0.0859	3.3	0.0142	3.1	-121.7	27.6	91.8	1.8	83.7	2.7	91.0	2.8
29	826	32514	0.025	22.2416	1.3	0.0043	3.6	0.0872	2.8	0.0141	2.4	-57.8	32.3	87.3	3.1	84.8	2.2	90.0	2.2
30	309	29054	0.011	22.4137	2.9	0.0047	2.6	0.0861	3.7	0.0140	2.2	-76.6	71.5	94.5	2.5	83.9	2.9	89.6	2.0
Sample 14WM37a - *Discordant leucosome in stromatic metatexite (N44.41924°, W116.13478°)*																			
Rims																			
1	2158	51314	0.042	21.4102	1.4	0.0046	2.9	0.0907	2.4	0.0141	2.0	34.3	34.1	92.3	2.7	88.1	2.1	90.1	1.8
3	2202	45715	0.048	20.8844	1.4	0.0046	2.9	0.0968	3.4	0.0147	3.1	93.5	33.8	93.3	2.7	93.8	3.1	93.8	2.9
5	1993	7824	0.255	21.0412	1.4	0.0043	2.7	0.0893	4.3	0.0136	4.1	75.7	32.6	86.4	2.3	86.9	3.6	87.3	3.6
6	522	38718	0.013	21.5853	1.3	0.0047	4.6	0.1064	6.0	0.0167	5.8	14.7	32.2	95.0	4.4	102.6	5.8	106.5	6.1
8	1418	77952	0.018	21.1302	1.1	0.0044	7.3	0.0943	7.8	0.0145	7.7	65.7	27.1	88.1	6.4	91.5	6.9	92.5	7.1
9	809	52193	0.015	21.8427	1.5	0.0044	2.9	0.1065	5.5	0.0169	5.3	-13.8	36.5	89.3	2.6	102.8	5.4	107.9	5.7
11	1084	67144	0.016	20.1806	1.5	0.0046	1.4	0.0996	2.9	0.0146	2.5	174.0	35.4	91.8	1.3	96.4	2.7	93.3	2.3
13	1035	72175	0.014	20.0004	1.6	0.0045	3.4	0.0942	4.0	0.0137	3.7	195.0	37.9	89.8	3.1	91.4	3.5	87.5	3.2
16	1769	45665	0.039	20.7835	1.5	0.0047	3.4	0.0996	5.2	0.0150	4.9	104.9	36.4	94.3	3.2	96.4	4.8	96.1	4.7
17	1674	54571	0.031	21.2291	1.3	0.0046	2.9	0.0957	4.8	0.0147	4.7	54.6	30.4	93.5	2.7	92.8	4.3	94.3	4.4
18	1375	87559	0.016	20.9945	0.9	0.0044	2.8	0.0953	3.9	0.0145	3.8	81.0	22.0	88.5	2.5	92.4	3.5	92.9	3.5
19	2922	49291	0.059	20.7225	0.6	0.0047	9.6	0.0988	4.4	0.0149	4.4	111.9	15.0	95.5	9.2	95.7	4.0	95.1	4.1
20	1018	45575	0.022	21.5575	1.8	0.0045	1.6	0.0903	3.0	0.0141	2.4	17.8	42.8	90.9	1.5	87.8	2.5	90.3	2.2
21	2121	93967	0.023	21.1452	0.7	0.0044	4.5	0.0966	5.6	0.0148	5.6	64.0	15.5	89.1	4.0	93.6	5.0	94.8	5.3
22	1179	89639	0.013	21.4364	1.0	0.0044	2.3	0.0897	4.5	0.0140	4.4	31.3	23.5	88.1	2.0	87.3	3.8	89.3	3.9
Cores																			
1	1256	67819	0.019	20.8441	1.3	0.0044	2.5	0.0957	7.9	0.0145	7.8	98.1	30.9	89.6	2.2	92.8	7.0	92.6	7.2
2	1092	47096	0.023	20.9402	1.2	0.0048	2.9	0.0983	4.2	0.0149	4.0	87.2	28.0	95.8	2.7	95.2	3.8	95.5	3.8
3	1609	52273	0.031	20.6593	1.4	0.0046	2.3	0.0977	2.7	0.0146	2.2	119.1	33.8	92.9	2.2	94.7	2.4	93.7	2.1
9	1465	48803	0.030	20.4601	1.6	0.0047	3.8	0.1014	4.6	0.0151	4.3	141.9	38.4	94.1	3.5	98.1	4.3	96.3	4.1
11	1606	59938	0.027	20.7692	1.2	0.0046	1.6	0.0970	3.5	0.0146	3.3	106.5	28.0	92.1	1.4	94.0	3.1	93.5	3.1
12	1063	54819	0.019	20.0257	1.6	0.0046	2.3	0.1017	2.3	0.0148	1.7	192.0	37.9	92.7	2.1	98.4	2.2	94.6	1.6
13	1588	51985	0.031	20.0681	1.1	0.0044	3.7	0.0938	3.2	0.0137	3.1	187.1	24.8	89.2	3.3	91.0	2.8	87.4	2.6
14	1859	50114	0.037	20.6560	1.1	0.0045	3.0	0.1003	7.5	0.0150	7.4	119.5	26.6	91.0	2.7	97.0	6.9	96.1	7.0
15	547	68233	0.008	22.1736	2.2	0.0044	2.9	0.0869	3.2	0.0140	2.3	-50.3	53.7	88.8	2.6	84.7	2.6	89.5	2.0
16	1024	54047	0.019	20.9863	1.2	0.0044	4.5	0.0959	5.7	0.0146	5.6	81.9	28.6	89.5	4.0	93.0	5.1	93.4	5.2
18	1104	79226	0.014	20.3595	1.4	0.0044	4.4	0.0965	4.1	0.0142	3.8	153.4	33.3	88.7	3.9	93.5	3.6	91.2	3.5
19	1899	51627	0.037	21.1952	1.7	0.0046	1.7	0.0997	3.6	0.0153	3.2	58.4	40.0	93.5	1.6	96.5	3.3	98.0	3.1
22	412	63471	0.006	21.4490	1.5	0.0044	4.5	0.0888	3.6	0.0138	3.3	29.9	35.9	89.3	4.0	86.4	3.0	88.4	2.9
Sample 14WM39a - *Boudinaged leucosome within melanocratic diatexite (N44.41895°, W116.13708°)*																			
Rims																			
1	1359	61976		20.2993	2.8	0.0044	6.0	0.0945	5.2	0.0139	4.3	160.4	65.5	89.7	5.4	91.7	4.5	89.1	3.8
2	993	64699		17.3563	1.2	0.0046	3.7	0.1142	1.8	0.0144	1.3	515.2	26.8	92.3	3.4	109.8	1.8	92.0	1.2
3	2815	69724		21.0361	0.7	0.0045	3.0	0.0949	2.9	0.0145	2.8	76.3	17.7	90.1	2.7	92.0	2.6	92.7	2.6
4	2238	64291		19.4329	0.9	0.0046	4.6	0.1011	4.0	0.0142	3.9	261.4	21.0	92.6	4.3	97.8	3.8	91.2	3.6
5	1285	67125		21.2985	2.1	0.0045	5.1	0.0895	4.2	0.0138	3.7	46.8	50.1	89.8	4.5	87.1	3.5	88.6	3.2

TABLE 2. Summary of LA-ICP-MS U-Pb monazite results for migmatitic rocks in the Potters Pond migmatite domain — Continued

Grain Number	U (ppm)	Th (ppm)	U/Th	Isotope Ratios $^{208}Pb^*/^{207}Pb^*$	±1σ (%)	$^{208}Pb^*/^{232}Th$	±1σ (%)	$^{207}Pb^*/^{235}U$	±1σ (%)	$^{206}Pb^*/^{238}U$	±1σ (%)	Ages (in Ma) $^{206}Pb^*/^{207}Pb^*$	±1σ (%)	$^{208}Pb^*/^{232}Th$	±1σ (%)	$^{207}Pb^*/^{235}U$	±1σ (%)	$^{206}Pb^*/^{238}U$	±1σ (%)
6	1066	60744		18.0623	1.2	0.0044	4.3	0.1054	4.7	0.0138	4.5	426.9	26.9	89.5	3.9	101.8	4.6	88.4	4.0
7	2881	60740		21.4973	2.0	0.0045	7.2	0.0904	3.9	0.0141	3.3	24.5	48.4	91.4	6.6	87.8	3.2	90.2	3.0
8	1825	68755		18.7375	1.6	0.0045	5.0	0.1029	4.2	0.0140	3.9	344.5	36.3	91.4	4.5	99.4	4.0	89.5	3.5
9	1516	60989		21.3277	1.8	0.0044	4.1	0.0950	2.5	0.0147	1.8	43.5	42.1	89.6	3.7	92.1	2.2	94.0	1.7
10	1102	58003		21.8006	1.6	0.0043	2.0	0.0867	3.1	0.0137	2.6	-9.2	39.6	86.2	1.7	84.4	2.5	87.7	2.3
11	777	63335		20.0634	1.9	0.0045	4.1	0.0937	3.2	0.0136	2.6	187.6	44.4	89.8	3.6	91.0	2.8	87.3	2.2
12	1322	59197		21.1812	1.9	0.0045	2.5	0.0912	5.4	0.0140	5.0	59.9	45.9	90.1	2.2	88.6	4.6	89.7	4.5
13	1506	67320		20.5006	1.3	0.0044	3.5	0.0939	4.0	0.0140	3.8	137.2	31.0	88.7	3.1	91.1	3.5	89.4	3.4
14	1055	62610		19.9381	1.2	0.0043	9.5	0.0955	8.0	0.0138	7.9	202.2	28.0	86.8	8.2	92.6	7.1	88.4	6.9
15	1058	58006		17.8213	1.2	0.0044	2.0	0.1047	3.8	0.0135	3.6	456.8	26.3	88.3	1.8	101.1	3.6	86.6	3.1
16	1807	61334		19.6545	1.0	0.0045	4.8	0.1007	1.8	0.0144	1.4	235.4	23.4	91.2	4.4	97.5	1.6	91.9	1.3
17	2768	80127		20.1196	0.8	0.0044	2.7	0.0964	4.0	0.0141	4.0	181.1	17.5	89.1	2.4	93.5	3.6	90.1	3.5
Cores																			
3	1975	69891		19.2554	0.7	0.0048	1.9	0.1095	1.9	0.0153	1.8	282.5	16.6	96.9	1.9	105.5	1.9	97.9	1.7
4	1833	65962		20.7859	1.3	0.0046	0.9	0.0949	5.1	0.0143	5.0	104.6	30.1	92.1	0.8	92.1	4.5	91.6	4.5
6	1202	62593		17.9899	1.0	0.0045	3.5	0.1085	3.9	0.0142	3.8	435.9	22.4	91.1	3.1	104.6	3.9	90.6	3.4
7	2224	56304		20.8434	0.8	0.0045	5.0	0.0924	4.5	0.0140	4.4	98.2	18.0	89.8	4.5	89.7	3.9	89.4	3.9
8	1663	66697		21.2965	1.6	0.0044	2.8	0.0907	3.8	0.0140	3.5	47.0	39.2	88.8	2.5	88.2	3.2	89.7	3.1
11	1364	63105		21.9289	2.8	0.0045	5.3	0.0864	6.9	0.0137	6.3	-23.4	68.9	89.7	4.8	84.1	5.6	88.0	5.5
Sample 14WM58 - *Nebulitic diatexite (N44.42994°, W116.13438°)*																			
Rims																			
1	2334	57903		20.5318	1.2	0.0046	7.1	0.1002	4.9	0.0149	4.8	133.6	28.4	93.4	6.7	97.0	4.5	95.5	4.5
2	1399	43224		20.6453	1.3	0.0045	3.1	0.0952	4.6	0.0143	4.4	120.7	31.3	90.3	2.8	92.4	4.0	91.3	4.0
3	1016	44047		21.6402	1.2	0.0045	1.7	0.0916	4.7	0.0144	4.5	8.6	28.2	91.5	1.5	89.0	4.0	92.0	4.1
5	1657	40374		20.4753	0.6	0.0045	4.4	0.0944	4.0	0.0140	4.0	140.1	13.0	91.2	4.0	91.6	3.5	89.7	3.6
6	1169	45487		20.9768	1.1	0.0045	2.7	0.0962	3.2	0.0146	3.0	83.0	25.0	91.1	2.4	93.2	2.8	93.6	2.8
7	653	54494		19.5378	2.1	0.0046	6.7	0.1001	3.2	0.0142	2.4	249.1	48.3	92.1	6.2	96.9	2.9	90.8	2.2
8	2529	46983		20.6135	1.2	0.0046	3.8	0.0939	4.0	0.0140	3.8	124.3	28.4	92.2	3.5	91.1	3.5	89.9	3.4
9	1976	49720		20.4471	1.5	0.0046	2.9	0.0948	3.4	0.0141	3.0	143.3	35.1	91.8	2.6	91.9	3.0	90.0	2.7
10	1948	39598		20.1903	0.7	0.0044	16.4	0.0960	2.6	0.0141	2.5	172.9	16.8	89.0	14.6	93.1	2.3	90.0	2.2
12	1226	44798		20.4199	1.4	0.0045	4.6	0.0980	5.4	0.0145	5.2	146.5	33.6	91.4	4.2	94.9	4.9	92.9	4.8
13	1149	41547		20.2453	1.4	0.0045	5.4	0.0981	5.1	0.0144	4.9	166.6	32.1	90.7	4.9	95.0	4.6	92.2	4.5
14	1444	43356		20.6156	1.0	0.0045	2.1	0.0949	5.2	0.0142	5.1	124.0	24.3	91.2	1.9	92.1	4.5	90.8	4.6
15	1418	41994		20.4299	1.1	0.0045	5.0	0.0947	4.2	0.0140	4.1	145.3	25.2	90.1	4.5	91.9	3.7	89.8	3.6
16	1002	43551		21.9395	1.8	0.0045	3.4	0.0912	6.5	0.0145	6.2	-24.5	44.2	90.9	3.1	88.7	5.5	92.9	5.7
17	1007	46087		20.7416	1.4	0.0045	2.1	0.0957	3.9	0.0144	3.6	109.7	34.0	90.9	1.9	92.8	3.5	92.2	3.3
19	2654	62996		20.1365	0.5	0.0046	3.3	0.1015	2.8	0.0148	2.7	179.1	12.7	92.3	3.1	98.1	2.6	94.8	2.6
20	846	48673		21.1695	1.9	0.0045	4.7	0.0921	3.1	0.0141	2.5	61.3	44.3	89.9	4.2	89.5	2.7	90.5	2.3
21	2233	53240		21.2689	1.0	0.0046	2.7	0.0950	4.0	0.0147	3.9	50.1	24.7	93.1	2.6	92.2	3.5	93.8	3.6
22	1591	40498		20.9356	1.2	0.0045	2.3	0.0947	4.6	0.0144	4.4	87.7	28.1	91.4	2.1	91.9	4.0	92.0	4.1
23	1239	50012		20.8187	1.2	0.0044	6.7	0.0941	6.4	0.0142	6.3	100.9	28.9	88.9	5.9	91.3	5.6	90.9	5.7
Cores																			
1	3009	58020		20.6792	1.2	0.0046	3.5	0.0954	7.4	0.0143	7.3	116.8	29.3	93.2	3.2	92.6	6.5	91.6	6.6
2	613	19238		22.4472	2.1	0.0049	2.8	0.0967	3.8	0.0157	3.1	-80.2	52.0	99.5	2.8	93.7	3.4	100.7	3.1
3	449	19512		21.2249	1.8	0.0050	5.3	0.1027	5.6	0.0158	5.3	55.0	42.3	99.9	5.3	99.3	5.3	101.2	5.3
5	1093	25679		20.5536	1.0	0.0048	6.4	0.1060	2.0	0.0158	1.7	131.1	22.5	95.8	6.1	102.3	1.9	101.1	1.8
6	1232	47248		20.2748	1.6	0.0046	2.7	0.0978	4.2	0.0144	3.9	163.2	36.9	91.7	2.5	94.8	3.8	92.1	3.6
8	2603	55903		20.4399	1.2	0.0046	6.5	0.0971	4.8	0.0144	4.6	144.2	29.3	92.1	6.0	94.1	4.3	92.1	4.2
8	1581	25148		20.7873	1.1	0.0049	8.2	0.1031	6.2	0.0155	6.1	104.5	26.8	99.2	8.2	99.7	5.9	99.5	6.0
9	929	54490		20.1970	2.0	0.0045	3.0	0.0949	5.2	0.0139	4.9	172.1	45.7	91.0	2.7	92.0	4.6	89.0	4.3
10	1220	43740		21.0859	0.8	0.0044	9.9	0.0925	2.3	0.0141	2.1	70.7	20.0	88.4	8.7	89.8	2.0	90.5	1.9
12	1515	45565		21.2801	1.2	0.0044	3.3	0.0906	5.2	0.0140	5.0	48.8	29.3	89.7	2.9	88.0	4.3	89.5	4.5
14	994	43422		20.6976	1.9	0.0045	4.3	0.0946	5.1	0.0142	4.7	114.7	45.3	90.7	3.9	91.8	4.5	90.9	4.3
17	1313	44252		22.2992	1.7	0.0044	7.3	0.0864	9.6	0.0140	9.4	-64.1	42.2	88.3	6.4	84.2	7.7	89.5	8.4

TABLE 2. Summary of LA-ICP-MS U-Pb monazite results for migmatitic rocks in the Potters Pond migmatite domain — Continued

Grain Number	U (ppm)	Th (ppm)	U/Th	Isotope Ratios $^{206}Pb^*/^{207}Pb^*$	±1σ (%)	$^{208}Pb^*/^{232}Th$	±1σ (%)	$^{207}Pb^*/^{235}U$	±1σ (%)	$^{206}Pb^*/^{238}U$	±1σ (%)	Ages (in Ma) $^{206}Pb^*/^{207}Pb^*$	±1σ (%)	$^{208}Pb^*/^{232}Th$	±1σ (%)	$^{207}Pb^*/^{235}U$	±1σ (%)	$^{206}Pb^*/^{238}U$	±1σ (%)
Sample 14WM115 - *Agmatic diatexite (44.43280°, W116.14230°)*																			
Rims																			
1	1840	170476	0.011	20.7036	2.7	0.0044	5.7	0.0969	4.9	0.0145	4.0	114.0	64.5	89.7	5.1	93.9	4.4	93.1	3.7
1R	1742	168998	0.010	20.7600	1.4	0.0046	2.4	0.0976	2.5	0.0147	2.0	107.6	33.6	92.7	2.2	94.6	2.2	94.0	1.9
1RR	1747	170796	0.010	20.5327	2.0	0.0046	11.1	0.0966	9.1	0.0144	8.9	133.6	47.0	91.7	10.2	93.6	8.2	92.1	8.1
1RRR	2115	166425	0.013	19.8023	1.4	0.0044	8.4	0.1000	4.3	0.0144	4.0	218.1	33.4	88.7	7.5	96.8	4.0	92.0	3.7
1(R)	2103	172796	0.012	20.9328	0.7	0.0045	6.6	0.0953	9.2	0.0145	9.1	88.0	16.7	89.9	5.9	92.4	8.1	92.6	8.4
2	2532	156404	0.016	20.9341	1.8	0.0044	4.8	0.0955	4.4	0.0145	4.0	87.9	43.6	89.6	4.3	92.6	3.9	92.8	3.7
2R	3589	136259	0.026	20.9869	1.6	0.0043	5.0	0.0916	3.2	0.0139	2.7	81.8	38.1	86.3	4.3	88.9	2.7	89.2	2.4
2RR	2227	147112	0.015	20.7617	2.0	0.0043	4.6	0.0953	6.0	0.0143	5.7	107.4	47.2	87.5	4.0	92.4	5.3	91.8	5.2
2RRR	2539	161389	0.016	21.0079	1.1	0.0044	3.5	0.0937	4.7	0.0143	4.6	79.5	25.0	88.6	3.1	90.9	4.1	91.4	4.2
2(RR)	2141	180860	0.012	20.8790	2.1	0.0044	3.9	0.0974	4.6	0.0148	4.1	94.1	49.6	89.0	3.4	94.4	4.1	94.4	3.8
Cores																			
1C	1847	195494	0.009	21.0439	2.0	0.0044	10.1	0.0943	7.4	0.0144	7.1	75.4	48.7	89.6	9.0	91.5	6.4	92.1	6.5
1CC	1801	196825	0.009	20.5897	1.6	0.0045	5.1	0.0961	3.6	0.0143	3.2	127.1	38.8	90.1	4.5	93.1	3.2	91.8	3.0
1CCC	1778	191234	0.009	20.9003	3.0	0.0045	1.7	0.0960	3.7	0.0146	2.3	91.7	70.2	91.0	1.6	93.1	3.3	93.1	2.1
2C	1864	142648	0.013	21.1964	1.4	0.0044	5.0	0.0924	3.1	0.0142	2.8	58.2	32.4	87.9	4.4	89.8	2.7	91.0	2.5
2CC	1910	156642	0.012	20.9691	2.1	0.0043	5.1	0.0950	3.7	0.0145	3.1	83.9	50.5	87.1	4.5	92.2	3.3	92.5	2.8
2CCC	2318	171061	0.014	21.1172	1.4	0.0043	2.9	0.0954	1.9	0.0146	1.2	67.1	32.9	87.4	2.6	92.5	1.6	93.5	1.2

Standard analyses with >10% uncertainty (1-sigma) in 206Pb/238U age are not included.
Standard analyses with >10% uncertainty (1-sigma) in 206Pb/207Pb age are not included, unless 206Pb/238U age is <600 Ma.
All uncertainties are reported at the 1-sigma level, and include only measurement errors.
Systematic errors are as follows (at 2-sigma level): [Sample: 13WM025: 1.5% (206Pb/238U), 1.2% (208Pb/232Th); Sample: 14WM037a: 1.2% (206Pb/238U), 1.4% (208Pb/232Th);
Sample: 13MW058: 1.2% (206Pb/238U), 1.4% (208Pb/232Th); Sample: 13WM030: 1.7% (206Pb/238U), 1.1% (208Pb/232Th); Sample: 14WM039a: 1.2% (206Pb/238U), 1.4% (208Pb/232Th)].
Analyses conducted by LA-MC-ICPMS, as described by Gehrels et al. (2008).
U concentration and U/Th are calibrated relative to 44069 monazite standard and are accurate to ~20%.
Common Pb correction is from measured 204Pb with common Pb composition interpreted from Stacey and Kramers (1975).
Common Pb composition assigned uncertainties of 1.5 for 206Pb/204Pb, 0.3 for 207Pb/204Pb, and 2.0 for 208Pb/204Pb.
U/Pb and 206Pb/207Pb fractionation is calibrated relative to individual grains of 44069 monazite with an ID-TIMS age of 424.9 ± 0.4 Ma (2-sigma).
U and Th decay constants and U composition as follows: 235U = 9.8485 x 10-10, 238U = 1.55125 x 10-10, 232Th =4.9475 x 10-11, 238U/235U = 137.88.
Weighted mean and concordia plots constructed using Isoplot 3.75 (Ludwig, 2012), with uncertainties reported at the 2-sigma level, and incorporate both the measurement and instrumental errors.

APPENDIX A: ANALYTICAL METHODS

U-Pb geochronologic analysis of zircon (Element2 HR ICPMS)

Zircon crystals are extracted from samples by traditional methods of crushing and grinding, followed by separation with a Wilfley table, heavy liquids, and a Frantz magnetic separator. Samples are processed such that all zircons are retained in the final heavy mineral fraction. Approximately 50 high-quality grains are selected and mounted into 1" expoxy mounts with fragments or loose grains of Sri Lanka, FC-1, and R33 zircon crystals that are used as primary standards. The mounts were sanded down to a depth of ~20 microns, polished, imaged, and cleaned prior to isotopic analysis.

Pre-acquisition cathodoluminescence imaging of zircon was conducted at University of Arizona using a Hitachi 3400N SEM and a Gatan CL2 detector system (www.geoarizonasem.org) to provide a guide for locating analysis pits in textural domains (e.g., core and rim overgrowths).

U-Pb geochronology of zircons was conducted by laser ablation inductively coupled plasma mass spectrometry (LA-ICPMS) at the Arizona LaserChron Center (Gehrels et al., 2006, 2008; Gehrels and Pecha, 2014). The analyses involve ablation of zircon with a Photon Machines Analyte G2 excimer laser equipped with HelEx ablation cell using a spot diameter of 20 microns. The ablated material is carried in helium into the plasma source of an Element2 HR ICPMS, which sequences rapidly through U, Th, and Pb isotopes. Signal intensities are measured with an SEM that operates in pulse counting mode for signals less than 50K cps, in both pulse-counting and analog mode for signals between 50K and 4M cps, and in analog mode above 4M cps. The calibration between pulse-counting and analog signals is determined line-by-line for signals between 50K and 4M cps, and is applied to 4M cps signals. Four intensities are determined and averaged for each isotope, with dwell times of 0.0052 sec for 202, 0.0075 sec for 204, 0.0202 sec for 206, 0.0284 sec for 207, 0.0026 sec for 208, 0.0026 sec for 232, and 0.0104 sec for 238.

With the laser set an energy density of ~5 J/cm2, a repetition rate of 8 hz, and an ablation time of 10 seconds, ablation pits are ~12 microns in depth. Sensitivity with these

settings is approximately ~5,000 cps/ppm. Each analysis consists of 5 sec on peaks with the laser off (for backgrounds), 10 sec with the laser firing (for peak intensities), and a 20 second delay to purge the previous sample and save files.

U-Pb/Th-Pb geochronologic analysis of monazite (Nu Instruments HR-MC-ICPMS)

U-Pb/Th-Pb geochronology of individual monazite crystals was conducted by laser ablation multicollector inductively coupled mass spectrometry (LA-MC-ICPMS) at the Arizona LaserChron Center (Gehrels et al., 2006, 2008). The isotopic analyses involved ablation of monazite using a Photon Machines Analyte G2 excimer laser (λ = 193 nm) coupled to a Nu Instruments HR-MC-ICPMS. Helium carries the ablated material into the plasma source of the ICPMS, which is equipped with a flight tube of sufficient width such that U, Th, and Pb isotopes are measured simultaneously. Analyses were conducted with a 6 micron laser spot diameter using an acquisition routine consisting of one 9 second integration on peaks with the laser off (for backgrounds), 9 one-second integrations with the laser firing, and a 30 second delay to ensure the previous sample is purged from the collector block. Operating parameters for the excimer laser were maintained at ~10 J/cm^2 at 5 Hz in constant energy mode for 65 laser bursts per analysis, producing an ablation depth of ~ 6 microns. Faraday detectors with 3x10^{11} ohm resistors measure ^{238}U, ^{232}Th, and discrete dynode ion counters measure $^{208\text{-}204}$Pb, all in static mode.

The errors in determining the ^{206}Pb/^{238}U and ^{206}Pb/^{204}Pb result in a final measurement error of ~1-2% (at 2-sigma level) in the ^{206}Pb/^{238}U age for each analysis. The errors in determining ^{206}Pb/^{207}Pb and ^{206}Pb/^{204}Pb also result in ~1-2% (at 2-sigma level) uncertainty in age for grains that are older than 900 Ma; however, they are substantially larger for younger grains due to the low intensity of the ^{207}Pb signal. The errors in determining the ^{208}Pb/^{232}Th and ^{208}Pb/^{204}Pb result in a final measurement of ~1-2% (at 2-sigma level) in the ^{208}Pb/^{232}Th age for each analysis.

The common Pb correction is accomplished by using the Hg-corrected ^{204}Pb and assuming an initial Pb composition from Stacey and Kramers (1975). Uncertainties of 1.5 for ^{206}Pb/^{204}Pb and 0.3 for ^{207}Pb/^{204}Pb are applied to these compositional values based

on the variation in Pb isotopic composition in modern crystalline rocks. Interference of ^{204}Hg with ^{204}Pb is accounted for measurement of ^{202}Hg during laser ablation and subtraction of ^{204}Hg according to the natural ^{202}Hg/^{204}Hg of 4.35.

The 6 micron spot diameter in conjunction with the 9 second analysis routine (65 bursts at a 5Hz repetition) was used to minimize both spatial and at-depth mixing of multiple age domains. Grain selection and spot placements were based on the high resolution BSE images, for grains where there was a large difference in compositional domains multiple analyses were performed.

Data Reduction

Following analysis, data reduction was performed using an in-house Python decoding routine and an Excel spreadsheet (E2agecalc) that:

1. Decodes .dat files from the Thermo software such individual intensities for measurement are available (routine written by John Hartman, University of Arizona)

2. Imports intensities and a sample name for each analysis

3. Calculates average intensities for each isotope (based on the sum of all counts while the laser is firing)

4. Subtracts ^{204}Hg from the 204 signal to yield ^{204}Pb intensity (using natural ^{202}Hg/^{204}Hg of 4.3). This Hg correction is not significant for most analyses because our Hg backgrounds are low (generally ~150 cps at mass 204).

5. Performs a common Pb correction based on the measured ^{206}Pb/^{204}Pb and the assumed composition of common Pb based on Stacey and Kramers (1975)

6. Calculates measured 206/238, 206/207, and 208/232 ratios

7. Compares measured and known ratios for the three standards to determine fractionation factors for 206/238, 206/207, and 208/232. These correction factors are generally <5% for 206/238, <2% for 206/207, and <20% for 208/232.

8. Determines an overdispersion factor if the standard analyses show greater dispersion than expected from measurement uncertainties

9. Uses a sliding-window average to apply fractionation factors to unknowns (generally averaging 8 standard analyses)

10. Calculates fractionation-corrected 206/238, 206/207, and 208/232 ratios and ages for unknowns

11. Propagates measurement uncertainties for 206/238 and 208/232 that are based on the scatter about a regression of measured values. Uncertainties for 206/207 and 206/204 are based on the standard deviation of measured values since these ratios generally do not change during an analysis. The sum of this uncertainty and any overdispersion factor is reported as the internal (or measurement) uncertainty for each analysis. These uncertainties are reported at the 1-sigma level.

12. Calculates the down-hole slope of 206/238 to highlight analyses in which 206/238 is compromised due to heterogeneity in age (e.g., crossing an age boundary) or intersection of a fracture or inclusion.

13. Calculates concentrations of U and Th for unknowns based on the measured intensity and known concentrations of FC-1.

14. Calculates the external (systematic) uncertainties for 206/238, 206/207, and 208/232, which include contributions from (a) the scatter of standard analyses, (b) uncertainties in the ages of the standards, (c) uncertainties in the composition of common Pb, and (4) uncertainties in the decay constants for ^{235}U and ^{238}U.

15. Determines a “Best Age” for each analysis, which is generally the 206/238 age for <900 Ma ages and the 206/207 age for >900 Ma ages

16. Provides preliminary filters that highlight analyses with >20% discordance, >5% reverse discordance, or >10% internal (measurement) uncertainty.

17. Creates a publication-ready datatable with concentrations, isotope ratios, and ages for unknowns.

References

Gehrels, G.E., Valencia, V., Ruiz, J., 2008, Enhanced precision, accuracy, efficiency, and spatial resolution of U-Pb ages by laser ablation–multicollector–inductively coupled plasma–mass spectrometry: Geochemistry, Geophysics, Geosystems, v. 9, Q03017, doi:10.1029/2007GC001805.

Gehrels, G.E., Valencia, V., Pullen, A., 2006, Detrital zircon geochronology by Laser-Ablation Multicollector ICPMS at the Arizona LaserChron Center, in Loszewski, T., and Huff, W., eds., Geochronology: Emerging Opportunities, Paleontology Society Short Course: Paleontology Society Papers, v. 11, 10 p.

Gehrels, G. and Pecha, M., 2014, Detrital zircon U-Pb geochronology and Hf isotope geochemistry of Paleozoic and Triassic passive margin strata of western North America: Geosphere, v. 10 (1), p. 49-65.

Harrison, T.M., G. M,M.K. D, Coath, C.D., Lovera, O.M., and Le Fort, P., 1999, Origin and episodic emplacement of the Manaslu intrusive complex, central Himalaya: J. Petrol. v. 40, p. 3-19.

Ludwig, K.R., 2012, Isoplot 3.75. Berkeley Geochronology Center, Special Publication No. 5, 75 p.

Peterman, E.M., Mattinson, J.M., and Hacker, B.R., 2012, Multi-step TIMS and CA-TIMS tomonazite U–Pb geochronology: Chem. Geol. v. 312–313, p. 58–73.

Stacey, J.S., and Kramers, J.D., 1975, Approximation of terrestrial lead isotope evolution by a two-stage model: Earth and Planetary Science Letters, v. 26, p. 207-221.